

Functionalized porous (organo)silicas for applications in enamine catalysis and photocatalysis

Judith Ouwehand

Promotors: Prof. Dr. Pascal Van Der Voort

Prof. Dr. Ir. Joris W. Thybaut

Dissertation submitted to the Faculty of Sciences of Ghent University in fulfillment of the requirements for the degree of Doctor in Science: Chemistry

Department of Chemistry

Faculty of Sciences

Ghent University

2018



Members of the examination committee

Chair

Prof. Dr. Klaartje De Buysser (Ghent University)

Examination Committee

Prof. Dr. Dirk Poelman (Ghent University)

Dr. Ir. Jeroen Lauwaert (Ghent University)

Dr. Anna Kaczmarek (Ghent University)

Prof. Dr. Pegie Cool (University of Antwerp)

Prof. Dr. Sammy Verbruggen (University of Antwerp)

Dr. Els De Canck (Recticel Insulation)

Be like the squirrel, girl. Be like the squirrel.

-The White Stripes

Table Of Contents

Table of contents	I
Acknowledgements	V
List of publications	VII
Summary	IX
Samenvatting	XIII
List of abbreviations	XVII
Outline	XXI
PART I. Functionalized periodic mesoporous organosilicas for enamine catalysis	
Chapter 1. An introduction to functional periodic mesoporous organosilicas	1.1
1.1 A brief history of periodic mesoporous (organo)silicas	1.1
1.1.1 The emergence of ordered mesoporous silicas	1.1
1.1.2 The liquid crystal templated sol-gel synthesis	1.2
1.1.3 The effect of pore structure on diffusion	1.4
1.2 Functionalization of periodic mesoporous silicas	1.5
1.2.1 Grafting	1.6
1.2.2 Co-condensation	1.6
1.2.3 Direct incorporation of bissilanes: the emergence of PMOs.....	1.7
1.3 The three COMOC PMOs and the thiol-ene click reaction	1.8
1.3.1 The 100% trans ethene PMO (or ePMO)	1.9
1.3.2 The monoallyl ring PMO (or mAR-PMO).....	1.11
1.3.3 The thiol PMO	1.12

Chapter 4. Proline-functionalized PMOs for asymmetric enamine catalysis	4.1
4.1 Introduction to immobilized proline	4.1
4.2 Set-up and aim of the research	4.2
4.3 Results and discussion	4.2
4.3.1 Synthesis and characterization of the 25% thiol PMO	4.2
4.3.2 Proline-functionalization of the PMO	4.6
4.3.2.1 Allylation of hydroxyproline	4.6
4.3.2.2 The thermal anchoring method	4.7
4.3.2.3. The UV anchoring method	4.9
4.3.2.4 Revisiting the thermal anchoring method	4.12
4.4 Conclusions	4.17
4.5 Experimental Details	4.18
4.6 References	4.21

PART II. Titania-functionalized frustules as photocatalysts

Chapter 5. An introduction to titania and titania/silica composites in photocatalysis ..	5.1
5.1 Titania as a photocatalyst	5.1
5.1.1 The different forms of titania	5.1
5.1.2 The mechanism of photocatalysis	5.2
5.1.3 Anatase versus rutile as photocatalyst	5.3
5.2 Titania/silica composites as photocatalysts	5.5
5.2.1 The role of silica in composite materials	5.5
5.2.2 Synthesis methods of titania/silica composites	5.7
5.2.2.1 The sol-gel synthesis method	5.7
5.2.2.2 Post-functionalization of pre-formed porous silicas	5.8
5.3 Diatom frustules as silica source	5.9
5.3.1 An introduction to diatom frustules	5.9
5.3.2 Technological applications of diatom frustules	5.11
5.3.3 Diatom frustules in titania/silica composites	5.12
5.4 References	5.13

Chapter 6 Titania-functionalized diatom frustules as photocatalyst for indoor air purification	6.1
6.1 Set-up and aim of the research	6.1
6.2 Results and discussion	6.2
6.2.1 Extraction and characterization of frustules	6.2
6.2.2 Optimization of calcination temperature and duration	6.4
6.2.3 Optimization of titania loading	6.7

6.2.4 Further characterization of the optimized photocatalyst	6.9
6.2.5 Influence of humidity on the photocatalytic activity	6.11
6.2.6 Extended activity study	6.12
6.3 Conclusions	6.13
6.4 Experimental details	6.13
6.5 References	6.17
Outlook and Perspectives.....	7.1

Acknowledgements

I want to start by thanking my main promotor, Pascal Van Der Voort, for giving me the opportunity to pursue my PhD in the COMOC group and for always having blind faith in me as a researcher. As for my second promotor, Joris Thybaut, I always appreciated the time you took to give your perspective on my work and your insights from an engineering point of view were always very helpful. In this line I also want to thank An Verberckmoes, even though you were not technically my promotor, I highly appreciated your involvement in the Biocapps project. Your close follow-up of the research and your support were of tremendous help.

Secondly I want to thank all members of COMOC, past and present, for your everyday presence. For the past four years I worked not only surrounded by colleagues but surrounded by friends every day. You guys, make sure to keep that lab clean, it should be a little bit easier now that my mess is gone! Of course I also thank the other members of S3 for the general good vibes we shared on a daily basis.

A special shout-out goes to the PMO team: Els, Sander and Dolores. It was great to be surrounded by passionate researchers in the same field and you guys were a great support system. Sander, my last year in the lab just wasn't the same without mocking you and your tiny filters. And of course Pegie Cool and Ward Huybrechts, even though we met less often it was always appreciated to get feedback from fellow PMO researchers.

I was lucky to work with researchers from different departments as well. I particularly appreciated the collaboration with Jeroen Lauwaert and Anton De Vylder. It was always interesting to get an engineer's perspective and to share the same line of research. Especially Jeroen, you were of great help getting me started on my research project and were always there for advice. And of course I appreciate the countless HPLC analyses you both did for me.

I also felt very lucky to be part of the Biocapps project. It was a complete U-turn from my PMO research but I highly appreciated broadening my knowledge and discovering the field of photocatalysis. Of course I am grateful to Erik Van Eynde for setting up the project and for the great collaboration we had.

I also want to especially thank Els De Canck, for your support throughout your time in COMOC but also beyond. You are a truly generous person and I highly appreciated all the time you devoted to me in the past year.

Next I want to thank the two people who support me the most, my parents. Thank you for believing in me, supporting me, missing me, encouraging me and always being there for me.

And finally Fady, you were there for me during the good times and made them so much better. You were there for me during the bad times and made them go away. Thanks for calming me, comforting me, distracting me and annoying me every day.

List of Publications

A1 Publications

J. Ouwehand, J. Lauwaert, D. Esquivel, K. Hendrickx, V. Van Speybroeck, J.W. Thybaut, P. Van Der Voort, Facile Synthesis of Cooperative Acid-Base Catalysts by Clicking Cysteine and Cysteamine on an Ethylene-Bridged Periodic Mesoporous Organosilica, *European Journal of Inorganic Chemistry*, (2016) 2144-2151.

J. Lauwaert, J. Ouwehand, J. De Clercq, P. Cool, P. Van Der Voort, J.W. Thybaut, Tuning component enrichment in amino acid functionalized (organo)silicas, *Catalysis Communications*, 88 (2017) 85-89.

A.M. Kaczmarek, D. Esquivel, J. Ouwehand, P. Van der Voort, F.J. Romero-Salguero, R. Van Deun, Temperature dependent NIR emitting lanthanide-PMO/silica hybrid materials, *Dalton Transactions*, 46 (2017) 7878-7887.

D. Esquivel, J. Ouwehand, M. Meledina, S. Turner, G. Van Tendeloo, F.J. Romero-Salguero, J. De Clercq, P. Van Der Voort, Thiol-ethylene bridged PMO: A high capacity regenerable mercury adsorbent via intrapore mercury thiolate crystal formation, *Journal of Hazardous Materials*, 339 (2017) 368-377.

E. De Canck, F. Nahra, K. Bevernaege, S. Vanden Broeck, J. Ouwehand, D. Maes, S.P. Nolan, P. Van der Voort, PMO-Immobilized Au-I-NHC Complexes: Heterogeneous Catalysts for Sustainable Processes, *Chemphyschem*, 19 (2018) 430-436.

A. Ryzhikov, T.J. Daou, H. Noualia, J. Patarin, J. Ouwehand, S. Clerick, E. De Canck, P. Van Der Voort, J.A. Martens, Periodic mesoporous organosilicas as porous matrix for heterogeneous lyophobic systems, *Microporous and Mesoporous Materials*, 260 (2018) 166-171.

J. Ouwehand, E. Van Eynde, E. De Canck, S. Lenaerts, A. Verberckmoes, P. Van der Voort, Titania-functionalized diatom frustules as photocatalyst for indoor air purification, *Applied Catalysis B-Environmental*, 226 (2018) 303-310.

X. Feng, H. S. Jena, K. Leus, G. Wang, J. Ouwehand, P. Van Der Voort, L-proline modulated zirconium metal organic frameworks: Simple chiral catalysts for the aldol addition reaction, *Journal Of Catalysis*, 365 (2018) 36-42.

Conference proceedings

J. Ouwehand, D. Esquivel, J. Lauwaert, J. W. Thybaut and P. Van Der Voort, Amino acid functionalized periodic mesoporous organosilicas as bifunctional catalysts, NCCC 2015, Noordwijkerhout, Netherlands, Poster presentation.

J. Ouwehand, E. Van Eynde, E. De Canck, S. Lenaerts, A. Verberckmoes and P. Van Der Voort, Titania-functionalized diatom frustules as photocatalysts for indoor air purification, ChemCys 2018, Blankenberge, Belgium, Oral presentation.

Summary

In part one of this dissertation, functionalized periodic mesoporous organosilicas (PMOs) are investigated as heterogeneous enamine catalysts. PMO materials emerged in 1999 and have since been studied for applications in catalysis, adsorption, low-*k* materials, controlled drug release and chromatographic stationary phases. PMOs emerged from a need for mesoporous materials which contain a functional organic group and which are hydrolytically stable. These requirements were achieved by using bridged bis-silanes in a sol-gel synthesis, yielding materials with organic functional groups incorporated directly into the structure. This in contrast with the traditional functionalization methods used on mesoporous silicas, namely grafting and co-condensation, which make use of organosilanes. The PMO structure gives us the opportunity to add a useful functionality onto the PMO by directly modifying the PMO backbone and therefore the desired functionality can be attached via stable covalent bonds to the PMO structure, which avoids leaching. The three PMOs which were developed in our research group are the ethene PMO (or ePMO), the monoallyl ring PMO (or mAR-PMO) and the thiol PMO. All three of these PMOs are synthesized from a functional precursor, which allows further modification of the PMO materials. In particular, all three of these PMOs can be modified using the thiol-ene click reaction. This reaction links a thiol and a C=C functionality in a radical reaction mechanism to yield a thioether bond.

In this work, the ePMO and mAR-PMO materials were functionalized with cysteine and cysteamine. The thiol PMO was modified with proline, all making use of the thiol-ene click reaction. The purpose of these materials was to be used as heterogeneous enamine catalysts. This type of catalyst can be applied to the aldol reaction, to selectively yield the aldol addition product and limit the formation of the condensation product. To this end, aminated mesoporous silicas have previously been used as cooperative catalysts. In that case, the amine acts as a nucleophile which activates the nucleophilic reagent and the silanol groups on the silica surface activate the electrophilic reagent. This enhances the

reaction rate while keeping a high selectivity towards the aldol addition product. When using a chiral catalyst such as L-proline, the aldol product can be formed enantioselectively. Several efforts have also been made to heterogenize proline on solid supports to this end.

We functionalized the ePMO with cysteine and cysteamine, and did the same for the ePMO with end-capped silanol groups in order to investigate the influence of the different acid promoting sites (silanol groups and carboxylic acid). The loading of the functional groups on the materials were also varied to study their effect on the reactivity of the materials. The test reaction used for these materials was the aldol reaction of acetone and 4-nitrobenzaldehyde. We found that the thiol-ene click reaction in water, using Irgacure 2959 as radical initiator was successful in grafting the functionalities to the PMO structure. When comparing materials with similar loadings of functional groups, we found that the silanol groups had a stronger promoting effect than the carboxylic acid groups. This could be due to the difference in pKa of the two acid sites, but also to the positioning of the acid sites relative to the amine. When comparing materials bearing the same functional groups, but in different loadings, we found that the catalytic activity decreased with increasing loading. To explain this, a computational model was used to investigate hydrogen bond formation between functional groups on the material. It was found that two cysteine moieties grafted onto neighbouring ePMO precursors were prone to hydrogen bonding together, thus deactivating the functionalities for catalysis. A single cysteine grafted onto the material showed no hydrogen bonding with the silanol groups on the PMO surface. This could account for the decrease in activity at higher loadings, where neighbouring cysteine moieties would be more likely to occur. We further attempted a similar modification on the mAR-PMO. However, the catalytic activity of this PMO was much lower than that of the functionalized ePMO. The different factors that could influence the activities between these materials were investigated. They were the mesopore structure, the silanol group density and the linker length. It was concluded that the chain length of the functional groups was probably one of the determining factors in the difference in catalytic activity.

In an effort to create an enantioselective enamine catalyst for the aldol reaction, proline was grafted onto a 25% thiol PMO. A commercially available Boc-hydroxyproline was modified with an allyl functionality. This allylated product was then linked to the thiol functionalities on the PMO via a thiol-ene click reaction in toluene, using AIBN as radical initiator. After the click reaction, the Boc-group was removed by a TFA treatment. This method was based on literature reports, but the resulting PMO material was not active in the aldol reaction. A different functionalization method, based on the UV-initiated click reaction in water was attempted but while the resulting materials showed more conversion, they were not enantioselective catalysts either. The thermal functionalization method was then tested on a thiol PMO with capped silanol groups, as well as a thiolated ethane PMO and a thiolated SBA-15 material. The capped thiol PMO and ethane PMO

X

materials did show significant enantioselectivity in the aldol reaction after modification with proline. The catalytic conditions of these two materials should be further optimized in order to achieve the same degree of conversion and enantioselectivity as similar materials reported in the literature.

In the second part of the dissertation, a titania-functionalized diatom frustule material is investigated for photocatalytic applications in indoor air pollution. Diatom frustules are a biogenic porous silica, produced by diatoms (single-celled algae) as a protective shell. Diatom frustules present a wide variety of hierarchically organized porous silica materials and might become a widely available side-product of diatom-based biofuel production. Porous silicas are useful for the immobilization of titania particles in photocatalytic applications. Synthesizing the titania particles onto the silica material can limit the size of the titania nanoparticles. Additionally, adsorption of the reagents on the silica surface and subsequent diffusion to the active titania site can also increase the photocatalytic activity.

We chose the diatom species *Thalassiosira Pseudonana* for its availability, its fast growth and the high surface area of its frustules. The frustules were extracted by using an acid digestion of the organic material, followed by calcination at 550°C, resulting in a pure silica material with a specific surface area of 115 m²/g and pores of 20 nm diameter. We used the water-soluble titania source titanyl sulfate (TiOSO₄) to functionalize the frustules. After calcination, a material containing titania nanoparticles in the anatase phase was obtained. The synthesis conditions were optimized by varying the calcination duration and temperatures, as well as the ratio of titania to silica. The optimization was based on the photocatalytic activity of each material in the used test reaction, namely the decomposition of gaseous acetaldehyde. This reaction was chosen as a test reaction representing the decomposition of VOCs in polluted indoor air. The optimized material was visualized using TEM imaging, as well as STEM-EDX mapping. We can see titania nanoparticles with an average particle size of 8 nm. Some of the nanoparticles are lodged inside the silica pores, while others are attached to the silica surface. The activity of the optimized photocatalyst was compared to that of P25, the most common benchmark for titania-based photocatalysts. The activity of the titania nanoparticles in the material was about 2.5 times higher than that of P25. The material was also tested in conditions of increasing relative humidity (RH). We found an optimum at 12.5% RH, but at the typical RH value of 50% for indoor air, only a slight decrease in activity of the photocatalyst occurred, when compared to P25. Finally, the material was subjected to a longer measurement of 48 consecutive hours, to test its deactivation over time. We saw that although the activity fluctuated somewhat over time, the average activity was only slightly lower than in the initial, short measurement. We therefore concluded that the titania-functionalized frustules were an interesting photocatalyst for indoor air applications, as they showed good results at 50% RH and over prolonged periods of time.

Samenvatting

In het eerste deel van deze uiteenzetting worden periodische mesoporeuze organosilicas (PMO's) onderzocht als heterogene enamine katalysatoren. PMO materialen zijn in 1999 opgekomen en zijn onderzocht voor toepassingen in katalyse, adsorptie, low-*k* materialen, gecontroleerde afgifte van medicijnen en chromatografische stationaire fasen. PMO's zijn ontstaan uit een behoefte aan hydrolytisch stabiele materialen die een functionele organische groep bevatten. Aan deze voorwaarden werd voldaan door het gebruik van gebrugde bissilanen in een sol-gel synthese, waaruit materialen ontstaan met een functionele organische groep die direct in het materiaal verwoven is. Dit in tegenstelling tot de traditionele functionalisatiemethodes van mesoporeuze silica materialen, namelijk grafting en co-condensatie met behulp van organosilanen. De PMO structuur biedt de mogelijkheid om een nuttige functionele groep aan het materiaal te verankeren, via directe modificatie van de PMO structuur. Daardoor kan de functionele groep via stabiele covalente bindingen verankerd worden, wat problemen met uitloging vermijdt. De drie PMO's die in onze onderzoeksgroep werden ontwikkeld zijn de ethaan PMO (ePMO), de monoallyl ring PMO (mAR-PMO) en de thiol PMO. Elk van deze drie PMOs wordt gesynthetiseerd vanuit een functionele precursor, wat verdere modificatie van de PMO materialen mogelijk maakt. In het bijzonder zijn deze drie PMOs geschikt voor modificatie via de thiol-een click reactie. Deze reactie verbindt een thiol groep en een C=C dubbele binding via een radicalair mechanisme, met vorming van een thioether.

In dit werk werden de ePMO en mAR-PMO materialen gefunctionaliseerd met cysteïne en cysteamine. De thiol PMO werd gemodificeerd met proline. Al deze procedures maakten gebruik van de thiol-een click reactie. Het doel van deze materialen was het gebruik als heterogene enamine katalysatoren. Dit is een type katalysator die op aldol reacties kan worden toegepast, om selectief het aldol additieproduct te vormen en de vorming van het condensatieproduct te voorkomen. Hiervoor zijn tot nu toe geamioneerde mesoporeuze silica's als cooperatieve katalysatoren gebruikt. In dat geval treedt het amine als nucleofiel

op dat het nucleofiele reagens activeert en de silanol groep op het silica oppervlak activeert het elektrofile reagens. Dit versnelt de reactie met behoud van de selectiviteit van het additieproduct. Wanneer een chirale katalysator zoals L-proline wordt gebruikt, kan het aldol product ook enantioselectief gevormd worden. Meerdere pogingen zijn dan ook ondernomen om proline te heterogeniseren op een vaste drager.

We hebben de ePMO gefunctionaliseerd met cysteïne en cysteamine, en hebben hetzelfde gedaan voor de PMO met afgeschermd silanol groepen. Zo konden we de invloed van de verschillende zuurgroepen (silanolen of carbonzuur) onderzoeken. De belading van de functionele groepen op deze materialen werd gevarieerd om het effect op de activiteit van de materialen te onderzoeken. De testreactie die voor deze materialen werd gebruikt was de aldol reactie van aceton en 4-nitrobenzaldehyde. De thiol-*een* click reactie in water, met Irgacure 2959 als radicalaire initiator bleek succesvol te zijn voor het verankeren van de functionele groepen op het PMO oppervlak. Wanneer we de materialen met gelijkaardige beladingen vergelijken, blijkt dat de silanol groepen een groter activerend effect hebben dan het carbonzuur. Dit kan komen door het verschil in pKa tussen de twee zuren, of door de relatieve posities van de zuren ten opzichte van het amine. Wanneer we de materialen met dezelfde functionele groepen, maar met verschillende beladingen vergelijken, zien we dat de katalytische activiteit daalt met toenemende belading. Om dit te verklaren werd een computationeel model gebruikt om de waterstofbrugvorming tussen de functionele groepen op het materiaal te bestuderen. Er bleek dat twee cysteïne eenheden die op naburige ePMO eenheden werden verankerd samen waterstofbruggen konden vormen, waardoor de functionaliteit gedesactiveerd werd voor katalyse. Een enkele cysteïne groep vertoonde geen waterstofbrugvorming met de silanolgroepen aan het oppervlak. Dit zou kunnen verklaren waarom de activiteit daalt bij hogere beladingen, aangezien in dat geval naburige cysteïne groepen meer kans hebben om voor te komen. We hebben een gelijkaardige functionalisatie ook op de mAR-PMO geprobeerd, maar de katalytische activiteit was veel lager dan die van de gefunctionaliseerde ePMO. De verschillende factoren die dit verschil in activiteit zouden kunnen verklaren werden onderzocht, namelijk de mesoporiestructuur, de dichtheid van de silanolgroepen en de ketenlengte van de functionele groepen. Er werd besloten dat de ketenlengte waarschijnlijk een van de bepalende factoren was in het verschil in activiteit tussen de twee materialen.

Om ook een enantioselectieve enamine katalysator voor de aldol reactie te verkrijgen, werd proline verankerd op een 25% thiol PMO. Een commercieel beschikbaar Boc-hydroxyproline werd gemodificeerd met een allyl groep. Dit geallyleerd product werd toen verankerd op de thiol groepen via de thiol-*een* click reactie in toluen, met AIBN als radicalaire initiator. Na de click reactie werd de Boc-groep verwijderd via een zuurbehandeling met TFA. Deze methode werd gebaseerd op de literatuur, maar het bekomen PMO materiaal was niet actief in de aldol reactie. Een andere functionalisatiemethode, gebaseerd op de UV-

geactiveerde click reactie in water werd toegepast op dezelfde PMO, maar ondanks een hogere conversie, gaf het resulterende materiaal ook geen enantioselectief aldol product. De thermale click reactie werd ook toegepast op een thiol PMO met afgescherme silanolgroepen, alsook op een ethaan PMO met gegrafte thiol groepen en een SBA-15 met gegrafte thiol groepen. De ethaan PMO en de thiol PMO met afgeschermd silanolen vertoonden wel enantioselectiviteit in de aldol reactie na modificatie met proline. De reactiviteit van deze materialen zou nog verder geoptimaliseerd moeten worden om de gerapporteerde resultaten van gelijkaardige materialen te evenaren.

In het tweede deel van deze verhandeling werden titania-gefunctionaliseerde diatomee frustules onderzocht voor fotokatalytische toepassingen in de zuivering van lucht in gebouwen. Diatomee frustules bestaan uit een biogeen, poreus silica materiaal dat geproduceerd wordt door diatomeeën (eencellige algen) als een beschermend schild. Diatomee frustules voorzien een grote verscheidenheid van hiërarchisch geordende poreuze silica materialen. Ze zouden een belangrijk bijproduct kunnen worden van grootschalige diatomee productie in verband met de opkomst van biobrandstof. Poreuze silica's zijn nuttig als dragermateriaal voor titania partikels in fotokatalytische toepassingen. De synthese van titania deeltjes op een silica materiaal kan hun groei beperken, waardoor ze hogere activiteit kunnen vertonen. Ook kunnen reagentia op het silica oppervlak adsorberen en vervolgens naar de actieve titania site diffunderen, waardoor de fotokatalytische activiteit stijgt.

We verkozen de diatomee soort *Thalassiosira Pseudonana* om haar beschikbaarheid, snelle groei en hoge oppervlak van de frustules. De frustules werden geïsoleerd met behulp van een vertering van het organische materiaal in zuur, gevolgd door calcinatie op 550°C. Dit resulteerde in een puur silica materiaal met een specifiek oppervlak van 115 m²/g en poriën van 20 nm. De wateroplosbare titania bron tytanylsulfaat (TiOSO₄) werd gebruikt om de frustules te functionaliseren. De synthesecondities werden geoptimaliseerd door de duur en de temperatuur aan te passen, alsook de verhouding tussen titania en silica. Deze optimalisatie werd gebaseerd op de fotokatalytische activiteit van elk materiaal in de testreactie, namelijk de afbraak van gasvormig acetaldehyde. Deze reactie werd gekozen als testreactie om de afbraak van vluchtige organische pollutanten in de lucht te vertegenwoordigen. Het geoptimaliseerde materiaal werd gevisualiseerd via TEM en STEM-EDX. We kunnen de titania deeltjes, van gemiddeld 8 nm groot, op het materiaal zien zitten. Sommige van de titania deeltjes zijn verankerd in de poriën van de frustules, andere zitten verankerd op het silica oppervlak. De activiteit van het geoptimaliseerde materiaal werd vergeleken met dat van P25, de meest gebruikte standaard in fotokatalyse. De activiteit van de titania deeltjes op de frustules was rond de 2.5 maal hoger dan dat van P25. Het materiaal werd ook getest in condities van oplopende luchtvochtigheid. We zagen een optimum bij 12.5% luchtvochtigheid, maar bij de realistische waarde van 50%

luchtvochtigheid in lucht binnenshuis, zagen we slechts een kleine daling in activiteit, in vergelijking met P25. Uiteindelijk werd het materiaal blootgesteld aan een lange meting van 48 opeenvolgende uren, om de deactivatie van het materiaal in functie van de tijd te bestuderen. We zagen dat, ondanks een fluctuatie van de activiteit, de gemiddelde activiteit slechts een fractie daalde ten opzichte van de kortere metingen. We besloten dus dat de titania-gefunctionaliseerde frustules een interessante fotokatalysator vormen voor toepassingen in luchtzuivering, aangezien ze actief zijn bij 50% luchtvochtigheid en over langere periodes.

List of abbreviations

AIBN	Azobisisobutyronitrile
ALD	Atomic Layer Deposition
a.u.	arbitrary units
BET	Brunauer-Emmett-Teller
BINAP	2,2'-Bis((diphenylphosphino)-1,1'-binaphtyl)
Boc	tert-Butyl Oxycarbonyl
BTEE	1,2-Bis(triethoxysilyl)ethane
BTETE	1,2-bis(triethoxysilyl)thio-ethane
BTME	1,2-Bis(trimethoxysilyl) Ethane
CB	Conduction Band
COMOC	Center for Ordered Materials, Organometallics and Catalysis
CPB	Cetylpyridinium Bromide
CPC	Cetylpyridinium Chloride
CTAB	Cetyltrimethylammonium Bromide
CTAC	Cetyltrimethylammonium Chloride
CVD	Chemical Vapor Deposition
DCM	Dichloromethane
DFT	Density Functional Theory
DMPA	2,2-Dimethoxy-2-Phenylacetophenone
DMSO	Dimethyl Sulfoxide
DRIFTS	Diffuse Reflectance Infra Red Fourier Transform Spectroscopy
DTAB	Dodecyltrimethylammonium Bromide
DTAC	Dodecyltrimethylammonium Chloride
EDX	Energy-dispersive X-Ray Spectroscopy
ee	enantiomeric excess

ePMO	ethene PMO
FT	Fourier Transform
HAADF	High-Angle Annular Dark-Field
HMDS	Hexamethyl Disilazane
HPLC	High Performance Liquid Chromatography
mAR	Monoallyl Ring
MCM	Mobil Composition of Matter
MPTES	Mercaptopropyl Triethoxysilane
MPTMS	Mercaptopropyl trimethoxysilane
NMR	Nuclear Magnetic Resonance
PMO	Periodic Mesoporous Organosilica
PMS	Periodic Mesoporous Silica
ppm	parts per million
PVD	Physical Vapor Deposition
RH	Relative Humidity
RI	Radical Initiator
SBA	Santa Barbara Amorphous
SDA	Structure Directing Agent
SEM	Scanning Electron Microscopy
STEM	Scanning Transmission Electron Microscopy
TBHP	Tert-Butyl Hydroperoxide
TBOT	Tetrabutyl Orthotitanate
t-BuLi	Tert-Butyl Lithium
TDI	Terrylene Diimide
TEA	Triethyl Amine
TEM	Transmission Electron Microscopy
TEOS	Tetraethyl Orthosilicate
TFA	Trifluoro Acetic Acid
THF	Tetrahydrofuran
TiBALDH	Titanium (IV) bis (ammonium lactato) dihydroxide
TMOS	Tetramethyl Orthosilicate
TMS	Trimethyl Silane
TOF	Turnover Frequency
TTIP	Titanium Tetraisopropoxide
UV	Ultra Violet
VB	Valence Band

VOC	Volatile Organic Compound
XRD	X-Ray Diffraction
XRF	X-Ray Fluorescence

Outline

What Follows is a PhD dissertation in two parts. The first part focuses on the synthesis of functionalized organosilicas for heterogeneous catalysis. The second part discusses a project on photocatalysis. A detailed outline of the manuscript follows hereafter.

Part I: Functionalized periodic mesoporous organosilicas for enamine catalysis.

Chapters 1 and 2 are introductory chapters which give the reader an overview of the literature required to understand the experimental parts.

Chapter 1 focuses on PMO materials and describes their development and the important parameters of their synthesis. There is also a literature review focused on the state of the art in functionalizing PMO bridges, either before or after the PMO synthesis.

Chapter 2 gives an introduction on the aldol reaction and the different ways this reaction can be catalyzed. It then focuses on the enamine catalysis pathway and gives the state of the art in cooperative heterogeneous catalysts reported to perform this type of catalysis.

Chapters 3 and 4 are experimental chapters.

Chapter 3 discusses the functionalization of an ethene PMO with cysteine and cysteamine, using a thiol-ene click reaction. This material is then used as a cooperative catalyst in an aldol reaction. The synthesis of the material is described and the catalytic results are analyzed in detail.

In **Chapter 4**, proline is anchored on a 25% thiol PMO via two different methods based on the thiol-ene click reaction. The aim is to obtain an enantioselective catalyst for the aldol reaction. The functionalization is also performed on several other (organo)silicas in order to better interpret the obtained results.

Part II: Titania-functionalized frustules as photocatalysts

Chapter 5 is the introductory chapter for part II of the dissertation. It describes the physical and photocatalytic properties of titania. Then, the concept of titania/silica composite materials is introduced with an overview of different synthesis methods. Diatom frustules are introduced and the state of the art is given on their use in titania/silica materials.

Chapter 6 describes research done on the synthesis of titania-functionalized diatom frustules and their application in the degradation of acetaldehyde. The optimization of the synthesis condition is discussed and the resulting material is tested in different conditions which are relevant to photocatalytic applications in indoor air pollution.

Part I.

Functionalized periodic mesoporous organosilicas for enamine catalysis

Chapter 1.

An introduction to functional periodic mesoporous organosilicas

1.1 A brief history of ordered mesoporous silicas

1.1.1 The emergence of ordered mesoporous silicas

The history of periodic mesoporous silica (PMS) materials started in 1992, when the Mobil corporation reported the synthesis of a family of templated silica materials, named M41S.¹ They pioneered the use of the liquid crystal templated synthesis, in which micelles are used as a structure directing agent (SDA). In this type of synthesis, the silica precursor condenses around the SDA, which is removed after the formation of the solid. In this way, a pore structure with the same conformation as the SDA is obtained in the material. This principle is illustrated in Figure 1.1. It shows a schematic representation of the SDAs used for the synthesis of MCM-41 with a hexagonal pore structure, MCM-48 with a cubic pore structure and MCM-50 with a lamellar pore structure. This type of synthesis introduced ordered pores with diameters of 3 to 4 nm. This was an advancement compared to zeolites, of which the pore size did not exceed 1 nm.

Later on, in 1998, the SBA-type materials emerged.² They were synthesized with triblock copolymers as SDA, which increased the pore size of the materials. Pore diameters of 4 to 10 nm were obtained for SBA-15, which has a hexagonal pore structure. While this material has large mesopores, it also has a high pore wall thickness, which provides it with good mechanical stability. Another difference as a result of the polymeric template is that micropores are formed, which connect the mesopores of the material. SBA-type materials also have high specific surface areas and pore volumes. Typical values for SBA-15 are BET

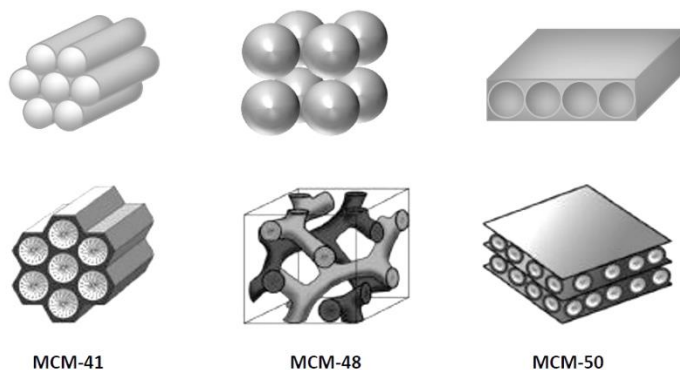


Figure 1.1. A schematic representation of the SDA (top) inducing an ordered pore structure in a mesoporous silica (bottom).

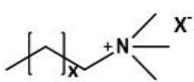
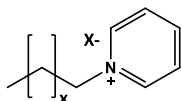
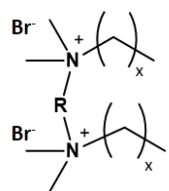
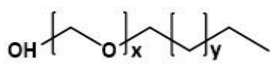
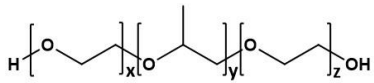
(Brunauer-Emmett-Teller) surface areas between 600 and 900 m²/g and pore volumes of around 1 cm³/g.²

1.1.2 The liquid crystal templated sol-gel synthesis

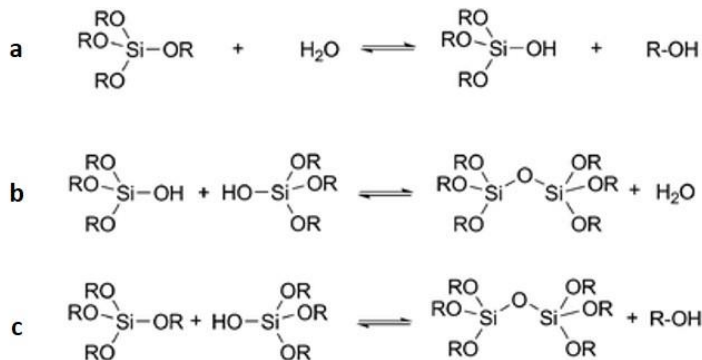
Periodic mesoporous silica materials are formed via a templated synthesis. This template, also called the structure directing agent (SDA) or the liquid crystal template, consists of micelles formed by a variety of molecules. In a typical synthesis, the SDA is dissolved in the reaction mixture at a high concentration. When the critical micelle concentration is reached, the SDA self-assembles into micelles, which can have different configurations such as spherical, cylindrical or lamellar. If the SDA concentration is increased further, the micelles can shift to a different configuration. The type of SDA and its concentration thus dictate the pore structure of the resulting material.

An overview of the most common SDAs is given in Table 1.1. We can distinguish two types of templates. The first type are ionic templates, containing a hydrophilic head and a hydrophobic tail. The most common of these are the cationic surfactants which contain an ammonium or pyridinium group and a hydrophobic tail. Gemini surfactants are cationic surfactants which contain two ammonium groups and two tails, separated by a spacer. The second type of SDA are non-ionic polymers. The Brij-type polymers contain a long hydrophobic alkyl chain, connected to a hydrophilic polyethylene oxide chain. Another type of non-ionic polymer surfactants are the triblock copolymers, also called Pluronics, containing a hydrophobic polypropylene oxide block, flanked by hydrophilic polyethylene oxide blocks on either side. The micelle size of each SDA determines the pore size of the resulting mesoporous material, whereas the micelle concentration determines the ordering configuration of the micelles, and thus of the porous structure of the resulting material.

Table 1.1. An overview of the most common structure directing agents.

Chemical structure	Specifications	Name	Abbreviation
	x = 14, X = Br	Cetyltrimethylammonium Bromide	CTAB
	x = 14, X = Cl	Cetyltrimethylammonium Chloride	CTAC
	x = 10, X = Br	Dodecyltrimethylammonium Bromide	DTAB
	x = 10, X = Cl	Dodecyltrimethylammonium Chloride	DTAC
	x = 14, X = Br	Cetylpyridinium Bromide	CPB
	x = 14, X = Cl	Cetylpyridinium Chloride	CPC
	x = 11 R = (C ₂ H ₄)-O-(C ₂ H ₄)	Diethyl ether -1,4-bis(dimethyl dodecylammonium bromide)	-
	x = 11 R = (C ₄ H ₈)	Butane-1,4-bis(dimethyl dodecylammonium bromide)	-
	x = 10, y = 13	Polyoxyethylene(10) cetyl ether	Brij-56
	x = 10, y = 15	Polyoxyethylene(10) stearyl ether	Brij-76
	x = z = 20, y = 70	Pluronic P123	P123
	x = z = 101, y = 56	Pluronic F127	F127

Once the SDA micelles have been allowed to assemble in an aqueous solution, a silica precursor is added. This is usually a tetra-alkoxysilane, such as tetraethyl orthosilicate (TEOS) or tetramethyl orthosilicate (TMOS). A silica network is formed by the hydrolysis and condensation of the silane, as shown in Scheme 1.1.³ Reaction **a** shows the hydrolysis of TEOS (if R = Et), which is acid or base-catalyzed. Reaction **b** is the condensation of the silanol moieties of two hydrolyzed TEOS species, yielding a water molecule. Alternatively, a mixed condensation between a silanol and an alkoxide can occur, yielding an alcohol molecule (reaction **c**). After completion of this sol-gel synthesis, a rigid three-dimensional silica network is formed. The condensation of the silica occurs amidst the micelles in the solution, thus taking the shape of the SDA. In order to improve the interaction between the silane and the SDA, usually an inorganic salt such as NaCl or KCl or an organic additive such as butanol is added to the reaction mixture.



Scheme 1.1. Reaction scheme of the hydrolysis (a) and condensation (b and c) reactions of a tetraalkyl orthosilicate.³

Different types of interactions can take place between the SDA and the silica. In a basic synthesis medium, the silica species is negatively charged and can directly interact with a cationic surfactant. In acidic conditions (below pH 2), the silica species is positively charged and can interact indirectly with cationic surfactants, via the mediation of anions (Figure 1.2 a and b). In the case of a non-ionic SDA, interactions can be formed with the silica via hydrogen bonding, for example between an uncharged silica (around pH 2) and the

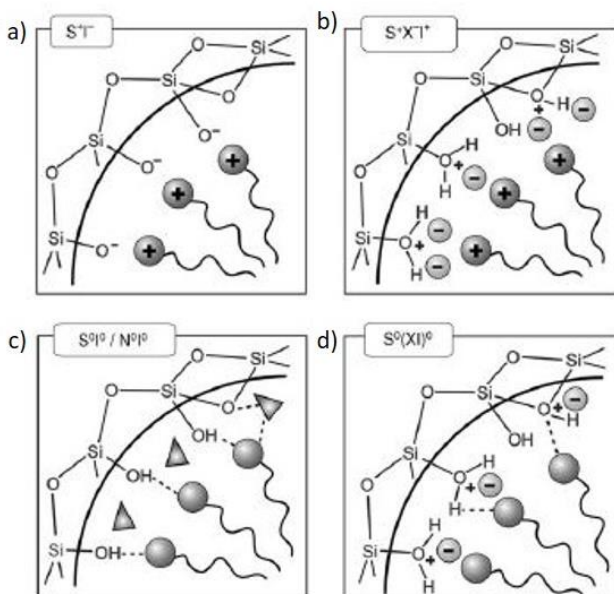


Figure 1.2. A schematic representation of the different possible interactions between surfactants and silica species.⁴ (S=Surfactant, I=Inorganic precursor, N=Non-ionic surfactant, X= mediating anion)

polyethylene oxide chain of a polymeric surfactant. At lower pH, cationic silica with anionic counter-ions can also hydrogen bond with a non-ionic SDA (Figure 1.2 c and d).⁴

In summary, in a typical liquid crystal synthesis, a solution is made of the chosen template and additives, along with an inorganic acid or base, in water. After the template is fully dissolved, the silane is added and gently stirred at a slightly elevated temperature. During the aging step, stirring is stopped and the mixture is heated to enhance the condensation of the silanes. After the silica material is formed, it is filtered and washed. The template can then be removed via calcination or solvent extraction, yielding an ordered mesoporous silica.

1.1.3 The effect of pore structure on diffusion

Is there any concrete benefit to the synthesis of these ordered pore structures? While the increase of diffusion with increasing pore size is very intuitive, the influence of pore ordering on diffusion is perhaps more subtle. This question was investigated experimentally by the group of Bein.⁵ They synthesized an ordered mesoporous silica film by spin-coating a mixture of TEOS, Brij-56, HCl, terylene diimide (TDI) and water onto a flat support. TDI is a highly fluorescent molecule which was used for tracking the diffusion through the pores (Figure 1.3 e). The porous silica film was visualized using transmission electron microscopy (TEM) imaging, while the movements of TDI were tracked via fluorescence microscopy. By combining both measurements, they were able to follow the movements of single TDI molecules through the mesopores. (Figure 1.3 f). The diffusion coefficients of TDI were determined for ordered pores (Figure 1.3 a and b) and blocked pores (Figure 1.3 c and d). The diffusion coefficients are summarized in Table 1.2. These results show that diffusion was significantly faster in the parts of the film which contained ordered cylindrical pores, be they straight or curved. This study proves the benefit of the ordered pore structures in

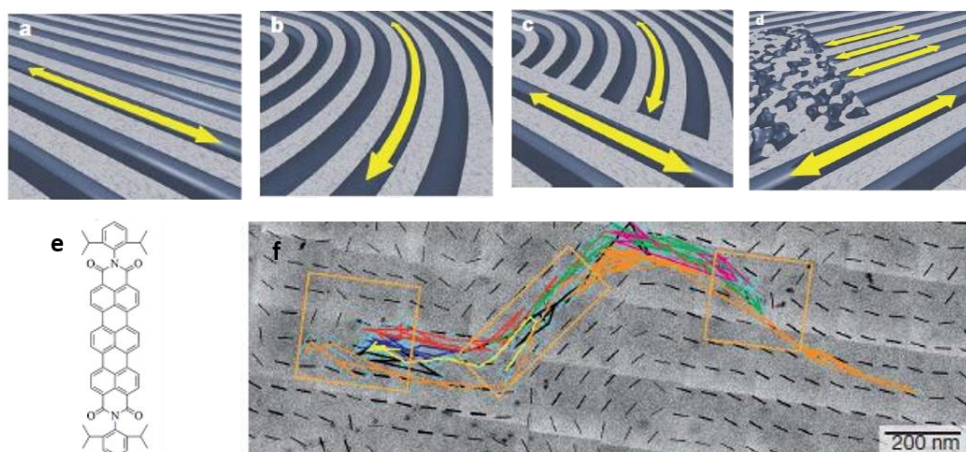


Figure 1.3. A schematic representation of four different pore domains (a-d), the chemical structure of TDI (e) and the diffusion path of TDI through a porous silica film (f).⁵

Table 1.2. The diffusion coefficients of TDI in the porous film, travelling through ordered and blocked pore channels.

Reference in Figure 4	Type of pore structure	Diffusion coefficient ($10^{-2} \mu\text{m}^2/\text{s}$)
a and b	Straight or curved parallel, ordered pore channels	5,5
c	Pore channels blocked by pores with a different orientation	1,1
d	Pore channels blocked by a disordered region	1,0

MCM-41 and SBA-15. Obviously, this can have a substantial influence on the performance of porous materials in applications such as catalysis or adsorption. Unfortunately, no comparative studies for other pore configurations (e.g. 3D ordering) are available at this time.

1.2 Functionalization of periodic mesoporous silicas

High specific surface areas, large pore sizes and tailored pore structures make periodic mesoporous silicas interesting for applications in adsorption, catalysis and others. However, without any organic functional groups, the possible applications are very limited. Two general strategies are known to functionalize PMS materials, namely grafting and co-condensation.⁴ Both of these methods make use of functional silanes of the form $(R'O)_3\text{Si}-R$. Many of these silanes are commercially available, containing functionalities such as amines, thiols, halides or allyls to name a few (Scheme 1.2).



Scheme 1.2. A selection of commercially available functional silanes.

1.2.1 Grafting

Grafting is a post-modification method whereby a pre-formed PMS is reacted with a functional silane (Figure 1.4). This is a very straightforward procedure which leaves the ordered pore structure of the material unaltered. However, the grafting of silanes can cause clustering and even pore blocking, especially at high loadings. With this method, leaching of the functional groups can be a problem when the material is brought into suspension in

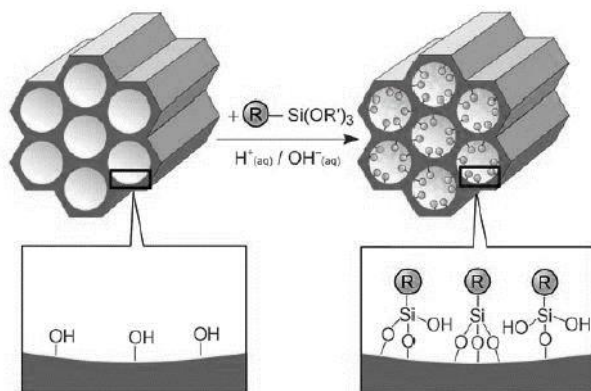


Figure 1.4. Functionalization of a PMS via grafting.⁴

a solvent. Especially in aqueous solutions, the Si-O-Si bond can hydrolyze, releasing the functional silane from the material.

1.2.2 Co-condensation

Co-condensation is a one-pot synthesis method, where the functional silane is directly incorporated during the sol-gel synthesis (Figure 1.5). This method usually ensures a homogeneous distribution of the functional groups and avoids pore blocking. However, if the condensation rate of the inorganic silane and the functional silane differ too much, preferential condensation of one type of silane can occur, resulting in clustering of the

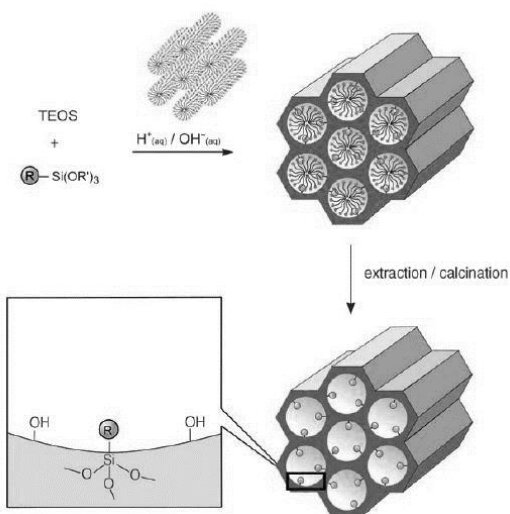


Figure 1.5. Functionalization of a PMS via co-condensation.⁴

functional group or in failure to incorporate the functionality. The mesostructure of the resulting material is usually less well-defined than the pure PMS, because the synthesis of ordered pores gets more difficult to control with increasing organosilane content. Therefore, the loading of functional groups is usually limited to around 20 mol% with this method.

1.2.3 Direct incorporation of bissilanes: the emergence of PMOs

Considering the drawbacks of both grafting and co-condensation of PMS materials, it is especially challenging to obtain a high loading of organic functionalities by either of these methods. This drawback is overcome by the synthesis of periodic mesoporous organosilicas, or briefly PMOs. These materials were pioneered in 1999 by the groups of Inagaki⁶, Stein⁷ and Ozin⁸. They combined the templated sol-gel synthesis with bridged organobissilanes of the form $(R'O)_3Si-R-Si(OR')_3$. The organic functionality R is lodged in between two silane moieties and is thus directly incorporated into the silica framework (Figure 1.6). In this way, a high loading of the functionality is incorporated with a homogeneous distribution. Also, leaching of the organosilane is avoided due to its direct incorporation into the framework. Aside from the fact that small organic functionalities can be incorporated at high loadings in PMO materials, another advantage of PMOs is their increased mechanical and hydrothermal stability, compared to pure silica materials.^{9, 10}

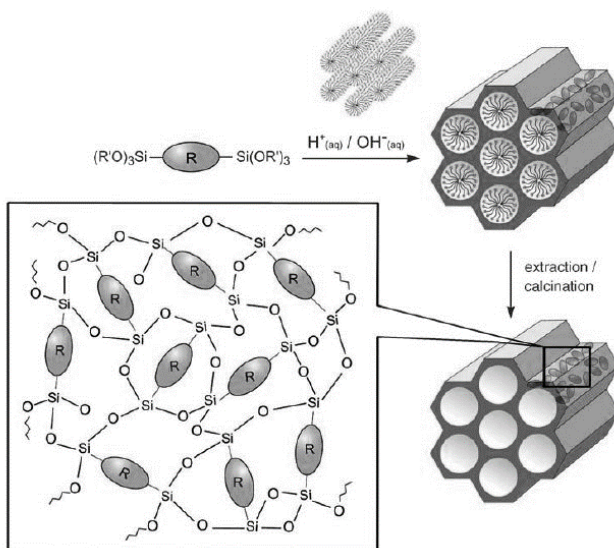
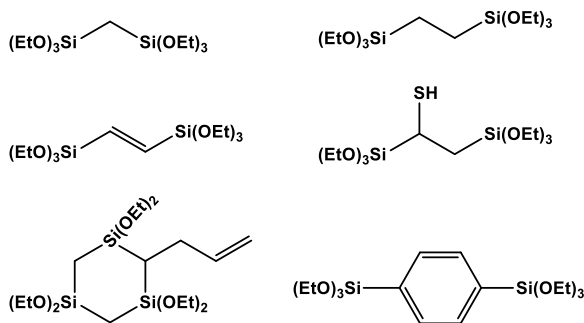


Figure 1.6. The PMO synthesis process.⁴

However, the choice of R should be limited to small and rigid functional groups in order to obtain the desired ordered pore structure. For instance, PMO precursors containing methyl, ethyl, ethene, allyl, thio-ethyl and phenyl moieties can be used without any other precursor

(Scheme 1.3). In the case of larger organic moieties, co-condensation with TEOS or a smaller PMO precursor is often required in order to obtain an ordered mesostructure. Nowadays, many simple and complex PMO precursors have been reported and PMO materials are investigated for applications in catalysis, adsorption, chromatography, low-*k* materials and more.¹¹



Scheme 1.3. A selection of small, rigid PMO precursors.

1.3 The three COMOC PMOs and the thiol-ene click reaction

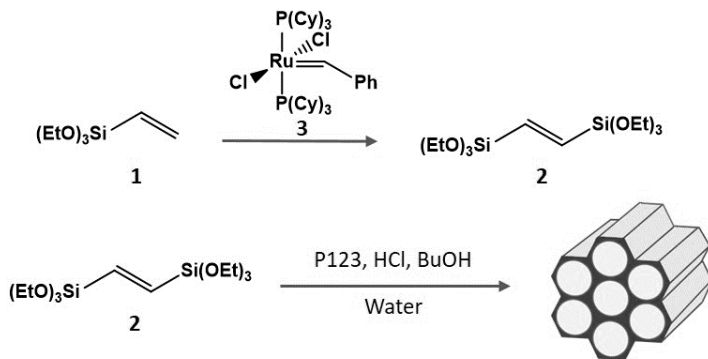
In the COMOC research group (Center for Ordered Materials, Organometallics and Catalysis), we mainly focus on PMOs with functional bridges which provide a wide variety of possibilities for further functionalization, with applications in catalysis, adsorption and chromatography in mind. Three different PMOs have been developed over the years, namely an ethene PMO, an allyl ring PMO and a thiol PMO. All three use P123 as SDA, which gives them mesopore sizes of around 5 nm and a 2D hexagonal pore structure. Since all three of these PMOs play a part in the research presented in this dissertation, each one of these COMOC PMOs is presented in more detail hereafter. An overview of the thiol-ene click reaction, which plays an important role in this work, is also given.

1.3.1 The 100% trans ethene PMO (or ePMO)

The first report of an ethene PMO appeared in the pioneering PMO papers of 1999, published by the groups of Stein⁷ and Ozin⁸. They used the commercial ethene precursor (1,2-bis(triethoxysilyl)ethene), which consists of roughly 80% trans and 20% cis isomer. The synthesis was performed in basic conditions with CTAB as template. Both groups also reported for the first time the bromination of the double bonds on the solid. Later, the synthesis of ethene PMOs was extended with the use of different templates as well as acidic reaction conditions.

However, as early as 1998, even before the emergence of PMOs, a method for isolating the trans precursor by vacuum distillation was reported. The 100% trans precursor was then used to form a xerogel in a non-templated sol-gel synthesis.¹² The first account of a PMO material using the 100% trans precursor was reported by Xia et al.¹³, who produced porous microspheres using dodecyltrimethylammonium bromide (DTAB) as template. They also showed a molecular-level ordering of the material caused by stacking of the double bonds, as evidenced by an XRD signal at 16.5°.

The difference between PMOs formed with a mixture of isomers and a 100% trans precursor was investigated in our research group by Vercaemst et al. (Scheme 1.4).¹⁴ They found that the 100% trans precursor **2** can be selectively synthesized by the self-metathesis reaction of vinyltriethoxysilane (**1**), using Grubbs' first generation catalyst (**3**).



Scheme 1.4. Synthesis scheme for the 100% trans PMO precursor and the 'ultrafast' ePMO synthesis.

A mixture of cis and trans precursors could be obtained by a similar procedure, using $\text{RuCl}_2(\text{PPh}_3)_3$ as catalyst. From this mixture, the pure cis precursor could be obtained by successive fractional distillations. In this way, a series of PMO materials was synthesized, using different ratios of the cis and trans precursors and using P123 as template. Figure 1.7 shows the XRD patterns of these materials. It is clear that the ordering of the PMO materials improves with increasing trans precursor content.¹⁴ The material made from pure trans precursor shows well-defined secondary reflections at 1.5° and 1.8°, indicating excellent long-range ordering of the pore structure. This material also exhibits the most narrow pore size distribution. It was also shown that the pure trans PMO has a significantly better hydrothermal stability than the PMO formed by a mixture of 80% trans and 20% cis precursors.

Vercaemst et al. also optimized the synthesis of the pure trans ethene PMO in acidic conditions with P123 as template and butanol as additive. This resulted in an 'ultra-fast

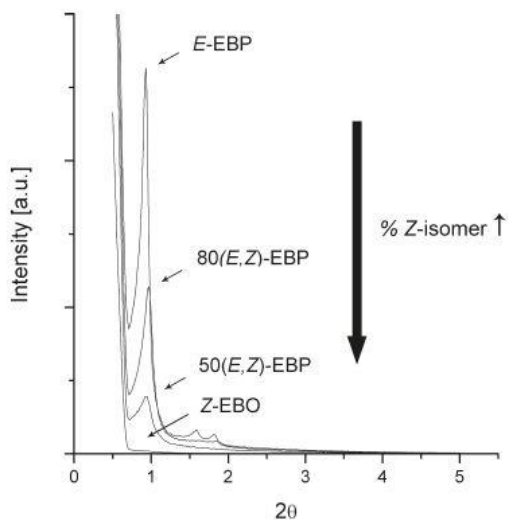
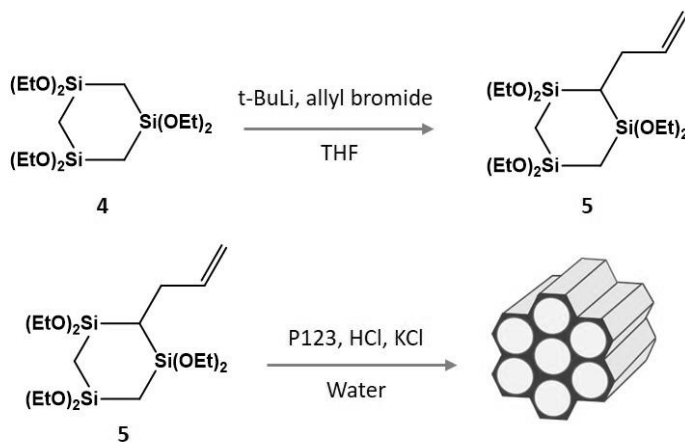


Figure 1.7. XRD patterns of PMO materials synthesized with different ratios of cis and trans ePMO precursors (E=trans, Z=cis).¹⁴

synthesis procedure' which only takes two days to complete (Scheme 1.4).¹⁵ The PMO obtained in this optimized synthesis procedure, using the 100% pure trans precursor, became the standard ethene PMO used in our research group and will further on be denoted as the 'ePMO'.

1.3.2 The monoallyl ring PMO (or mAR-PMO)

PMOs containing six-membered rings bearing three alkoxy silane moieties were first reported by the group of Ozin in 2003.¹⁶ 1,3,5-tris[diethoxysila]cyclohexane (Scheme 1.5, **4**)

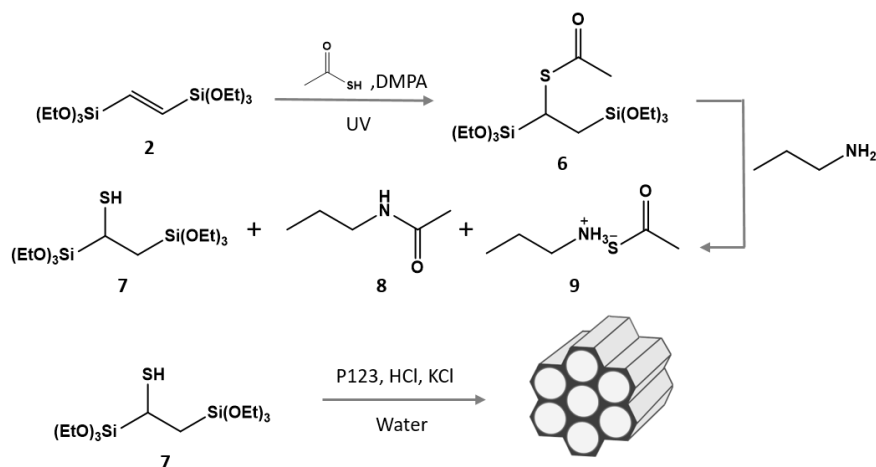


Scheme 1.5. Synthesis scheme for the monoallyl ring precursor and PMO.

is now a commercial precursor, but it doesn't contain any functional groups that could be used for further modifications. Ide et al.¹⁷ developed an allylation procedure, using tert-butyl lithium (t-BuLi) and allyl bromide as reagents. This introduced a useful functionality to this ring PMO precursor. However, over-allylation occurred in this reaction, yielding mono, bis and tris-allylated ring precursors. Clerick et al.¹⁸ further elaborated on this procedure by tuning the reaction parameters and were able to avoid the over-allylation completely. The mono-allylated ring precursor (**5**) could then easily be isolated via flash column chromatography. They also developed the synthesis of a well-ordered, P123-templated PMO containing 100% of the mono-allylated precursor (Scheme 1.5). This optimized PMO will further be denoted as the 'monoallyl ring PMO' (mAR-PMO). This PMO offers remarkable stability in water, withstanding pH values ranging from 0 to 13.

1.3.3 The thiol PMO

A PMO precursor containing a functional thiol group was developed by Esquivel et al.¹⁹ (Scheme 1.6). The synthesis starts from the ethene PMO precursor, which undergoes a thiol acid-ene click reaction with thioacetic acid. This reaction is a variation on the classic thiol-ene click reaction, which forms a thioether moiety from a thiol and a double bond (see section 1.3.4). After the formation of the thioester (**6**), hydrolysis by propylamine yields the thiol precursor (**7**). During this procedure, two side products are formed, namely the amide formed after the nucleophilic substitution with propylamine (**8**) and the salt formed by the excess of thioacetic acid and the excess of propylamine (**9**). However, despite these impurities, the thiol precursor can be used in the PMO synthesis without purification, as the side products dissolve in the reaction medium and are filtered off after the PMO formation.



Scheme 1.6. Synthesis scheme for the thiol precursor and PMO. (DMPA = 2,2-Dimethoxy-2-phenylacetophenone)

The thiol PMO is formed in an acidic medium, with P123 as template and KCl as additive (Scheme 1.6). This results in a 100% thiol PMO, with a sulfur loading of around 4 mmol/g. If a lower loading of thiol groups is desired, the thiol precursor can be co-condensed with 1,2-bis(triethoxysilyl)ethane (BTEE). The sulfur content of the resulting PMOs is then directly proportional to the ratio of precursors used.

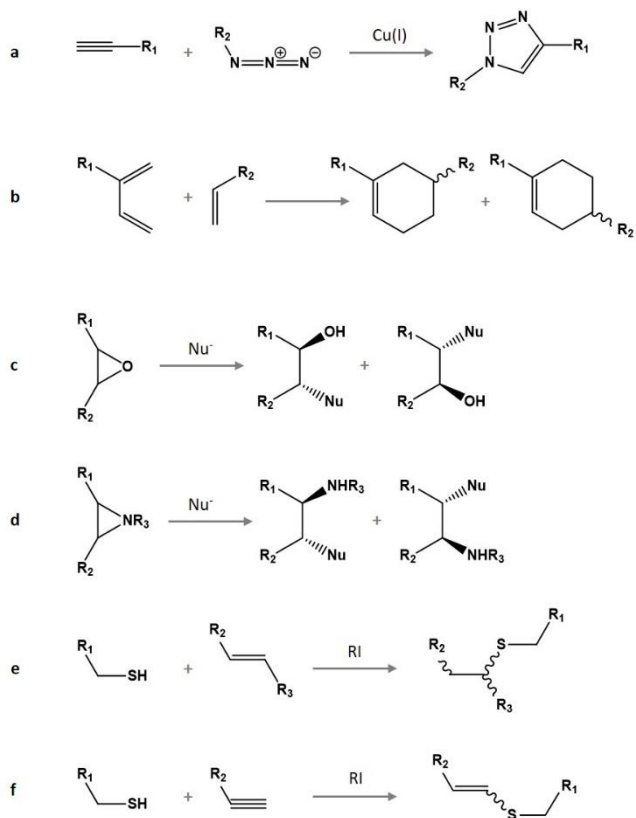
1.3.4 A closer look at the thiol-ene click reaction

The term 'click chemistry' was first introduced by Sharpless in 2001.²⁰ It describes a set of reactions, which share a set of assets that makes them versatile, environmentally friendly and easy to perform. The criteria that a reaction should meet in order to fall into the click category are as follows. The reaction should tolerate the presence of a variety of functional groups. It should be wide in scope and give high yields. It should be highly selective and if byproducts are formed, they should be benign. The reaction should be performed in water or solvent-free ideally, or else in an easily removed solvent. The reaction conditions should be easy and the reagents readily available. The workup of the reaction should be simple and not include column purification steps. With such a list of requirements, only few reactions can be considered as click reactions, owing their rapid completion and high selectivity to a high thermodynamic driving force (over 20 kcal/mol).

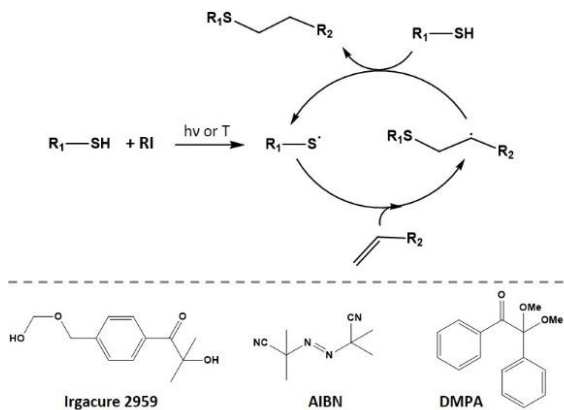
Some examples of click reactions are listed in Scheme 1.7. The most well-known one is the copper-catalyzed Huisgen reaction (**a**). This is a [3+2] cycloaddition of an azide and an acetylene to form a triazole ring. The Diels-Alder reaction (**b**), a [4+2] cycloaddition of an ene and a diene is also considered a click reaction. Another type of click reaction includes the nucleophilic ring-opening of epoxides (**c**) and aziridines (**d**). Finally, the thiol-ene click reaction (**e**) joins an alkene and a thiol to form a thioether bond. A variation of this reaction type is the thiol-yne reaction (**f**).

The thiol-ene click reaction proceeds via a radical mechanism, which is shown in Scheme 1.8.²¹ The reaction is started by a radical initiator, which can be activated thermally or by UV irradiation. Some typical UV-initiators are azobisisobutyronitrile (AIBN), 2-Hydroxy-4'-(2-hydroxyethoxy)-2-methylpropiophenone (Irgacure 2959) and 2,2-Dimethoxy-2-phenylacetophenone (DMPA). DMPA and Irgacure 2959 are UV-activated, while AIBN is thermally activated. AIBN and DMPA are soluble in a range of organic solvents, while Irgacure 2959 is soluble in water. Hence, by a strategic choice of radical initiator, the thiol-ene reaction can be performed in a variety of reaction conditions.

In this work, the thiol-ene reaction was used to functionalize PMO materials (Chapters 3 and 4). We found that the reaction proceeds readily when using solids, albeit significantly more slowly than in the homogeneous case. The reaction can be performed in both



Scheme 1.7. A selection of click reactions. (RI = radical initiator)



Scheme 1.8. The thiol-ene click mechanism and three radical initiators (RI).

directions, meaning that either the thiol or the alkene functionality can be present in the PMO material, with the compound containing the opposing functionality dissolved in the reaction medium.

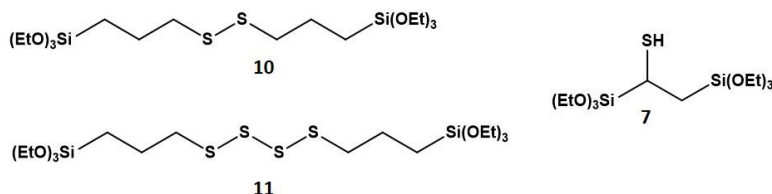
1.4 State of the art in functional PMOs and their applications

Two general strategies exist for the synthesis of functional PMOs for specific applications. The first is to incorporate a functionality into a PMO precursor, followed by the material synthesis. In this case, co-condensation with TEOS or a small PMO precursor (e.g. BTEE) is often needed. The second strategy is to form a PMO with a small functional precursor, such as an ethylene, allyl or phenyl group, and then post-functionalize the PMO bridge.

1.4.1 PMO synthesis using functional precursors

Over the years, many functional PMO precursors have been reported. They range from small and rigid precursors to large and complex, sometimes chiral ligands. A selection of the state of the art of these PMOs and their applications is summarized below.

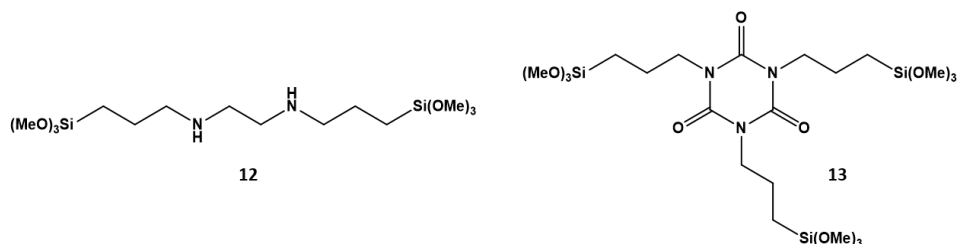
Due to the high affinity of sulfur and mercury, sulfur-functionalized materials can act as adsorbents for mercury ions in aqueous solutions (Scheme 1.9). A disulfide-bridged PMO was proposed by Hao et al.²² This material contained 20 mol% of the disulfide precursor (**10**) and could adsorb 716 mg/g of Hg²⁺. Zhang et al.²³ reported a tetrasulfide PMO based on **11** with an exceptionally high Hg²⁺ adsorption capacity of 2710 mg/g. However, the material, which contained 15 mol% of the tetrasulfide precursor, had a low surface area and stability, and reuse of the adsorbent was not successful. Esquivel et al.²⁴ applied the 100% thiol PMO (**7**) in mercury adsorption. This PMO could adsorb 1180 mg/g Hg²⁺, with good reusability.



Scheme 1.9. A selection of sulfur-containing PMO precursors.

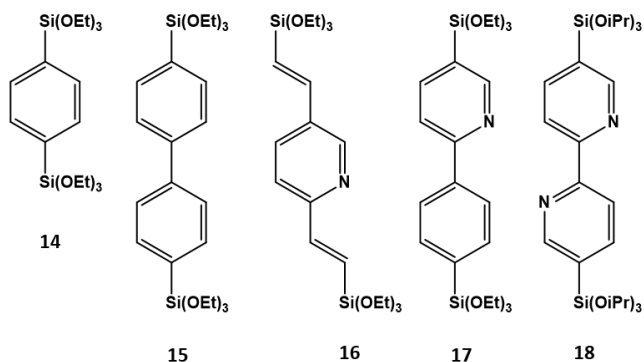
Nitrogen-based PMO precursors are also of interest for applications in adsorption and catalysis (Scheme 1.10). Zhu et al.²⁵ formed a PMO by co-condensation of BTEE and an ethylene diamine precursor (**12**). They also added Cu²⁺ ions during the synthesis, to optimize the conformation of the amino groups inside the PMO material. After removal of the copper ions, the molecularly imprinted PMO was shown to be a selective adsorbent for Cu²⁺. Zhu et al. showed that an ethylene diamine PMO could also be used as an effective base catalyst in Knoevenagel, Henry and Michael reactions.²⁶ Other nitrogen-bearing PMO precursors of

interest include an isocyanurate precursor (**13**) proposed by Olkhovyk et al.²⁷ A PMO containing 75% of this precursor and 25% TEOS was found to be an excellent adsorbent for Hg^{2+} , with an adsorption capacity of 1800 mg/g.



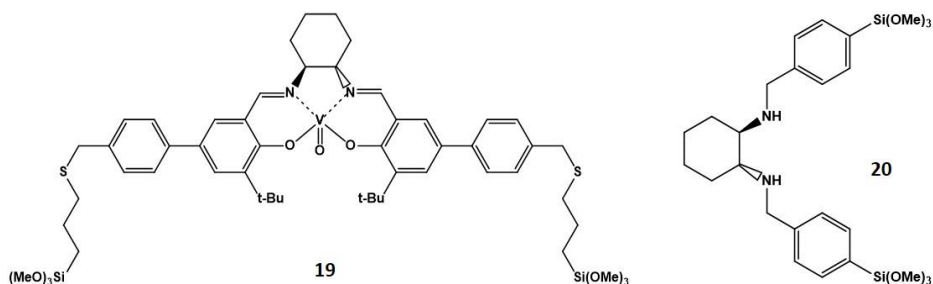
Scheme 1.10. A selection of nitrogen-containing PMO precursors.

Inagaki and his group made an important contribution to the development of functional PMOs with molecular-scale ordering. They developed phenyl,²⁸ biphenyl,²⁹ pyridine,³⁰ phenyl-pyridine³¹ and bipyridine³² PMOs (Scheme 1.11, **14-18**), without co-condensation of any other silica source. All these PMOs show crystal-like properties due to pi-pi stacking within the pore walls. In particular, the bipyridine PMO based on **18** proved to have many applications as a solid metal ligand. For instance, an Ir-complex grafted onto the bipyridine PMO was used as an efficient catalyst for the C-H borylation of benzene.³³ A Ru-complex immobilized on the same PMO, along with Pt nanoparticles, could successfully be used as a photosensitizer, for the production of H_2 with light in the visible spectrum.³² Several more applications for this PMO were reported.³⁴⁻³⁶



Scheme 1.11. A selection of PMO precursors reported by the group of Inagaki.

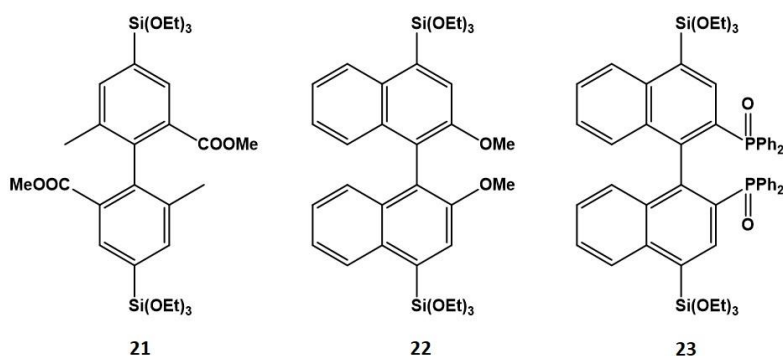
Baleizao et al.³⁷ were the first to report a chiral PMO precursor (Scheme 1.12, **19**). They modified a vanadyl Salen complex with silanes on both extremities to obtain a bis-silane. Co-condensation with at least 85% TEOS was necessary to form the PMO material, but the end product was proven to have chiral properties. The PMO catalyzed the cyanosilylation



Scheme 1.12. A selection of chiral PMO precursors.

of benzaldehyde, albeit with a lower enantioselectivity (*ee*) than the homogeneous vanadyl complex. PMO precursors containing chiral diamines (**20**) were prepared and co-condensed with TMOS to form chiral PMOs. These materials were then post-functionalized with Rh-complexes and used in the catalysis of an asymmetric hydrogen transfer reaction, achieving *ee* values of up to 60%.³⁸

Another route for incorporating chirality in PMOs was reported by the group of Cruden. They synthesized several axially chiral PMO precursors³⁹⁻⁴¹ (Scheme 1.13, **21-23**), which were co-condensed with a biphenyl PMO precursor. The resulting materials were shown to have chiral properties. In particular, the BINAP (2,2'-bis(diphenylphosphino)-1,1'-binaphthyl) based PMO (**23**) is of interest for catalytic applications. This material shows molecular-scale ordering inside the pore walls, but the BINAP loading is limited to 5%. The BINAP functionalities were further modified by reduction and grafting of a Ru-complex. This PMO shows remarkable activity and enantioselectivity in the asymmetric hydrogenation of β -ketoesters, reaching 99% *ee*.⁴¹ Further examples of chirality in PMOs can be found in a review on this topic.⁴²

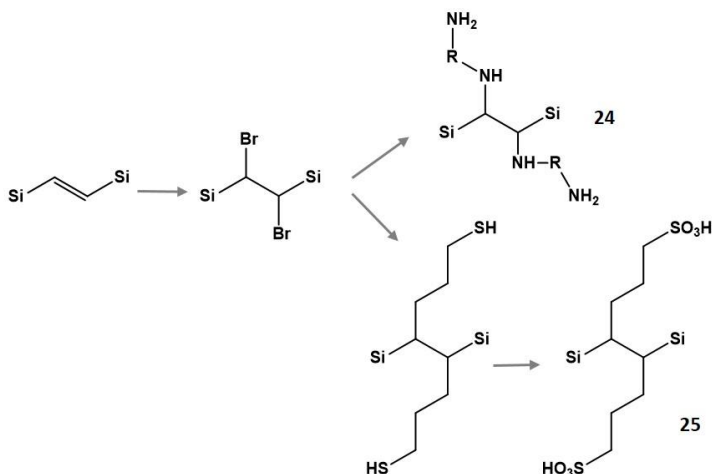


Scheme 1.13. A selection of axially chiral PMO precursors reported by the group of Cruden.

1.4.2 Post-modification of PMOs

Instead of synthesizing complex PMO precursors, PMOs containing small functional moieties can be modified after the material synthesis. This approach offers the advantage that the mesostructure of the PMO is retained and no co-condensation with TEOS is required. However, organic transformations, as well as the analysis of the obtained product, are often more challenging on the material than in the corresponding homogeneous reaction. The compatibility of the PMO with the reaction conditions should also be taken into consideration. Harsh basic conditions for example, should be avoided in most cases. Nonetheless, several examples of such post-modifications have been reported, for instance on ethene, allyl and phenyl PMOs. A selection of these post-modifications is summarized below.

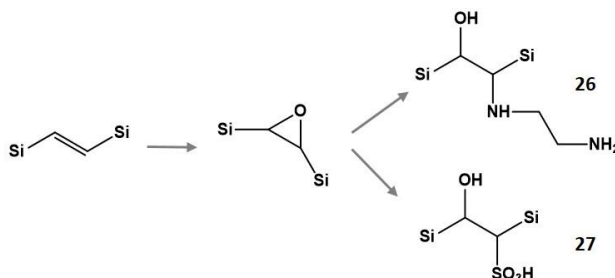
The double bond contained within ethene PMOs offers several possibilities for post-modification. Bromination of the double bond can be achieved by a direct reaction with bromine gas. This reaction can be used for gravimetric quantification of the double bonds, but also for further modifications (Scheme 1.14). Nakai et al.⁴³ followed the bromination of the double bond by a substitution with ethylene diamine to yield a primary amine-functionalized PMO (**24**), which was applied in the adsorption of arsenate. A similar approach was used on the ePMO by De Canck et al.⁴⁴, yielding several aminated PMOs that were used in CO₂ adsorption. Similarly, they also incorporated sulfonic acid groups on an ePMO.⁴⁵ Bromination of the double bond was followed by substitution with a Grignard



Scheme 1.14. A schematic representation of the post-modification of ethene PMOs via bromination.

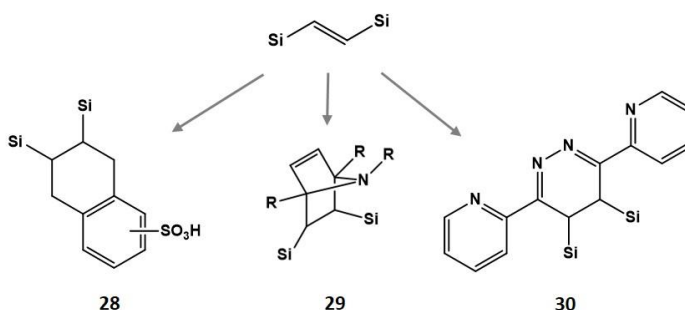
reagent to yield thiol groups and finally oxidation towards the sulfonic acid (**25**). This solid acid catalyst was applied in an esterification reaction.

Another way to introduce acid and basic functional groups is via epoxidation of the double bond using TBHP (tert-butyl hydroxyperoxide), followed by nucleophilic substitution (Scheme 1.15). Horiuchi et al.⁴⁶ used ethylene diamine after the epoxidation to yield the primary amine functionalization (**26**). Gold nanoparticles were then deposited on the PMO and the material was applied in tandem oxidation and Knoevenagel reactions. Sasidharan et al.⁴⁷ obtained an acid-functionalized PMO by means of sulfonation of the epoxide (**27**). This solid acid catalyst was applied in an esterification reaction.



Scheme 1.15. A schematic representation of the post-modification of ethene PMOs via epoxidation.

Another possible modification makes use of the Diels-Alder reaction (Scheme 1.16). Nakajima et al.⁴⁸ performed a Diels-Alder reaction on an ethene PMO with benzocyclobutene, followed by sulfonation of the aromatic ring, yielding a solid acid catalyst (**28**). Esquivel et al.⁴⁹ modified the ePMO via Diels-Alder reactions, yielding a range of pyrrole-functionalized PMOs (**29**). This Diels-Alder strategy was then extended to a tetrazine



Scheme 1.16. A schematic representation of the post-modification of ethene PMOs via Diels-Alder reactions.

with only a minor loss in surface area and ordered structure. The aminated PMO was successfully used as base catalyst in a Knoevenagel reaction. Huybrechts et al.⁵⁴ further modified the amine functionality with L-serine (**35**), yielding a catalyst for the Aldol reaction. The phenyl PMO can also be directly sulfonated with a $\text{SO}_3/\text{H}_2\text{SO}_4$ treatment to yield an acid catalyst (**36**), as reported by Inagaki et al.²⁸

In conclusion, many different pathways are available to incorporate interesting functionalities into PMO materials. These, combined with the porosity, stability and versatility of PMOs make them useful materials in a wide range of applications.

1.5 References

- [1] J.S. Beck, J.C. Vartuli, W.J. Roth, M.E. Leonowicz, C.T. Kresge, K.D. Schmitt, C.T.W. Chu, D.H. Olson, E.W. Sheppard, S.B. McCullen, J.B. Higgins, J.L. Schlenker, A NEW FAMILY OF MESOPOROUS MOLECULAR-SIEVES PREPARED WITH LIQUID-CRYSTAL TEMPLATES, *Journal of the American Chemical Society*, 114 (1992) 10834-10843.
- [2] D.Y. Zhao, J.L. Feng, Q.S. Huo, N. Melosh, G.H. Fredrickson, B.F. Chmelka, G.D. Stucky, Triblock copolymer syntheses of mesoporous silica with periodic 50 to 300 angstrom pores, *Science*, 279 (1998) 548-552.
- [3] F. Hoffmann, M. Froba, Vitalising porous inorganic silica networks with organic functions-PMOs and related hybrid materials, *Chemical Society Reviews*, 40 (2011) 608-620.
- [4] F. Hoffmann, M. Cornelius, J. Morell, M. Froba, Silica-based mesoporous organic-inorganic hybrid materials, *Angewandte Chemie-International Edition*, 45 (2006) 3216-3251.
- [5] A. Zurner, J. Kirstein, M. Doblinger, C. Brauchle, T. Bein, Visualizing single-molecule diffusion in mesoporous materials, *Nature*, 450 (2007) 705-709.
- [6] S. Inagaki, S. Guan, Y. Fukushima, T. Ohsuna, O. Terasaki, Novel mesoporous materials with a uniform distribution of organic groups and inorganic oxide in their frameworks, *Journal of the American Chemical Society*, 121 (1999) 9611-9614.
- [7] B.J. Melde, B.T. Holland, C.F. Blanford, A. Stein, Mesoporous sieves with unified hybrid inorganic/organic frameworks, *Chemistry of Materials*, 11 (1999) 3302-3308.
- [8] T. Asefa, M.J. MacLachlan, N. Coombs, G.A. Ozin, Periodic mesoporous organosilicas with organic groups inside the channel walls, *Nature*, 402 (1999) 867-871.
- [9] D. Esquivel, C. Jimenez-Sanchidrian, F.J. Romero-Salguero, Comparison of the thermal and hydrothermal stabilities of ethylene, ethylidene, phenylene and biphenylene bridged periodic mesoporous organosilicas, *Materials Letters*, 65 (2011) 1460-1462.
- [10] G. Smeulders, V. Meynen, A. Silvestre-Albero, K. Houthoofd, M. Mertens, J. Silvestre-Albero, J.A. Martens, P. Cool, The impact of framework organic functional groups on the hydrophobicity and overall stability of mesoporous silica materials, *Materials Chemistry and Physics*, 132 (2012) 1077-1088.
- [11] P. Van der Voort, D. Esquivel, E. De Canck, F. Goethals, I. Van Driessche, F.J. Romero-Salguero, Periodic Mesoporous Organosilicas: from simple to complex bridges; a comprehensive overview of functions, morphologies and applications, *Chemical Society Reviews*, 42 (2013) 3913-3955.

- [12] D.A. Loy, J.P. Carpenter, S.A. Yamanaka, M.D. McClain, J. Greaves, S. Hobson, K.J. Shea, Polymerization of bis(triethoxysilyl) ethenes. Impact of substitution geometry on the formation of ethenylene- and vinylidene-bridged polysilsesquioxanes, *Chemistry of Materials*, 10 (1998) 4129-4140.
- [13] Y.D. Xia, R. Mokaya, Surfactant mediated control of pore size and morphology for molecularly ordered ethylene-bridged periodic mesoporous organosilica, *Journal of Physical Chemistry B*, 110 (2006) 3889-3894.
- [14] C. Vercaemst, M. Ide, P.V. Wiper, J.T.A. Jones, Y.Z. Khimyak, F. Verpoort, P. Van Der Voort, Ethenylene-Bridged Periodic Mesoporous Organosilicas: From E to Z, *Chemistry of Materials*, 21 (2009) 5792-5800.
- [15] C. Vercaemst, M. Ide, B. Allaert, N. Ledoux, F. Verpoort, P. Van der Voort, Ultra-fast hydrothermal synthesis of diastereoselective pure ethenylene-bridged periodic mesoporous organosilicas, *Chemical Communications*, (2007) 2261-2263.
- [16] K. Landskron, B.D. Hatton, D.D. Perovic, G.A. Ozin, Periodic mesoporous organosilicas containing interconnected Si(CH₂)₃ rings, *Science*, 302 (2003) 266-269.
- [17] M. Ide, E. De Canck, I. Van Driessche, F. Lynen, P. Van der Voort, Developing a new and versatile ordered mesoporous organosilica as a pH and temperature stable chromatographic packing material, *Rsc Advances*, 5 (2015) 5546-5552.
- [18] S. Clerick, E. De Canck, K. Hendrickx, V. Van Speybroeck, P. Van der Voort, Heterogeneous Ru(III) oxidation catalysts via 'click' bidentate ligands on a periodic mesoporous organosilica support, *Green Chemistry*, 18 (2016) 6035-6045.
- [19] D. Esquivel, O. van den Berg, F.J. Romero-Salguero, F. Du Prez, P. Van Der Voort, 100% thiol-functionalized ethylene PMOs prepared by "thiolacid-ene" chemistry, *Chemical Communications*, 49 (2013) 2344-2346.
- [20] H.C. Kolb, M.G. Finn, K.B. Sharpless, Click chemistry: Diverse chemical function from a few good reactions, *Angewandte Chemie-International Edition*, 40 (2001) 2004-2021.
- [21] A.B. Lowe, Thiol-ene "click" reactions and recent applications in polymer and materials synthesis, *Polymer Chemistry*, 1 (2010) 17-36.
- [22] N. Hao, L. Han, Y.X. Yang, H.T. Wang, P.A. Webley, D.Y. Zhao, A metal-ion-assisted assembly approach to synthesize disulfide-bridged periodical mesoporous organosilicas with high sulfide contents and efficient adsorption, *Applied Surface Science*, 256 (2010) 5334-5342.

- [23] L.X. Zhang, W.H. Zhang, J.L. Shi, Z. Hua, Y.S. Li, J. Yan, A new thioether functionalized organic-inorganic mesoporous composite as a highly selective and capacious Hg²⁺ adsorbent, *Chemical Communications*, (2003) 210-211.
- [24] D. Esquivel, J. Ouwehand, M. Meledina, S. Turner, G. Van Tendeloo, F.J. Romero-Salguero, J. De Clercq, P. Van Der Voort, Thiol-ethylene bridged PMO: A high capacity regenerable mercury adsorbent via intrapore mercury thiolate crystal formation, *Journal of Hazardous Materials*, 339 (2017) 368-377.
- [25] H.G. Zhu, D.J. Jones, J. Zajac, R. Dutartre, M. Rhomari, J. Roziere, Synthesis of periodic large mesoporous organosilicas and functionalization by incorporation of ligands into the framework wall, *Chemistry of Materials*, 14 (2002) 4886-4894.
- [26] F.X. Zhu, P.S. Zhao, X.J. Sun, L.T. An, Y. Deng, J.M. Wu, Direct synthesis and application of bridged diamino-functionalized periodic mesoporous organosilicas with high nitrogen contents, *Journal of Solid State Chemistry*, 255 (2017) 70-75.
- [27] O. Olkhoviyk, M. Jaroniec, Periodic mesoporous organosilica with large heterocyclic bridging groups, *Journal of the American Chemical Society*, 127 (2005) 60-61.
- [28] S. Inagaki, S. Guan, T. Ohsuna, O. Terasaki, An ordered mesoporous organosilica hybrid material with a crystal-like wall structure, *Nature*, 416 (2002) 304-307.
- [29] M.P. Kapoor, Q.H. Yang, S. Inagaki, Self-assembly of biphenylene-bridged hybrid mesoporous solid with molecular-scale periodicity in the pore walls, *Journal of the American Chemical Society*, 124 (2002) 15176-15177.
- [30] M. Waki, N. Mizoshita, T. Ohsuna, T. Tani, S. Inagaki, Crystal-like periodic mesoporous organosilica bearing pyridine units within the framework, *Chemical Communications*, 46 (2010) 8163-8165.
- [31] M. Waki, N. Mizoshita, T. Tani, S. Inagaki, Periodic Mesoporous Organosilica Derivatives Bearing a High Density of Metal Complexes on Pore Surfaces, *Angewandte Chemie-International Edition*, 50 (2011) 11667-11671.
- [32] M. Waki, Y. Maegawa, K. Hara, Y. Goto, S. Shirai, Y. Yamada, N. Mizoshita, T. Tani, W.J. Chun, S. Muratsugu, M. Tada, A. Fukuoka, S. Inagaki, A Solid Chelating Ligand: Periodic Mesoporous Organosilica Containing 2,2'-Bipyridine within the Pore Walls, *Journal of the American Chemical Society*, 136 (2014) 4003-4011.
- [33] Y. Maegawa, S. Inagaki, Iridium-bipyridine periodic mesoporous organosilica catalyzed direct C-H borylation using a pinacolborane, *Dalton Transactions*, 44 (2015) 13007-13016.
- [34] N. Ishito, H. Kobayashi, K. Nakajima, Y. Maegawa, S. Inagaki, K. Hara, A. Fukuoka, Ruthenium-Immobilized Periodic Mesoporous Organosilica: Synthesis, Characterization,

and Catalytic Application for Selective Oxidation of Alkanes, *Chemistry-a European Journal*, 21 (2015) 15564-15569.

[35] Y. Kuramochi, M. Sekine, K. Kitamura, Y. Maegawa, Y. Goto, S. Shirai, S. Inagaki, H. Ishida, Photocatalytic CO₂ Reduction by Periodic Mesoporous Organosilica (PMO) Containing Two Different Ruthenium Complexes as Photosensitizing and Catalytic Sites, *Chemistry-a European Journal*, 23 (2017) 10301-10309.

[36] X. Liu, Y. Maegawa, Y. Goto, K. Hara, S. Inagaki, Heterogeneous Catalysis for Water Oxidation by an Iridium Complex Immobilized on Bipyridine-Periodic Mesoporous Organosilica, *Angewandte Chemie-International Edition*, 55 (2016) 7943-7947.

[37] C. Baleizao, B. Gigante, D. Das, M. Alvaro, H. Garcia, A. Corma, Synthesis and catalytic activity of a chiral periodic mesoporous organosilica (ChiMO), *Chemical Communications*, (2003) 1860-1861.

[38] D.M. Jiang, Q.H. Yang, H. Wang, G.R. Zhu, J. Yang, C. Li, Periodic mesoporous organosilicas with trans-(1R,2R)-diaminocyclohexane in the framework: A potential catalytic material for asymmetric reactions, *Journal of Catalysis*, 239 (2006) 65-73.

[39] S. MacQuarrie, M.P. Thompson, A. Blanc, N.J. Mosey, R.P. Lemieux, C.M. Crudden, Chiral Periodic Mesoporous Organosilicates Based on Axially Chiral Monomers: Transmission of Chirality in the Solid State, *Journal of the American Chemical Society*, 130 (2008) 14099-14101.

[40] X.W. Wu, T. Blackburn, J.D. Webb, A.E. Garcia-Bennett, C.M. Crudden, The Synthesis of Chiral Periodic Organosilica Materials with Ultrasmall Mesopores, *Angewandte Chemie-International Edition*, 50 (2011) 8095-8099.

[41] T. Seki, K. McEleney, C.M. Crudden, Enantioselective catalysis with a chiral, phosphane-containing PMO material, *Chemical Communications*, 48 (2012) 6369-6371.

[42] M.W.A. MacLean, L.M. Reid, X.W. Wu, C.M. Crudden, Chirality in Ordered Porous Organosilica Hybrid Materials, *Chemistry-an Asian Journal*, 10 (2015) 70-82.

[43] K. Nakai, Y. Oumi, H. Horie, T. Sano, H. Yoshitake, Bromine addition and successive amine substitution of mesoporous ethylenesilica: Reaction, characterizations and arsenate adsorption, *Microporous and Mesoporous Materials*, 100 (2007) 328-339.

[44] E. De Canck, I. Ascoop, A. Sayari, P. Van Der Voort, Periodic mesoporous organosilicas functionalized with a wide variety of amines for CO₂ adsorption, *Physical Chemistry Chemical Physics*, 15 (2013) 9792-9799.

- [45] E. De Canck, I. Dosuna-Rodriguez, E.M. Gaigneaux, P. Van der Voort, Periodic Mesoporous Organosilica Functionalized with Sulfonic Acid Groups as Acid Catalyst for Glycerol Acetylation, *Materials*, 6 (2013) 3556-3570.
- [46] Y. Horiuchi, D. Do Van, Y. Yonezawa, M. Saito, S. Dohshi, T.H. Kim, M. Matsuoka, Synthesis and bifunctional catalysis of metal nanoparticle-loaded periodic mesoporous organosilicas modified with amino groups, *Rsc Advances*, 5 (2015) 72653-72658.
- [47] M. Sasidharan, A. Bhaumik, Novel and Mild Synthetic Strategy for the Sulfonic Acid Functionalization in Periodic Mesoporous Ethenylene-Silica, *Acs Applied Materials & Interfaces*, 5 (2013) 2618-2625.
- [48] K. Nakajima, I. Tomita, M. Hara, S. Hayashi, K. Domen, J.N. Kondo, Development of highly active SO₃H-modified hybrid mesoporous catalyst, *Catalysis Today*, 116 (2006) 151-156.
- [49] D. Esquivel, E. De Canck, C. Jimenez-Sanchidrian, F.J. Romero-Salguero, P. Van der Voort, Pyrrole PMOs, incorporating new N-heterocyclic compounds on an ethene-PMO through Diels-Alder reactions, *Materials Chemistry and Physics*, 148 (2014) 403-410.
- [50] D. Esquivel, A.M. Kaczmarek, C. Jimenez-Sanchidrian, R. Van Deun, F.J. Romero-Salguero, P. Van der Voort, Eu³⁺@ PMO: synthesis, characterization and luminescence properties, *Journal of Materials Chemistry C*, 3 (2015) 2909-2917.
- [51] A.M. Kaczmarek, D. Esquivel, J. Ouwehand, P. Van der Voort, F.J. Romero-Salguero, R. Van Deun, Temperature dependent NIR emitting lanthanide-PMO/silica hybrid materials, *Dalton Transactions*, 46 (2017) 7878-7887.
- [52] C. Wu, Y. Liang, K.G. Yang, Y. Min, Z. Liang, L.H. Zhang, Y.K. Zhang, Clickable Periodic Mesoporous Organosilica Monolith for Highly Efficient Capillary Chromatographic Separation, *Analytical Chemistry*, 88 (2016) 1521-1525.
- [53] M. Ohashi, M.P. Kapoor, S. Inagaki, Chemical modification of crystal-like mesoporous phenylene-silica with amino group, *Chemical Communications*, (2008) 841-843.
- [54] W. Huybrechts, J. Lauwaert, A. De Vylder, M. Mertens, G. Mali, J.W. Thybaut, P. Van der Voort, P. Cool, Synthesis of L-serine modified benzene bridged periodic mesoporous organosilica and its catalytic performance towards aldol condensations, *Microporous and Mesoporous Materials*, 251 (2017) 1-8.

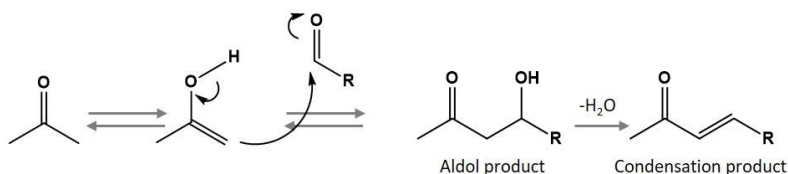
Chapter 2.

An introduction to cooperative enamine catalysis of aldol reactions

2.1 Enamine-catalysis of aldol reactions

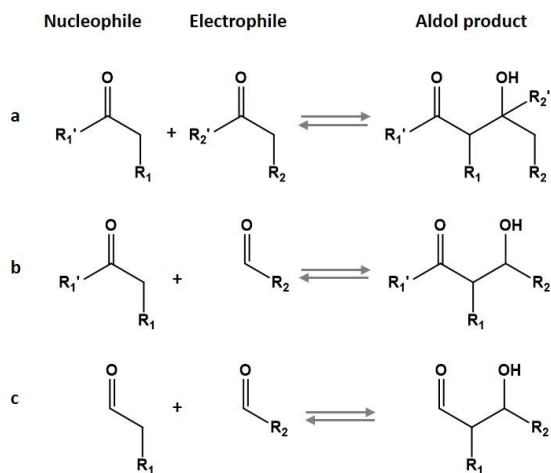
2.1.1 On the aldol reaction

Carbon-carbon coupling reactions are some of the most important reactions in organic chemistry. One of the most common of these is the aldol reaction, which couples two carbonyl compounds with the formation of an aldol adduct compound, which contains a ketone with an alcohol on the β -position. This product can then be dehydrated to form an α,β -unsaturated ketone. Of the two carbonyl compounds taking part in the aldol reaction, one acts as a nucleophile, while the other acts as an electrophile. The nucleophile, in its enol form, performs a nucleophilic attack on the electrophile to form the aldol product. From there, the condensation product can be formed by elimination of water. A general reaction scheme is shown in Scheme 2.1



Scheme 2.1. General reaction scheme of an aldol reaction.

In principle, three different combinations of reactants are possible, namely a combination of two ketones, a ketone and an aldehyde, or two aldehydes.¹ These are illustrated in Scheme 2.2. In practice, the ketone-ketone aldol reaction (**a**) is only feasible when using extremely reactive ketones as electrophiles, but in most cases the equilibrium for this reaction lies with the starting products. In a mixed aldol reaction between a ketone and an



Scheme 2.2. Aldol reactions between two ketones (a), a ketone and an aldehyde (b) and two aldehydes (c).

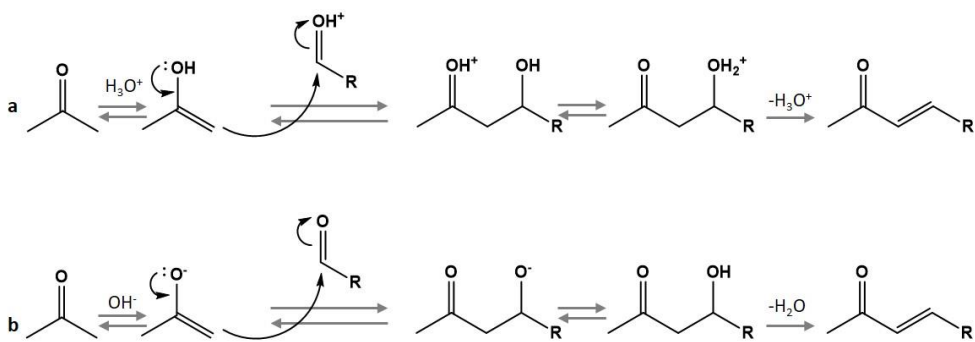
aldehyde (b), both the ketone and the aldehyde could act as the nucleophile, such that a mixture of aldol products would occur. This can be resolved by using a non-enolizable aldehyde. These are aldehydes with no proton in the α -position, so that the enol form cannot be formed. In addition, the ketone has to be symmetrical, or be non-enolizable on one side, in order to avoid mixed aldol products. An aldol reaction using two aldehydes (c) is also possible, although it is more difficult to avoid a mixture of products. One exception being the dimerization of a single aldehyde, which can only yield one aldol product. When using a mixture of aldehydes, the Mukaiyama aldol reaction can be employed to avoid multiple products.² Here, one of the aldehydes is transformed into a silyl enol ether, which essentially locks it in the enol form and forces it to act as the nucleophile. The other aldehyde is non-enolizable and therefore acts as the electrophile. However, this strategy requires one equivalent of enolating agent and is therefore no longer a purely catalytic process.

These requirements limit the scope of the aldol reaction. Generally, aromatic, non-enolizable aldehydes and symmetrical ketones are used as simple test reactions. Nonetheless, the aldol reaction has many applications, both in bulk and in fine chemistry. There are several examples of aldol condensation products produced on large scale. For example, the Aldox process, developed by Shell and Exxon, makes use of an aldol reaction for the synthesis of 2-ethylhexenal, which is produced at millions of tons per year.³ Aldol condensation products are also intermediates in the conversion of biomass to biofuel.⁴ In fine chemistry, aldol products are often used to induce chirality in the synthesis of complex organic molecules, such as pharmaceutical compounds.⁵

2.2

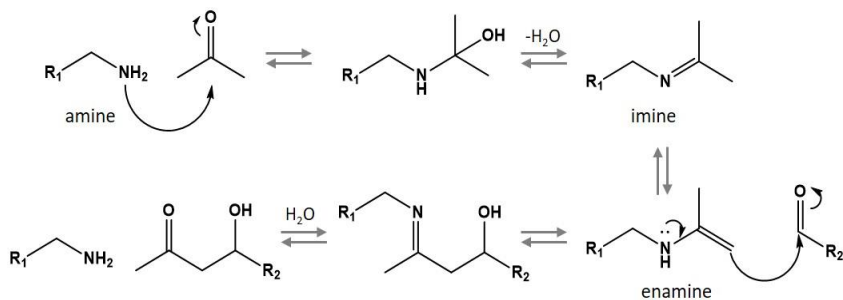
2.1.2 Aldol activation mechanisms: enol versus enamine intermediates

The aldol reaction can be acid or base-catalyzed. Both reaction pathways are illustrated in Scheme 2.3 (for simplicity, an aldol reaction between a symmetric ketone and a non-enolizable aldehyde is considered). The acid-catalyzed route (a) starts with the acid-mediated keto-enol tautomerization of the ketone. The aldehyde gets protonated by the acid, which activates the carbonyl bond. The enol performs a nucleophilic attack on the aldehyde, to form a protonated aldol product which can further form the unsaturated ketone via acid-catalyzed dehydration. Strong acids such as sulfuric acid and para-toluene sulfonic acid have been reported as catalysts for this process. In the base-catalyzed pathway (b), the enolate form of the ketone is formed. This compound then performs the nucleophilic attack on the aldehyde with the formation of the deprotonated aldol product. After protonation, the aldol product is obtained and the condensation product can be formed via base-catalyzed dehydration. Some commonly used bases for the aldol reaction are strong organic or inorganic bases such as sodium hydroxide and lithium di-isopropyl amide.



Scheme 2.3. The reaction mechanisms of the acid-catalyzed (a) and base-catalyzed (b) aldol reactions.

One downside of the acid and base-catalyzed aldol reactions is that strong acids and bases are required, which also inherently catalyze the dehydration of the aldol product. The selectivity towards the aldol product is therefore generally low. In the course of the last century, a third type of activation for the aldol reaction was discovered, namely the enamine-mediated aldol reaction.¹ The mechanism is shown in Scheme 2.4. This mechanism depends on the formation of an enamine intermediate from the ketone and a catalytic amine. Since the enamine is a stronger nucleophile than the corresponding enol, the nucleophilic attack on the aldehyde is enhanced. The catalytic amine is not effective for the dehydration of the aldol product, which can be largely avoided when the reaction temperature is not too high.

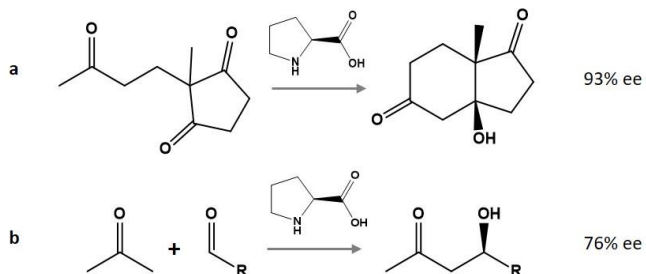


Scheme 2.4. The reaction mechanism of the enamine-catalyzed aldol reaction with a catalytic primary amine.

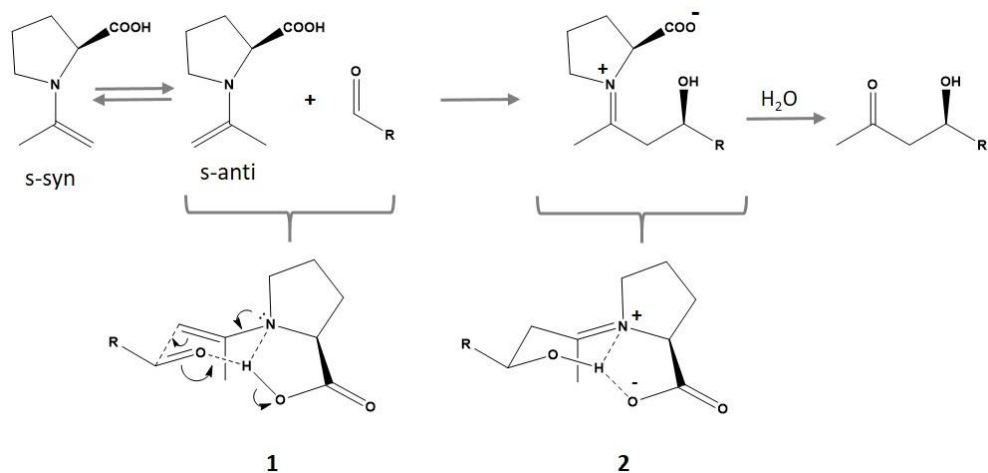
In the enamine-catalyzed aldol reaction, the presence of a weak acid can be beneficial. The role of the acid in that case is to increase the reactivity of the carbonyls towards nucleophilic attack. However, when using this cooperative enamine-acid mechanism, one should consider that the amine and the acid can neutralize each other. Two ways to prevent this are the use of a bifunctional homogeneous catalyst, which contains both the acid and the amine groups, or the use of a heterogeneous catalyst which contains both moieties. In the case of bifunctional homogeneous catalysts, enantioselective enamine catalysis becomes possible, which is discussed in the next section. Bifunctional heterogeneous enamine catalysts are discussed in section 2.2.2.

2.1.3 Enantioselective enamine catalysis

The discovery of enamine catalysis was largely inspired by the mechanism of aldolase enzymes, which perform aldol reactions via an enamine-activated mechanism. In the 1970's, a similar mechanism was discovered, which could be catalyzed by L-proline. The first proline-catalyzed aldol reaction was the intramolecular Hajos-Parrish-Eder-Sauer-Wiechert reaction⁶ (Scheme 2.5, reaction **a**). Only in the year 2000 was L-proline first used as catalyst in an intermolecular aldol reaction by List and Barbas⁷ (Scheme 2.5, reaction **b**). Both of these reactions were enantioselective towards the aldol product.



Scheme 2.5. Reaction schemes of the first enantioselective intramolecular (**a**) and intermolecular (**b**) reactions catalyzed by L-proline.



Scheme 2.6 The reaction scheme of the proline-catalyzed aldol reaction, with a representation of the most stable transition states.

The enantioselectivity of the proline-catalyzed aldol reaction can be explained by the intermediate configurations of the enamine mechanism, which are shown in Scheme 2.6. The enamine formed by proline and acetone can take on two conformations, namely the single-syn and the single-anti conformations (single refers to the N-C bond of the enamine moiety). The s-anti conformation forms much more stable transition states, hence it is this conformation which dictates the stereoselectivity. The s-anti enamine and the aldehyde form a chair-like configuration (**1**). The nucleophilic attack of the enamine on the aldehyde corresponds to a shift of electrons which yields the iminium configuration (**2**). Configurations **1** and **2** are stabilized by their chair conformation and by hydrogen bonding of the COOH group with the aldehyde. The favored equatorial position of the R-group of the aldehyde determines the orientation of the aldehyde and thus the stereoselectivity of the aldol product. Since the discovery of the unique catalytic activity of proline, many proline derivatives have been developed and applied in the formation of chiral carbon centers in the synthesis of countless organic compounds.⁵

2.2 Bifunctional (organo)silicas for cooperative enamine catalysis

As mentioned in section 2.2.1, heterogeneous catalysts can be used in the cooperative enamine catalysis of aldol reactions. These usually consist of functionalized mesoporous silica materials. An amine functionality can be incorporated via grafting or co-condensation (see also Chapter 1) of an aminosilane. The cooperative acidic site can be introduced via

another silane, or the silanol groups on the silica surface can act as the acid site. The synthesis and investigation of these materials is discussed below.

2.2.1 Incorporation of acid and basic sites onto mesoporous organosilicas

The first way to obtain a bifunctional acid-base solid catalyst is via the incorporation of a Brønsted acid and an amine onto the silica surface. The resulting materials offer unique catalytic properties that cannot be replicated in homogeneous catalysis, due to the mutual neutralization which would then occur between the acid and the base. These materials can be used in one-pot sequential reactions, where the acid and base functionalities catalyze separate reactions, or in cooperative acid-base catalysis.

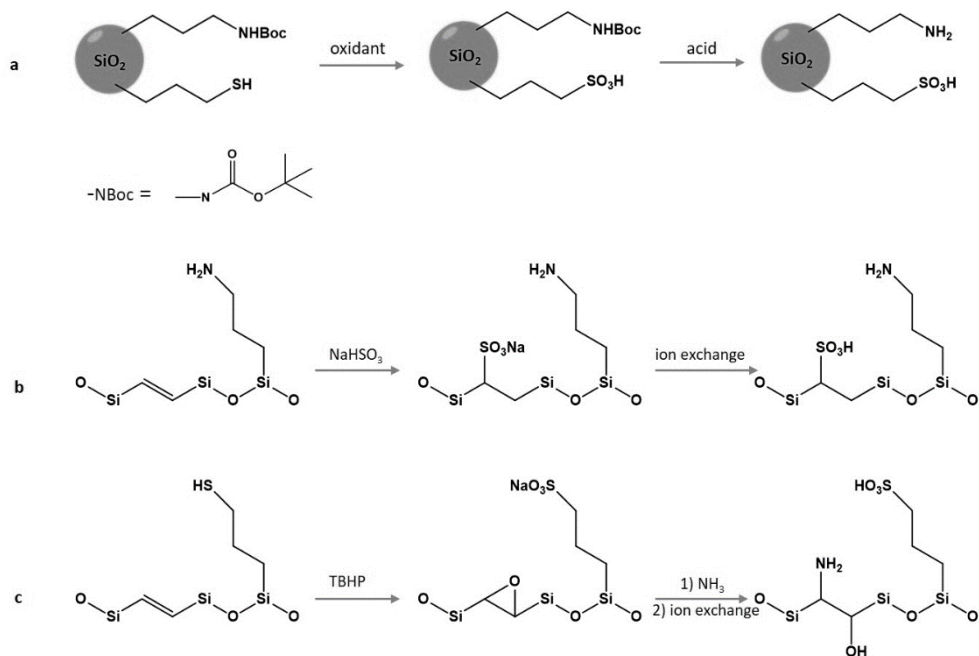
While bifunctional solid catalysts offer many opportunities, their synthesis is not necessarily straightforward. We have to consider the possibility of the acid and base interacting with each other during the synthesis, as well as the implication of each synthetic step on both functional groups. In the following section, different synthetic strategies that succeeded in these challenges are reviewed.

2.2.1.1 Heterogeneous bifunctional (organo)silicas in one-pot sequential catalysis

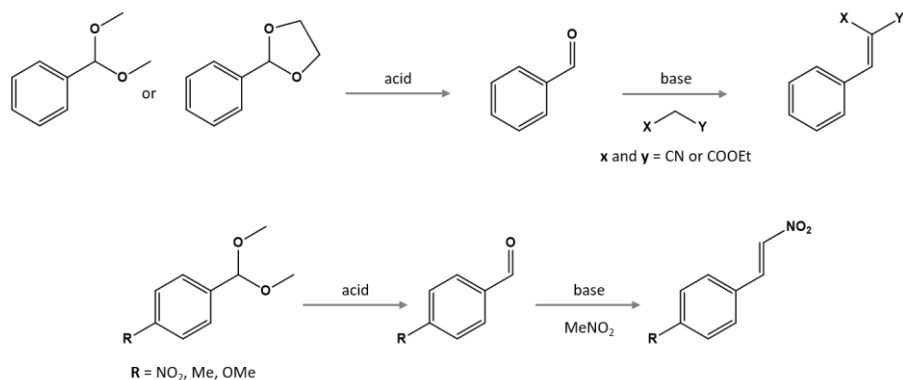
This section gives an overview of bifunctional acid-base functionalized (organo)silicas, with applications in sequential reactions. While these materials were not investigated as cooperative enamine catalysts, they are nonetheless interesting because of the variety of synthetic strategies used to incorporate the antagonistic acid and base sites.

A common strategy to incorporate acid and base sites on a mesoporous silica makes use of a Boc-protected aminosilane and a mercaptosilane (Scheme 2.7, **a**).^{8,9} Due to the Boc-group, they do not interact with each other during the synthesis. After the introduction of both functionalities (via grafting or co-condensation), the thiol group is oxidized to form a sulfonic acid, followed by the acid-mediated Boc-deprotection. The resulting material contains an acid and a base site. These types of materials can successfully be applied in typical one-pot sequential test reactions, namely the deprotection-Knoevenagel and the deprotection-Henry reactions (Scheme 2.8). In both reactions, the deprotection step consists of an acid-catalyzed deacetalization, yielding an aldehyde. The second step consists of a base-catalyzed reaction between the generated aldehyde and a second reagent. Both reactions are performed sequentially, without any workup in between.

A similar synthesis method was also developed for a PMO material, using the organic bridges in the material as anchoring points for the acid and base sites. Sasidharan et al.¹⁰ used an ethene PMO precursor, co-condensed with either an aminosilane or a mercaptosilane, to form two types of acid-base materials (Scheme 2.7, **b** and **c**). One material contains the amine as a dangling group (**b**) and the acid on the PMO surface, while the functionalities are reversed in the second material (**c**). They found that the material with



Scheme 2.7. Reaction schemes for the synthesis of bifunctional silica (a) or PMO (b and c) materials. TBHP = tert-butyl hydroperoxide.



Scheme 2.8. The sequential deprotection-Knoevenagel and deprotection-Henry reactions.

the dangling amine was more active in the sequential deprotection-Henry reaction. They postulated that the hydrophobic starting material reacts more readily with the acid in the hydrophobic micro-environment of the PMO pore, while the hydrophilic intermediate (the aldehyde) reacts more readily with the amine in the less hydrophobic micro-environment, further removed from the PMO surface.

When designing this type of material for a sequential reaction, several research groups also attempted the spatial separation of the acid and base sites by using core-shell nanoparticles.¹¹⁻¹³ A synthesis scheme for this type of particle is shown in Scheme 2.9. Even though the synthesized bifunctional particles were active in a sequential reaction, their reports show that a physical mixture of an acid-functionalized and a base-functionalized nanoparticle gave similar catalytic results. We can therefore state that, in the case of sequential catalysis, the synthesis of bifunctional acid-base materials is not strictly necessary.



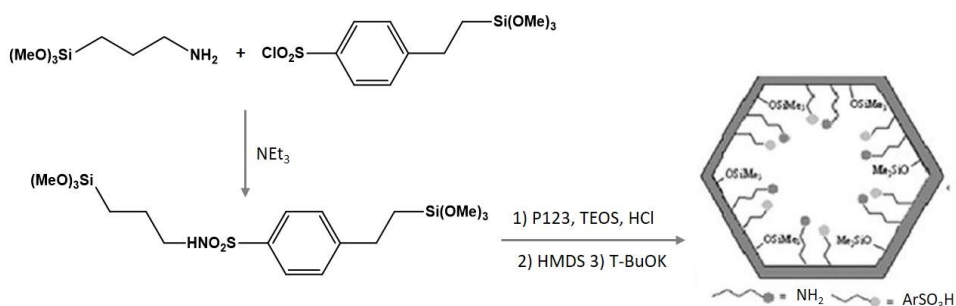
Scheme 2.9. Reaction scheme of a yolk-shell bifunctional silica nanoparticle. The opposite configuration can also be achieved via a similar strategy.¹⁰ BTME = Bis(trimethoxysilyl) ethane, MPTMS = Mercaptopropyl trimethoxysilane.

This changes, however, when we want to use bifunctional materials for cooperative enamine catalysis. In this case, the role of the acid site is to activate the carbonyl functionalities of the reagents for nucleophilic attack by the amine site. Therefore, both functionalities should be in close proximity. The application of acid-base materials in cooperative catalysis is discussed in the following section.

2.2.1.2 Heterogeneous bifunctional (organo)silicas in cooperative enamine catalysis

Several reports were made of $\text{NH}_2/\text{SO}_3\text{H}$ bifunctional materials for cooperative catalysis, synthesized via the grafting or co-condensation of functional silanes. Zeidan et al.¹⁴ reported the synthesis of an SBA-15, with co-condensation of an aminated silane and a benzenesulfonyl chloride-silane. This material was successful as a cooperative catalyst in an aldol reaction. Several groups^{15, 16} used a Boc-protected aminosilane and a mercaptosilane to achieve a $\text{NH}_2/\text{SO}_3\text{H}$ functional material (a method similar as shown in Scheme 2.7 a), with either MCM-41 or SBA-15 structures. All of these materials were shown to be more active in aldol reactions than a physical mixture of acid and base functionalized materials. This confirms that in the case of cooperative catalysis, it is useful to synthesize bifunctional materials. The reported materials were also more active than the aminated material on its own. This proves that the Brønsted acid sites on these materials were able to activate the carbonyl species in proximity to the amine site. There was no indication in these papers that the silanol groups could also act as activating sites. However, loadings of the aminated materials were not reported and perhaps there were not enough free silanol groups left after the incorporation of a high loading of silanes.

Peng et al.¹⁷ used an ingenious method to synthesize a SO₃H/NH₂ functionalized SBA-15, while ensuring that all acid-base pairs were in close proximity. They synthesized a bis-silated benzenesulfonamide, which was incorporated in an SBA-15 structure via co-condensation. Then, a strong base was used to break the sulfonamide bond, which forms dangling benzenesulfonic acid and amine groups in close proximity (Scheme 2.10). They compared the activity of this material in a Knoevenagel reaction to a similar one with randomly distributed functional groups. They also capped the silanol groups on both materials to ensure that the benzenesulfonic acid was the only acid promoting site. They found that the material with acid and basic sites in close proximity was slightly more active than the material with randomly distributed functionalities, proving that both functionalities need to be in close proximity in order to achieve a cooperative effect.



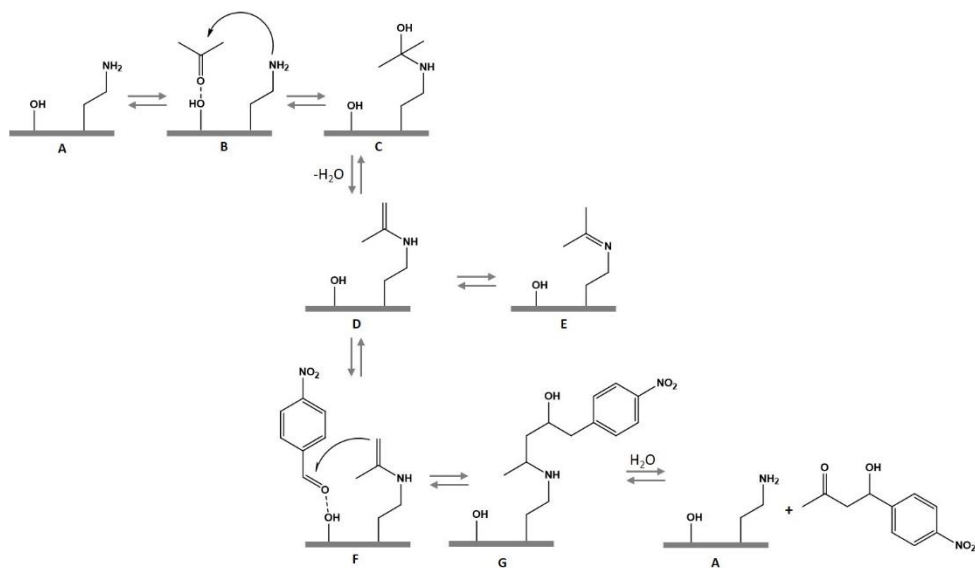
Scheme 2.10. Reaction scheme of a bifunctional silica made with a benzene sulfonamide precursor. Adapted from ref. 15.

2.2.2 Aminated materials with active silanol groups

As opposed to introducing an acid and a base group onto a mesoporous (organo)silica, one can also introduce only an amine and let the surface silanol groups act as the cooperative acid site. Since the average pK_a of silanol groups is close to 7, it is more appropriate to consider the silanol groups as hydrogen-bond donors, rather than as a Brønsted acid.^a They can activate carbonyls for nucleophilic attack via H—bonding, in a similar fashion to Lewis acids. This cooperativity can easily be proven by capping the silanol groups of an aminated (organo)silica with a trimethylsilyl group, using hexamethyl disilazane (HMDS) as reagent. These capped materials are consistently less active in enamine catalysis than their non-capped counterparts.¹⁸⁻²²

Scheme 2.11 shows the reaction mechanism of the aldol reaction of acetone and p-nitrobenzaldehyde, catalyzed by an aminated silica. Structure **A** shows the silica surface

^a In fact, the amine acts as a nucleophile in the enamine mechanism and not as a base. So technically, aminated silicas do not act as cooperative acid-base materials, but as cooperative H-bonding-nucleophile materials. However, the former name is much easier on the tongue and is generally used in the literature.



Scheme 2.11. The reaction mechanism of the aldol reaction of acetone and *p*-nitrobenzaldehyde, catalyzed by an aminated silica.

with an amine functionality and a silanol group in close proximity. The silanol can form a hydrogen bond with acetone, activating it for nucleophilic attack by the amine (**B**). This results in the alcohol form (**C**), which after dehydration yields the enamine (**D**), which is in equilibrium with the imine form (**E**). The enamine **D** is essentially a more activated form of the enol form of acetone, because an enamine is a stronger nucleophile than an enol. The *p*-nitrobenzaldehyde can also be activated by H-bonding with a silanol, followed by nucleophilic attack of the enamine (**F**), which results in structure **G**. After addition of water, the aldol product is released and the amine and silanol groups are available for another catalytic cycle.^{22, 23}

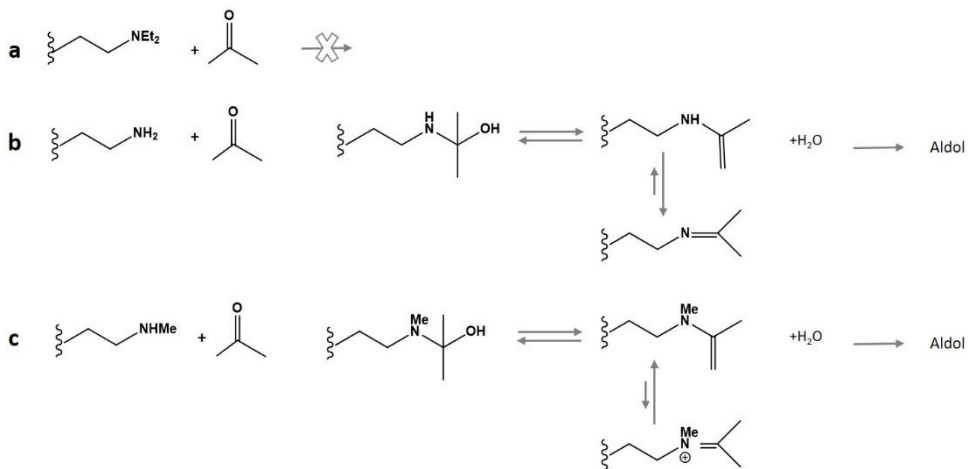
Many reports have been published about this type of material, each one investigating different aspects, such as the influence of the type of base group, as well as the density and distribution of these groups. Their findings are summarized hereafter.

2.2.2.1 Tuning cooperative (organo)silanes by controlling the basic site

Several research groups^{18, 19, 24} investigated the activity of aminated silicas containing primary, secondary and tertiary amines. They found that the activity of the materials increased in the sequence $\text{NEt}_2 < \text{NH}_2 < \text{NHMe}$. In other words, secondary amines are more active than primary amines, while tertiary amines are inactive in enamine catalysis. These reactivities can be elucidated by the enamine reaction mechanism and the differences in enamine formation (Scheme 2.12).

2.10

The mechanism is not applicable with tertiary amines, because they cannot form the enamine intermediate (Scheme 2.12 **a**). For primary amines, an enamine-imine equilibrium is established, in which the imine is thermodynamically favored (**b**). For secondary amines, an enamine-iminium equilibrium is in place, where the enamine is the most stable form (**c**). As the enamine intermediate is necessary for the aldol reaction, and it is most abundant in the case of a secondary amine, this explains why the aldol reaction proceeds the fastest in this case. Another factor to consider is sterical hindrance. Lauwaert et al.¹⁸ found that secondary amines with a bulky substituent drastically decrease in activity.



Scheme 2.12. An overview of the enamine formation reactions for a tertiary amine (**a**), a primary amine (**b**) and a secondary amine (**c**). The vertical arrows show the favoured species in the enamine-imine equilibrium.

Another important factor is the loading and distribution of the basic sites. Sharma et al.²⁵ were able to show the relation between the synthesis method, amine distribution, and catalytic activity of aminated silica materials. They used the grafting of an aminosilane on MCM-41 as synthetic approach. They postulated that, when using an apolar solvent such as toluene during the grafting procedure, the aminosilanes could cluster together, resulting in a material with poor distribution of the amines. In a more polar solvent, the interactions between amines would be less significant, resulting in a more homogeneous distribution of the amines. They used an ingenious method to investigate the distribution of amine functionalities on materials grafted in different solvents. The materials were added to an aqueous Cu^{2+} solution. The materials turned to different colors, depending on the Cu^{2+} ions coordinating to one or two amines. Therefore, this colorimetric method gave an indication of the degree of proximity of the amines on the solid. When the same materials were tested in the catalysis of a Henry reaction (which uses a similar enamine mechanism as the aldol

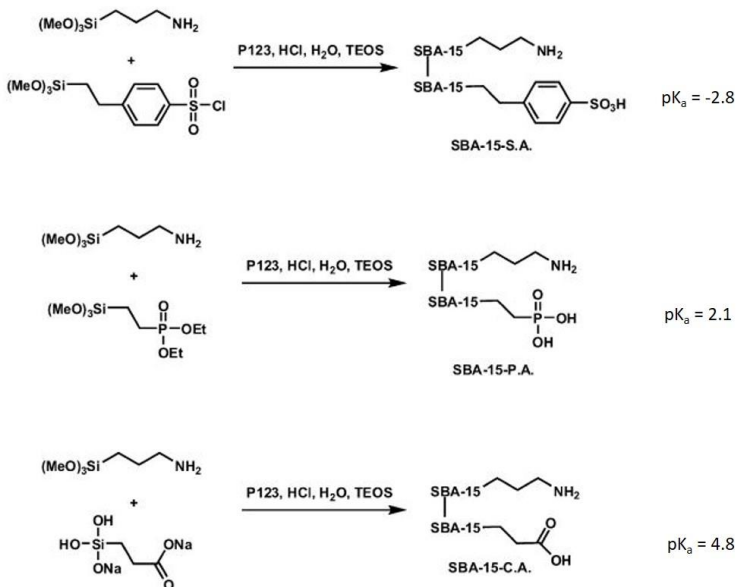
reaction), they found that the materials with a better distribution of amines were more active, presumably because the interaction between silanols and amines was better.

2.2.2.2 Silanol versus acid cooperativity: tuning the acid site

As discussed in the previous sections, two types of cooperative acid-base materials have been reported. Either the acid site is incorporated via a functional silane, or the silanol groups on the silica surface can be used as acid site. Several efforts have been made to investigate the differences between the two strategies and to determine which one is more effective.

Brunelli et al.²⁶ synthesized a mesoporous silica containing an amine and a carboxylic acid functionality. A carboxylic acid silane could not be introduced directly, because it would promote the hydrolysis and condensation of the ethoxysilyl groups and it could interact with the amine. Therefore, they synthesized a silane containing a tert-butyl ester, which can be incorporated into the material and then thermally cleaved to yield the carboxylic acid. The NH₂/COOH material was tested in an aldol reaction and compared to the aminated silica. They found that the silanol groups on the silica surface were a better promoting site than the carboxylic acid groups, which could possibly deactivate the amine via protonation.

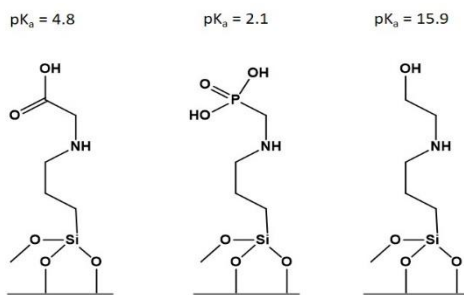
Zeidan et al.²⁷ used a one-pot synthesis method to make acid-base materials (Scheme 2.13). Silanes which can form acids and aminosilanes were co-condensed with TEOS and



Scheme 2.13. Synthetic scheme for acid-base materials, containing different Brønsted acids. The pK_a values of the acids are indicated.²⁴

protonation of the acids yielded the bifunctional materials. When testing acid sites of increasing acid strength (benzenesulfonic, phosphoric and carboxylic acids) in an aldol reaction, they found that the conversion lowered with increasing acid strength. This could be due to protonation of the amine in the presence of strong Brønsted acid sites. Interestingly, they also reported that the selectivity of the reaction towards the aldol product decreased with increasing acid strength. This shows that these acid sites are strong enough to catalyze the dehydration towards the condensation product. In comparison, aminated silicas with silanol promoting groups have selectivities of around 90% towards the aldol product.¹⁹

Lauwaert et al.²⁸ investigated different materials which contained a secondary amine and an acid (or H-bonding) group on the same linker. In this case, a mesoporous silica was grafted with the functional silane containing both functionalities (Scheme 2.14). They limited the loading of the functional sites and prevented clustering during the synthesis to prevent intermolecular interactions between the functional sites, such as acid-base coupling. They were then able to study the influence of different acid sites in proximity to the amine, without protonation of the amine. They found that an alcohol site on the functional linker, acting as H-bond donor, can enhance the aldol reaction just as well as silanol sites can. They also found that a combination of alcohol and silanol sites in proximity



Scheme 2.14. Materials containing acid and base functionalities on the same linker. The pK_a values of the acids are indicated. Based on ref. 25.

of the amine is even more beneficial, because then two carbonyl species can be activated simultaneously. However, the presence of stronger acid sites (carboxylic acid or phosphoric acid) gave lower turnover frequency (TOF) values compared to silanol activation.

These comparative studies show that the presence of a strong Brønsted acid can lower the activity of a material, compared to the presence of silanols. This is possibly due to the protonation, and thus deactivation, of the amine site. A strong acid can also promote the dehydration of the aldol product, which lowers the selectivity of the reaction as well.

In conclusion, the current literature contains many synthesis methods, both for the incorporation of amines and the incorporation of acid and base sites onto mesoporous

silicas. Some properties of the acid and basic sites of functionalized materials could be rationalized in terms of their effect on the catalytic activity of the material. However; most of the current functionalization methods make use of silanes. If we want to extend the incorporation of acid and base sites to PMO materials, we would ideally not use silanes but instead modify the functionality of the PMO linker. Surprisingly, reports of the synthesis of acid-base cooperative catalysts based on PMO materials are very limited. This is the aim of the research presented in the following two chapters.

The studies above also show that when using an acid site other than the silanol groups, it is interesting to put the amine and the acid on the same linker, to avoid deactivation of the amine. This leads us to the investigation of amino acids grafted onto PMO materials for cooperative enamine catalysis. Chapter 3 describes materials formed by grafting cysteine and its derivatives on PMO materials. The use of proline in enamine catalysis is well known and its immobilization on PMO materials is discussed in Chapter 4.

2.3 References

- [1] P.M. Pihko, I. Majander, A. Erkkilä, Enamine Catalysis, *Topics in Current Chemistry*, 291 (2010) 29-75.
- [2] T. Mukaiyama, K. Narasaka, K. Banno, NEW ALDOL TYPE REACTION, *Chemistry Letters*, (1973) 1011-1014.
- [3] H. Bahrmann, H.-D. Hahn, D. Mayer, G.D. Frey, 2-Ethylhexanol, *Ullmann's Encyclopedia of Industrial Chemistry*, 2013.
- [4] D.M. Alonso, J.Q. Bond, J.A. Dumesic, Catalytic conversion of biomass to biofuels, *Green Chemistry*, 12 (2010) 1493-1513.
- [5] B.M. Trost, C.S. Brindle, The direct catalytic asymmetric aldol reaction, *Chemical Society Reviews*, 39 (2010) 1600-1632.
- [6] U. Eder, G. Sauer, R. Weichert, TOTAL SYNTHESIS OF OPTICALLY ACTIVE STEROIDS .6. NEW TYPE OF ASYMMETRIC CYCLIZATION TO OPTICALLY ACTIVE STEROID CD PARTIAL STRUCTURES, *Angewandte Chemie-International Edition*, 10 (1971) 496-&.
- [7] B. List, R.A. Lerner, C.F. Barbas, Proline-catalyzed direct asymmetric aldol reactions, *Journal of the American Chemical Society*, 122 (2000) 2395-2396.
- [8] F.P. Shang, J.R. Sun, H. Liu, C.H. Wang, J.Q. Guan, Q.B. Kan, One-pot cascade reactions catalyzed by acid base mesoporous MCM-41 materials, *Materials Research Bulletin*, 47 (2012) 801-806.
- [9] F.P. Shang, J.R. Sun, S.J. Wu, Y. Yang, Q.B. Kan, J.Q. Guan, Direct synthesis of acid-base bifunctional mesoporous MCM-41 silica and its catalytic reactivity in Deacetalization-Knoevenagel reactions, *Microporous and Mesoporous Materials*, 134 (2010) 44-50.
- [10] M. Sasidharan, S. Fujita, M. Ohashi, Y. Goto, K. Nakashima, S. Inagaki, Novel synthesis of bifunctional catalysts with different microenvironments, *Chemical Communications*, 47 (2011) 10422-10424.
- [11] Y.L. Huang, S. Xu, V.S.Y. Lin, Bifunctionalized Mesoporous Materials with Site-Separated Bronsted Acids and Bases: Catalyst for a Two-Step Reaction Sequence, *Angewandte Chemie-International Edition*, 50 (2011) 661-664.
- [12] Y. Yang, X. Liu, X.B. Li, J. Zhao, S.Y. Bai, J. Liu, Q.H. Yang, A Yolk-Shell Nanoreactor with a Basic Core and an Acidic Shell for Cascade Reactions, *Angewandte Chemie-International Edition*, 51 (2012) 9164-9168.

[13] P. Li, C.Y. Cao, Z. Chen, H. Liu, Y. Yu, W.G. Song, Core-shell structured mesoporous silica as acid-base bifunctional catalyst with designated diffusion path for cascade reaction sequences, *Chemical Communications*, 48 (2012) 10541-10543.

[14] R.K. Zeidan, S.J. Hwang, M.E. Davis, Multifunctional heterogeneous catalysts: SBA-15-containing primary amines and sulfonic acids, *Angewandte Chemie-International Edition*, 45 (2006) 6332-6335.

[15] X.F. Yu, Y.C. Zou, S.J. Wu, H. Liu, J.Q. Guan, Q.B. Kan, Synthesis of acid-base bifunctional mesoporous materials by oxidation and thermolysis, *Materials Research Bulletin*, 46 (2011) 951-957.

[16] Y.Q. Shao, H. Liu, X.F. Yu, J.Q. Guan, Q.B. Kan, Synthesis, characterization and catalytic activity of acid-base bifunctional materials through protection of amino groups, *Materials Research Bulletin*, 47 (2012) 768-773.

[17] Y. Peng, J.Y. Wang, J. Long, G.H. Liu, Controllable acid-base bifunctionalized mesoporous silica: Highly efficient catalyst for solvent-free Knoevenagel condensation reaction, *Catalysis Communications*, 15 (2011) 10-14.

[18] J. Lauwaert, E. De Canck, D. Esquivel, P. Van Der Voort, J.W. Thybaut, G.B. Marin, Effects of amine structure and base strength on acid-base cooperative aldol condensation, *Catalysis Today*, 246 (2015) 35-45.

[19] Y.W. Xie, K.K. Sharma, A. Anan, G. Wang, A.V. Biradar, T. Asefa, Efficient solid-base catalysts for aldol reaction by optimizing the density and type of organoamine groups on nanoporous silica, *Journal of Catalysis*, 265 (2009) 131-140.

[20] S.L. Hruby, B.H. Shanks, Acid-base cooperativity in condensation reactions with functionalized mesoporous silica catalysts, *Journal of Catalysis*, 263 (2009) 181-188.

[21] N.A. Brunelli, S.A. Didas, K. Venkatasubbaiah, C.W. Jones, Tuning Cooperativity by Controlling the Linker Length of Silica-Supported Amines in Catalysis and CO₂ Capture, *Journal of the American Chemical Society*, 134 (2012) 13950-13953.

[22] J. Lauwaert, E. De Canck, D. Esquivel, J.W. Thybaut, P. Van Der Voort, G.B. Marin, Silanol-Assisted Aldol Condensation on Aminated Silica: Understanding the Arrangement of Functional Groups, *Chemcatchem*, 6 (2014) 255-264.

[23] K.C. Kim, E.G. Moschetta, C.W. Jones, S.S. Jang, Molecular Dynamics Simulations of Aldol Condensation Catalyzed by Alkylamine-Functionalized Crystalline Silica Surfaces, *Journal of the American Chemical Society*, 138 (2016) 7664-7672.

[24] S. Shylesh, D. Hanna, J. Gomes, S. Krishna, C.G. Canlas, M. Head-Gordon, A.T. Bell, Tailoring the Cooperative Acid-Base Effects in Silica-Supported Amine Catalysts:

Applications in the Continuous Gas-Phase Self-Condensation of n-Butanal, *Chemcatchem*, 6 (2014) 1283-1290.

[25] K.K. Sharma, A. Anan, R.P. Buckley, W. Ouellette, T. Asefa, Toward efficient nanoporous catalysts: Controlling site-isolation and concentration of grafted catalytic sites on nanoporous materials with solvents and colorimetric elucidation of their site-isolation, *Journal of the American Chemical Society*, 130 (2008) 218-228.

[26] N.A. Brunelli, K. Venkatasubbaiah, C.W. Jones, Cooperative Catalysis with Acid-Base Bifunctional Mesoporous Silica: Impact of Grafting and Co-condensation Synthesis Methods on Material Structure and Catalytic Properties, *Chemistry of Materials*, 24 (2012) 2433-2442.

[27] R.K. Zeidan, M.E. Davis, The effect of acid-base pairing on catalysis: An efficient acid-base functionalized catalyst for aldol condensation, *Journal of Catalysis*, 247 (2007) 379-382.

[28] J. Lauwaert, E.G. Moschetta, P. Van Der Voort, J.W. Thybaut, C.W. Jones, G.B. Marin, Spatial arrangement and acid strength effects on acid-base cooperatively catalyzed aldol condensation on aminosilica materials, *Journal of Catalysis*, 325 (2015) 19-25.

Chapter 3.

PMOs functionalized with cysteine and cysteamine for cooperative enamine catalysis

3.1 Set-up and aim of the research

In this chapter, a new synthetic route is proposed to obtain cooperative acid-base catalysts based on PMO materials. We take advantage of the ethylene functionalities embedded in a PMO material to incorporate carboxylic acid and amine groups via a single thiol-ene click reaction, using the amino acid cysteine. A similar approach is employed for the incorporation of a sole amine functionality, by grafting of cysteamine. As a result, the catalytically active sites are not linked to the carrier material via siloxane bonds, as is the case when classical grafting or co-condensation procedures are used, such as described in Chapter 2, but via more hydrolytically stable thioether bonds. In this way, the thiol-ene click reaction provides a reliable procedure for a straightforward, single-step grafting method.

The catalytic activity of the functionalized PMO materials is investigated in the aldol reaction of 4-nitrobenzaldehyde and acetone. The acid promoting properties of the carboxylic acid groups are compared to those of the silanol groups which are intrinsically present on the PMO surface. Subsequently, the influence of the loading of the catalytic functionality is investigated, as well as the potential to induce chirality in the reaction products. This part of the chapter was published under the following reference: J. Ouwehand, J. Lauwaert, D. Esquivel, K. Hendrickx, V. Van Speybroeck, J.W. Thybaut, P. Van Der Voort, Facile Synthesis of Cooperative Acid–Base Catalysts by Clicking Cysteine and

Cysteamine on an Ethylene-Bridged Periodic Mesoporous Organosilica, *Eur. J. Inorg. Chem.* 2016, 2144–2151.^a

This functionalization method was then also attempted on a monoallyl ring PMO (mAR-PMO), but the resulting materials showed much lower catalytic activity than the functionalized ethene PMO. Several properties of the two PMO materials were compared to explain this difference in activity.

3.2 Synthesis and characterization of the materials

An ethene PMO (ePMO) was prepared via the procedure described in Chapter 1 (see Scheme 1.4). The 100% trans ethene precursor was synthesized by the metathesis reaction of vinyltriethoxysilane and purified by vacuum distillation. The ¹H NMR spectrum of the ePMO precursor is shown in Figure 3.1.^b The absence of any signals between 5 and 6 ppm shows that the vinyltriethoxysilane was completely removed. For the ePMO synthesis, the

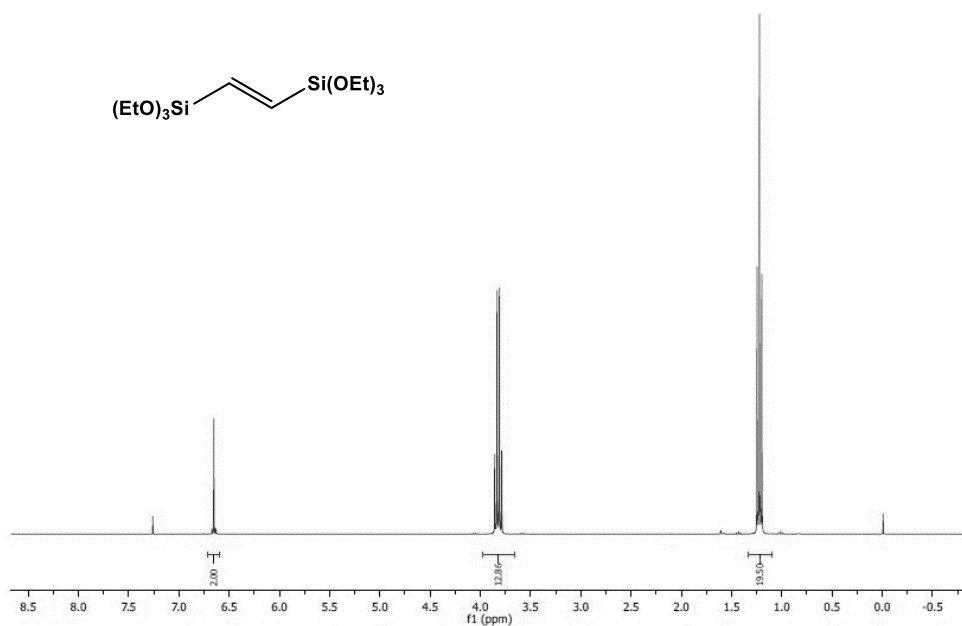
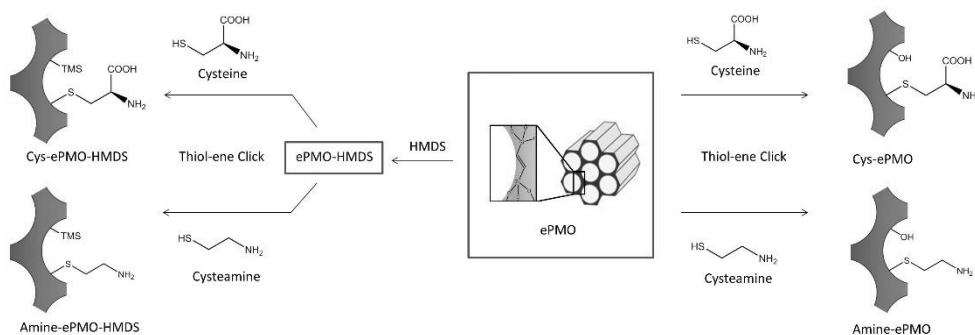


Figure 3.1. ¹H NMR spectrum of the 100% trans ePMO precursor, measured in CDCl₃.

^a The author performed all material syntheses and characterizations. The computational study was performed by Kevin Hendrickx. Catalytic testing and analysis were performed in part by Jeroen Lauwaert and in part by the author. Chiral analysis was performed by Jan Goeman.

^b ¹H NMR (300 MHz, CDCl₃) δ=6.65 (s, 2H, CH=CH), 3.83 (q, *J* = 7.0 Hz, 12H, OCH₂CH₃), 1.22 (t, *J* = 7.0 Hz, 18H, OCH₂CH₃)

100% trans ethene precursor was added to an aqueous solution of P123, HCl and butanol. After a stirring step at 45°C and an aging step at 90°C, the solid was filtered off and the P123 template was removed via Soxhlet extraction with acetone. The ethene functionality in the PMO was then used as an anchoring point for cysteine and cysteamine. The thiol-ene click reactions with these two compounds were performed in degassed water in a UV reactor, using Irgacure 2959 as the radical initiator. The reaction times of the click reactions were varied in order to obtain materials with different amine and amino acid loadings. A similar reaction was repeated on ePMO materials with deactivated silanol groups. These materials were treated with hexamethyldisilazane (HMDS) prior to the click-functionalization, to cap the silanols. These procedures resulted in four different types of PMO catalysts (Scheme 3.1).



Scheme 3.1. An overview of the four types of catalyst obtained by functionalizing the ePMO. (TMS = trimethylsilane)

We can now investigate materials containing a primary amine and different acid promoting sites, namely a material containing amines combined with silanol groups (Amine-ePMO), carboxylic acids (Cys-ePMO-HMDS), or a combination of both (Cys-ePMO) and a material without acid promoting sites (Amine-ePMO-HMDS).

The structure and functionalities of the PMO materials were analyzed by diffuse reflectance infrared Fourier transform spectroscopy (DRIFTS), nitrogen sorption, X-ray diffraction (XRD) and CHN elemental analysis.

The presence of the functional groups was confirmed by DRIFTS measurements. As shown in Figure 3.2, all non-capped samples show characteristic silanol bands around 3720 cm^{-1} . For ePMO-HMDS, the silanol band is strongly reduced, indicating that the majority of free silanols have been capped with HMDS. The bands at 2950 cm^{-1} represent C-H stretch from the ethylene bridge and the carbons in the cysteine or cysteamine groups. The increased C-H signal at 2950 cm^{-1} for the capped sample is due to the presence of the trimethylsilyl groups originating from HMDS. In the Cys-ePMO spectrum, a carbonyl signal can be

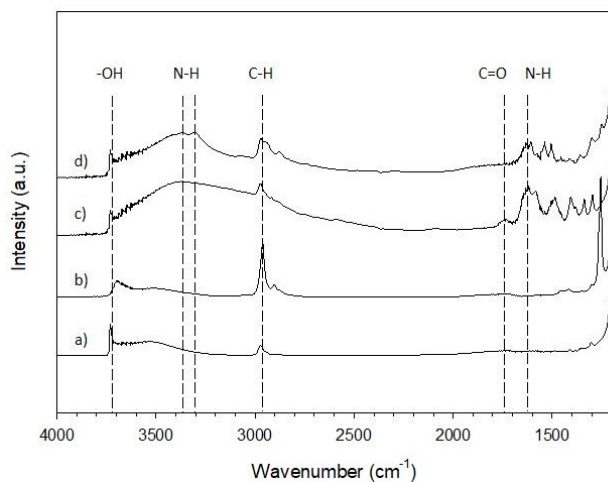


Figure 3.2. DRIFTS spectra of the materials. a) ePMO, b) ePMO-HMDS, c) Cys-ePMO, d) Amine-ePMO.

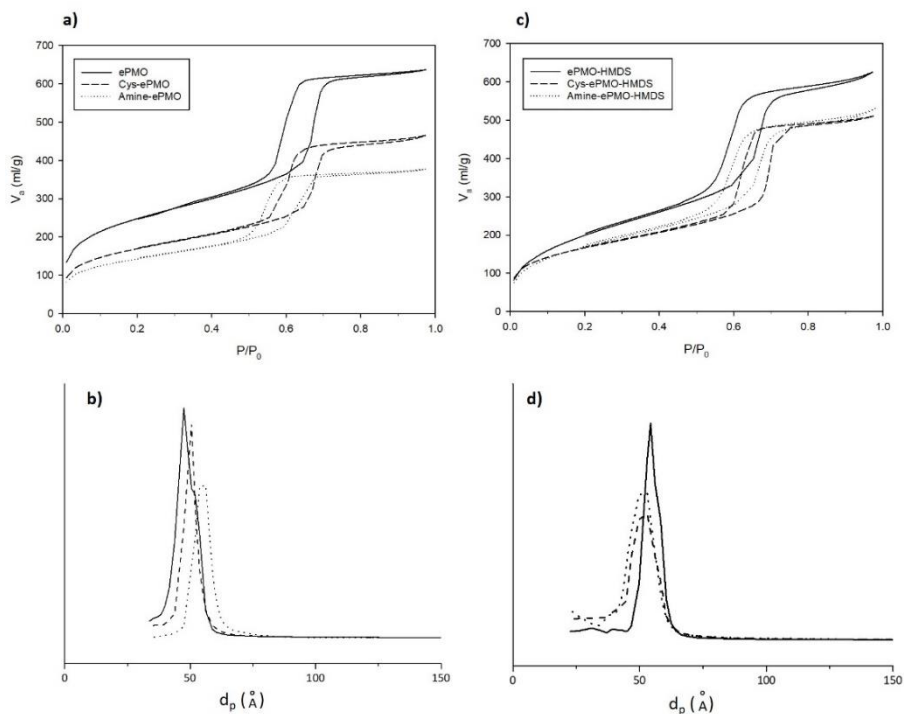


Figure 3.3. Nitrogen sorption isotherms (top) and BJH pore size distributions (bottom) of the non-capped (a and b) and capped (c and d) samples. BJH distribution was based on the desorption branch of the isotherm.

observed at 1730 cm^{-1} . In the Amine-ePMO spectrum, two bands at 3315 and 3365 cm^{-1} can be assigned to N-H stretching. In the Cys-ePMO and Amine-ePMO spectra, the signal at 1615 cm^{-1} is due to N-H bending.

The nitrogen sorption isotherms and BJH pore size distributions of the materials are shown in Figure 3.3. All materials exhibit type IV isotherms and H1-type hysteresis loops at relative pressures in the range of 0.5 to 0.7, indicative of mesopores with a narrow pore size distribution. The BJH pore size distributions confirm this, showing a narrow peak between 5 and 6 nm for all materials.

The specific BET surface area (S_{BET}), average pore size (d_p), pore volume (V_p) and wall thickness of the materials are summarized in Table 3.1. The starting ePMO and ePMO-HMDS materials have high surface areas of 890 and 751 m^2/g , respectively. After functionalization with cysteine and cysteamine, the specific surface area of the samples decreases, which could be due to an effective decrease in surface area, as well as to an increase in weight after the grafting procedure. All samples have a pore diameter around 5 nm and a wall thickness between 4 and 6 nm. This high wall thickness provides stability to the PMO materials.

Table 3.1. Structural properties and functional group loadings of the PMO materials.

Sample	S_{BET}^a (m^2/g)	d_p^b (nm)	V_p^c (ml/g)	a_0^d (nm)	Wall thickness ^e (nm)	Loading ^f (mmol/g)
ePMO	890	5.4	0.98	9.4	4.2	-
ePMO-HMDS	751	5.4	0.95	10.6	5.2	-
Cys-ePMO-1	610	5.4	0.71	10.2	4.8	0.08
Cys-ePMO-2	576	5.5	0.76	10.2	4.7	0.41
Cys-ePMO-3	496	5.0	0.44	10.6	5.6	0.84
Cys-ePMO-HMDS	604	5.0	0.78	9.8	4.8	0.15
Amine-ePMO-1	518	4.8	0.58	9.1	4.3	0.49
Amine-ePMO-2	373	5.5	0.60	10.1	4.6	0.65
Amine-ePMO- HMDS	633	5.3	0.80	10.8	5.5	0.46

^aSpecific BET surface area ^bBJH pore diameter, determined from desorption isotherm ^cPore volume, determined from desorption isotherm at $P/P_0=0.95$ ^dLattice parameter, calculated via $a_0=2d_{100}/\sqrt{3}$ ^eCalculated as the difference between a_0 and d_p ^fLoading of nitrogen, from CHN elemental analysis

The XRD patterns of the materials before and after grafting of cysteine and cysteamine are shown in Figure 3.4. All the materials show the characteristic (100), (110) and (200) reflections of a hexagonal pore ordering, which confirms that after functionalization, all samples retain their ordered pore structure of the P6mm space group.

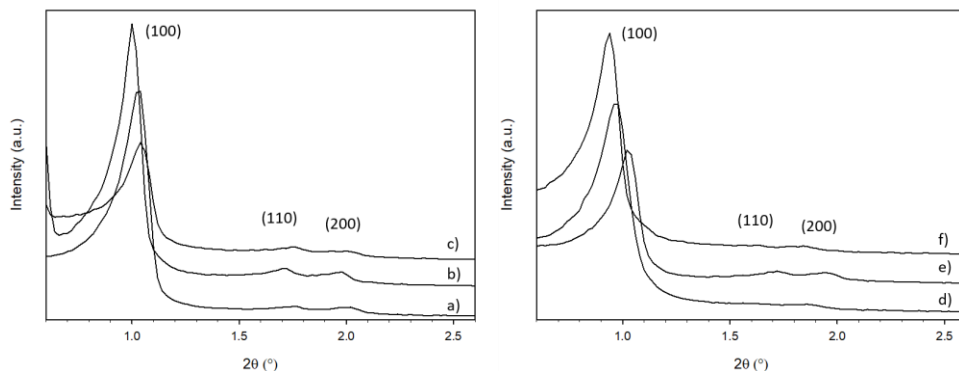


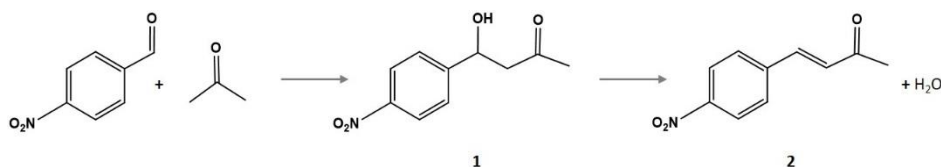
Figure 3.4 XRD patterns of the non-capped (left) and capped (right) samples. a) ePMO, b) Cys-ePMO, c) Amine-ePMO, d) ePMO-HMDS, e) Cys-ePMO-HMDS, f) Amine-ePMO-HMDS.

After grafting of cysteine and cysteamine, the loading of the functional groups was determined by elemental analysis of nitrogen (Table 3.1). For Cys-ePMO and Amine-ePMO, catalysts of different loadings were obtained by varying the reaction time of the thiol-ene click reaction. The loadings of the catalysts range from 0.08 to 0.84 mmol/g of nitrogen.

3.3 Catalytic Results

3.3.1 Activity and Selectivity

The catalytic activities of the functionalized materials were tested in the aldol reaction of 4-nitrobenzaldehyde and acetone (Scheme 3.2). In each experiment, the amount of catalyst added to the reaction mixture was adjusted such that the desired amount of amines was present, namely 4 mol-% with respect to the 4-nitrobenzaldehyde concentration. This way we are able to directly compare the activity of the different materials to each other.



Scheme 3.2. The aldol condensation of 4-nitrobenzaldehyde and acetone, with the formation of the aldol product (1) and the condensation product (2).

The reaction shown in Scheme 3.2 is a common aldol test reaction. It makes use of a symmetrical ketone as the nucleophile and a non-enolizable aldehyde as the electrophile.

3.6

This ensures that only one aldol product can be formed. Additionally, 4-nitrobenzaldehyde is an activated aldehyde, due to the electron withdrawing effect of the nitro group.¹

The catalytic data of the catalysts are represented in Table 3.2. The catalytic activity of each sample is expressed using the turnover frequency (TOF). The TOF expresses the amount of conversions performed per catalytic site per second and it is determined at the beginning of the conversion curve. The blank reaction, performed without addition of any catalyst did not yield any product after 24 hours. For the catalyzed reactions, conversion increased linearly with the reaction time up to a conversion of approximately 95%, indicating that the reaction rate remains constant and that the materials are stable during the catalytic tests. All catalysts could promote the reaction with a high selectivity towards aldol product **1** (>90%), with TOF values ranging from 3.0×10^{-5} to $5.5 \times 10^{-4} \text{ s}^{-1}$.

Table 3.2. Catalytic data of the functionalized PMO materials.

Sample	Loading ^a (mmol/g)	TOF·10 ⁻⁴ (s ⁻¹)	Selectivity ^b (%)	ee ^c (%)
Blank	0	0	-	-
Cys-ePMO-1	0.08	5.5	92.6	<5
Cys-ePMO-2	0.41	2.5	95.0	<5
Cys-ePMO-3	0.84	1.1	96.8	<5
Cys-ePMO-HMDS	0.15	0.9	95.3	25 (±5)
Amine-ePMO-1	0.49	3.5	96.5	<5
Amine-ePMO-2	0.65	2.3	96.5	<5
Amine-ePMO-HMDS	0.46	0.3	91.2	<5

^a Loading of nitrogen, from elemental analysis. ^b Towards aldol product **1**. ^c Towards the (*R*)-isomer of **1**.

The TOF values in Table 3.2 can be compared to activities of aminated porous silica materials previously reported by Lauwaert et al.², as these were tested in the same aldol reaction at identical reaction conditions. Porous silica grafted with a primary amine showed a TOF of $7.8 \cdot 10^{-4} \text{ s}^{-1}$, which is somewhat higher than the Amine-ePMO samples. A bifunctional silica material grafted with both amine and carboxylic acid groups showed a TOF of $9.5 \cdot 10^{-5} \text{ s}^{-1}$, which is slightly lower than the Cys-ePMO samples. Overall, the catalytic activities of the PMO material reported here are in the same order of magnitude as the corresponding silica materials. The chirality of the aldol product was investigated by chiral HPLC. The only sample which showed significant enantiomeric excess (ee) was Cys-ePMO-HMDS. These catalytic data are interpreted in the following sections.

3.3.2 Influence of the acid promoting site

In order to compare the four types of materials we obtained (see Scheme 3.1), while minimizing the influence of the loading of the active sites, four different samples with similar amine loadings (in the range of 0.15 to 0.5 mmol/g) were selected. These samples and their TOF values are represented in Figure 3.5. As could be expected, Amine-ePMO-HMDS, without any acid promoting sites, has the lowest activity. Amine-ePMO, which contains only silanol promoting groups, is more active than Cys-ePMO-HMDS, which contains only carboxylic acid promoting groups. This suggests that, for this reaction, the surface silanol groups on the PMO surface are more efficient promoters to the amine group. This is also immediately apparent from the fact that both capped samples have lower activities than the non-capped samples.

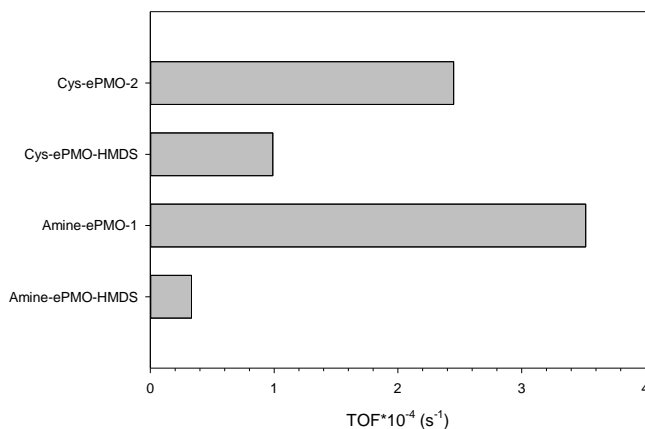


Figure 3.5. Catalytic activity (TOF) of the different types of catalysts.

This observation is in agreement with previously published studies regarding functionalized porous silica materials^{2, 3}. In the enamine reaction mechanism, the role of the acid promoting sites is to activate the carbonyl species. However, it was observed that the grafting of carboxylic acid groups along with amine groups on the silica surface lowered the activity of the materials compared to silicas functionalized with only amines. This effect was ascribed to two factors in the literature.

Firstly, it was stipulated that the grafting procedure of the carboxylic acid group via silylation of the surface silanols, effectively deactivates a fraction of the active silanols. However, this theory is not applicable to the PMO materials described here, since both functional groups were incorporated via thiol-ene click chemistry as opposed to silylation.

The second explanation for the decrease in activity is related to the relatively high acid strength of the carboxylic acid (pKa of 5) compared to the silanol groups (average pKa of 7.1⁴). This makes the carboxylic acid group a stronger acid and thus more likely to neutralize the amine. This second effect can also take place on the PMO material, with the difference that only H-bonds between different cysteine moieties can occur, as the amine and carboxylic acid on a single cysteine moiety are not in a configuration which allows H-bonding. The degree of H-bond formation and thus the loss of catalytic activity should then be proportional to the loading of the active sites. This effect is investigated in the following section.

The activity of Cys-ePMO, which contains both carboxylic acid and silanol groups, is lower than that of Amine-ePMO. This leads to the reasoning that a third factor should be considered, in the form of a steric hindrance effect, caused by the fact that the carboxylic acid groups are in close proximity to the amine active sites. This could make the amines less accessible to the aldol reagents, or it could hinder the amine being activated by the silanol groups, which would result in a decrease in activity of Cys-ePMO compared to Amine-ePMO. Thus, for the PMO materials, a combination of H-bond formation and steric hindrance can explain the difference in reactivity of the catalysts.

In terms of chirality of the aldol product, Cys-ePMO-HMDS is the only sample to show a significant enantioselectivity, with 25% ee. The Cys-ePMO sample does not show any significant ee. This indicates that for this sample, the silanol groups are the main activating groups, but they are less accessible due to the presence of the COOH group. This would explain that the activity lowered for Cys-ePMO as compared to Amine-ePMO, but no significant ee was observed.

In conclusion, the aminated ePMO with only silanol promoters has the highest activity in the aldol condensation reaction, due to a stronger promotion by the silanol groups. This also results in a lack of enantioselectivity in all samples except Cys-ePMO-HMDS.

3.3.3 Influence of the loading

In a further investigation of the catalytic properties of the materials, the influence of the loading of the active sites is studied. For this, the Cys-ePMO and Amine-ePMO samples with different loadings are compared. The TOF values are represented in Figure 3.6. For each material, the amount of catalyst used was adjusted, based on the amine loadings, so that the ratio of amines to 4-nitrobenzaldehyde stayed the same. Therefore, the materials with different loadings can be compared directly. For both the cysteine and amine functionalized samples, the TOF increases with decreasing loading. A similar effect was reported in the literature when grafting primary amines on silica materials with different loadings.⁵⁻⁷ The loss of activity at higher loadings was ascribed to a decrease in surrounding silanol groups.

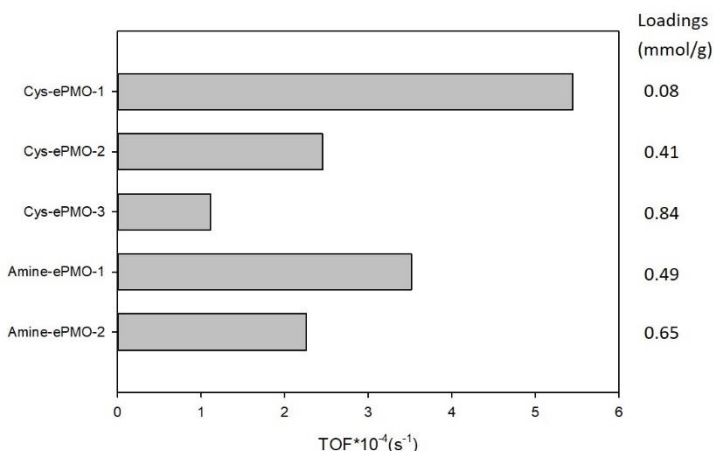


Figure 3.6. TOFs of the samples with different loadings.

Furthermore, it was suggested that hydrogen bonds are formed between the functional groups involved, causing deactivation of the amine active sites.

In order to investigate the hydrogen bond formation on a PMO material, a computational study, based on a simplified model system was performed to obtain more insight into the interactions at the nanoscale level. Theoretical studies of PMO materials are only very limitedly available in literature⁸, whilst modeling of mesoporous silicas is already more common.⁹ To investigate the possible conformations of two cysteine moieties grafted on neighboring ethylene bridges, a simple computational model was used, where the PMO backbone is kept rigid, whereas the cysteine moieties are allowed to rotate and interact. Optimizations starting from different initial geometries showed that the potential energy surface of the system has several local minima. All localized minima are shown in Figure 3.7. The relative stabilities of the four structures, expressed in relative Gibbs free energy values, are shown in Table 3.3. Structure C has the lowest Gibbs free energy and is therefore most stable. This structure contains two hydrogen bonds between the COOH and NH₂ moieties. Structure D also contains two H-bonds, but is twisted towards the siloxane bridge, causing an increase of 16 kJ/mol compared to structure C. Structures A and B are only stabilized by a single H-bond and their energies are around 25 kJ/mol higher than structure C.

The stable conformations presented in Figure 3.7 were then introduced in a model where the silanol groups and ethylene bridges are no longer static, but also allowed to rotate and interact with the cysteine moieties. This resulted in two stable conformations, presented in Figure 3.8. The energetic values for these structures are represented in Table 3.3. Both structures are more stable than structure C. Structure F is the most stable conformation. It

is stabilized by H-bonds between the amine groups, between the carboxylic acid groups and between the amine and the silanol groups.

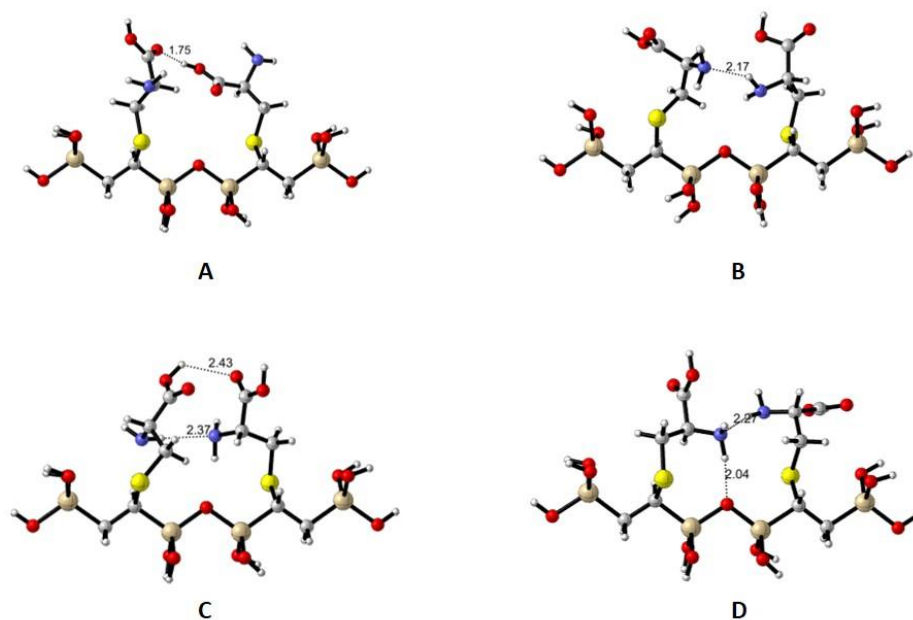


Figure 3.7. The four structures (A, B, C and D) corresponding to local minima of the potential energy surface of a rigid PMO backbone containing two neighboring cysteine units. (H=white, C=gray, N=blue, O=red, Si=beige, S=yellow)

Table 3.3. Energy differences between structures A, B, C and D. Δ is the difference, expressed in kJ/mol, between the Gibbs free energy of the respective structure and the most stable structure C. Energy values for the further optimized structures E and F are also shown.

	Δ (kJ/mol)
Structure A	+24
Structure B	+26
Structure C	0
Structure D	+16
Structure E	-21
Structure F	-45

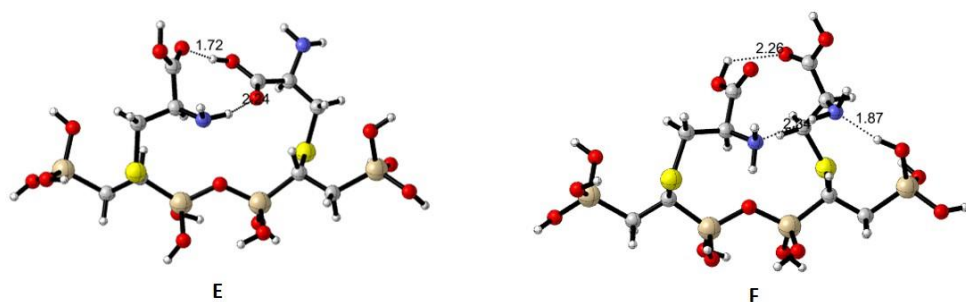


Figure 3.8. Optimization fixing only Si atoms (ethylene bridge and silanol groups optimized) starting from structure A and C respectively results in structures E and F. (H=white, C=gray, N=blue, O=red, Si=beige, S=yellow)

In order to confirm the geometries obtained from these static calculations, first principle molecular dynamics simulations were performed. Within the time scale of the simulation (12 ps), the molecule remained mostly in this stable conformation, showing the strong effect of the amine H-bonds. Figure 3.9 shows the $N\cdots H$ distance during the simulation. It can be observed that the bond length stays within the range of a strong hydrogen bond¹⁰, confirming that this geometry is stable when allowed to rotate freely. In conclusion, the calculations confirm a large stabilizing effect due to H-bond formation between two neighboring amine groups. Figure 3.10 shows a similar model, this time of an isolated cysteine moiety grafted on the PMO backbone, representing the materials with lower

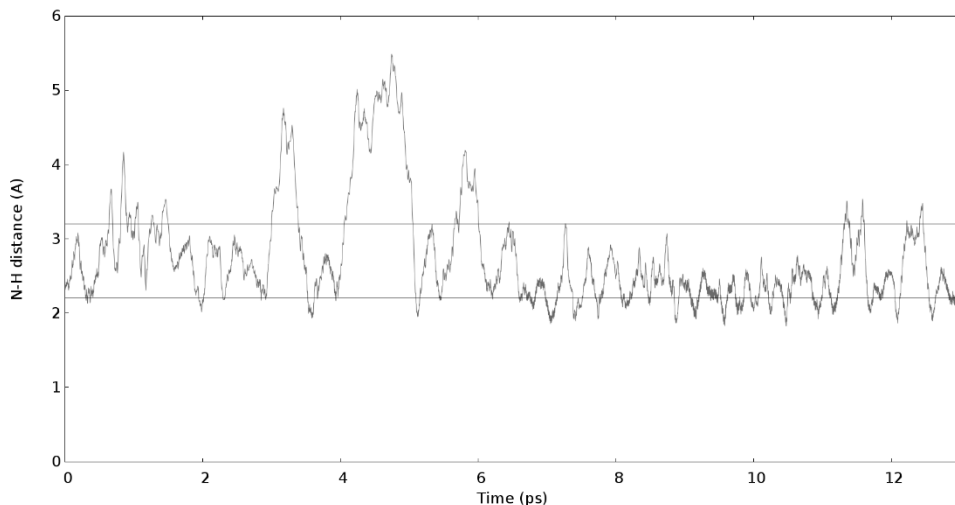


Figure 3.9. Evolution of the $N\cdots H$ hydrogen-bond length during the molecular dynamics simulation. The black lines represent the interval in which the interaction is labeled as a strong hydrogen bond.

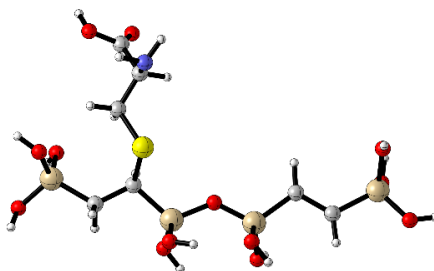


Figure 3.10. Geometric model of an isolated cysteine group grafted on the PMO backbone. (H=white, C=gray, N=blue, O=red, Si=beige, S=yellow)

loadings. In this model, the silanol groups were again allowed to rotate and interact with the cysteine group. However, in this case, no hydrogen bonding is observed.

In conclusion, this computational study shows that the configuration of two neighboring cysteine moieties is strongly stabilized by the formation of H-bonds. In this case, the active amine site could be strongly inhibited in the catalytic reaction, by the change in conformation as well as by the formed H-bonds. On the contrary, an isolated cysteine moiety is not hampered by H-bonding. These findings are in accordance with the catalytic results. At high loadings, the chance of finding two neighboring cysteine sites increases. The samples with higher loadings show a decrease of activity, which can be ascribed to the effects found in the computational study. The samples with the lowest loadings have the highest activities, which is in accordance with the model of the isolated cysteine site, which is more likely to occur at these lower loadings. The Amine-ePMO samples show a similar trend in catalytic activity, which leads to believe that a similar reasoning is valid for these aminated samples.

3.4 Extension of the methodology to the monoallyl ring PMO

After successfully functionalizing the ePMO via thiol-ene click chemistry, it was a logical step to extend this methodology to the monoallyl ring PMO. In fact, the allyl functionality should be more reactive than the ethene functionality in the thiol-ene click reaction, because it is less substituted. Additionally, the dangling allyl groups stick out into the pores and should therefore be more accessible. The following sections discuss the thiol-ene click functionalization of the mAR-PMO and its catalytic results.

3.4.1 Synthesis and characterization of a functionalized monoallyl ring PMO

A monoallyl ring PMO was prepared via the method described in Chapter 1. The commercial ring precursor was allylated and the monoallylated product was isolated by column separation. The proton NMR spectrum of the isolated precursor is shown in

Figure 3.11.^c The PMO was formed by adding the precursor to a solution of HCl, KCl and the P123 template. The solution is stirred at 45°C for 3 hours, followed by a 24 hour aging step at 95°C. The PMO was then filtered off and the template was removed by a Soxhlet extraction with acetone.

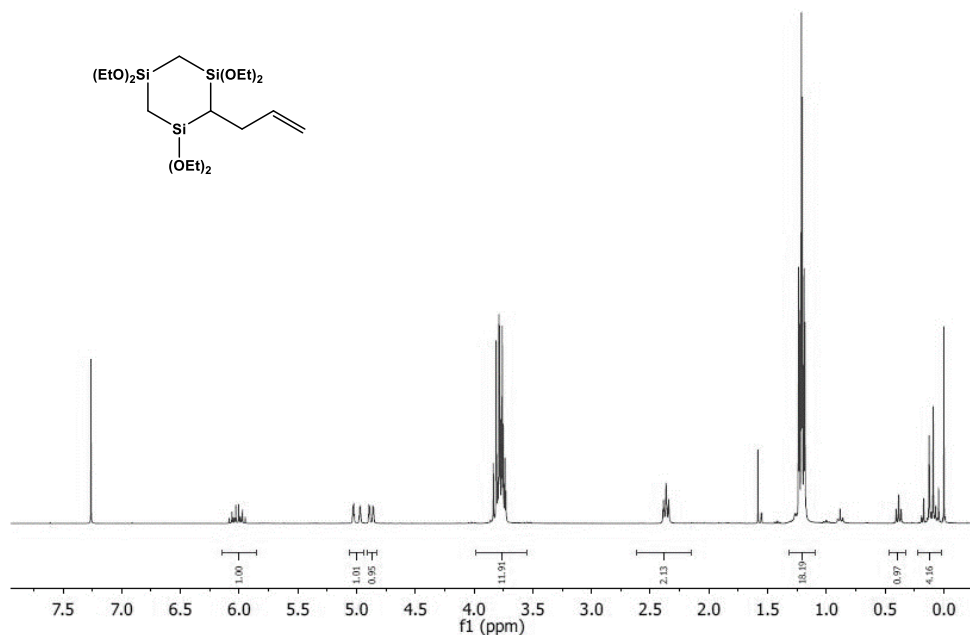


Figure 3.11. ¹H NMR spectrum of the monoallyl ring precursor, measured in CDCl₃.

The nitrogen sorption isotherm, BJH pore size distribution and XRD diffractogram are shown in Figure 3.13. The mAR-PMO has a BET surface area of 766 m²/g, with a well-defined pore size of 5.5 nm and a pore volume of 0.97 ml/g. It has a very similar mesopore structure to the ePMO, because both materials were synthesized using the P123 template.

The monoallyl ring PMO was then functionalized with cysteine and cysteamine. The thiol-ene click reaction proceeded within an hour, and the loading was controlled by adjusting the amount of cysteine or cysteamine added to the reaction mixture. This resulted in the

^c ¹H NMR (300 MHz, CDCl₃) δ = 6.02 (ddt, *J* = 17.0, 9.9, 7.0 Hz, 1H, CH₂CH=CH₂), 5.00 (m, 1H, CH=CH₂), 4.88 (m, 1H, CH=CH₂), 3.76 (m, 12H, OCH₂CH₃), 2.36 (m, 2H, CHCH₂CH=CH₂), 1.22 (m, 18H, OCH₂CH₃), 0.38 (t, *J* = 6.4, 1H, CH(Si)₂CH₂), 0.11 (m, 4H, CH₂(Si)₂), 1.56 (s, trace water)

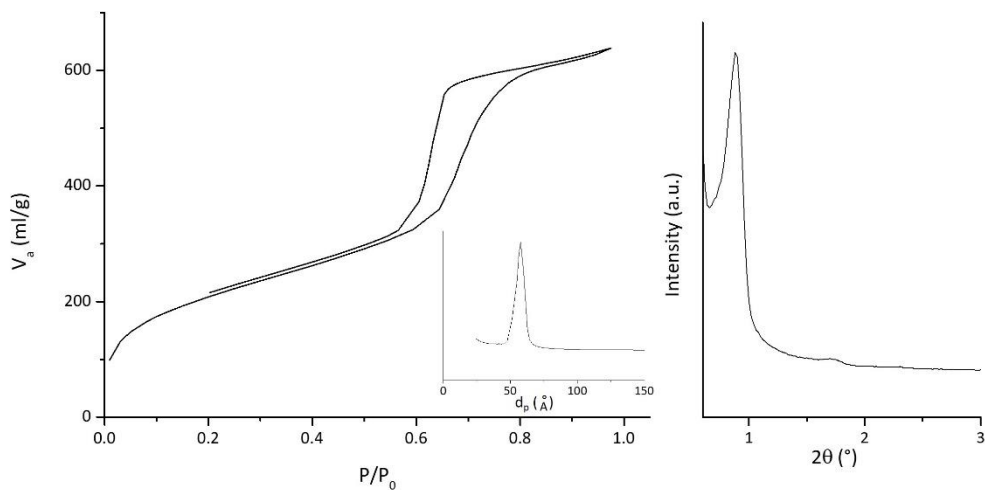


Figure 3.12. Nitrogen sorption isotherm with BJH distribution in inset (left) and XRD diffractogram (right) of the monoallyl ring PMO.

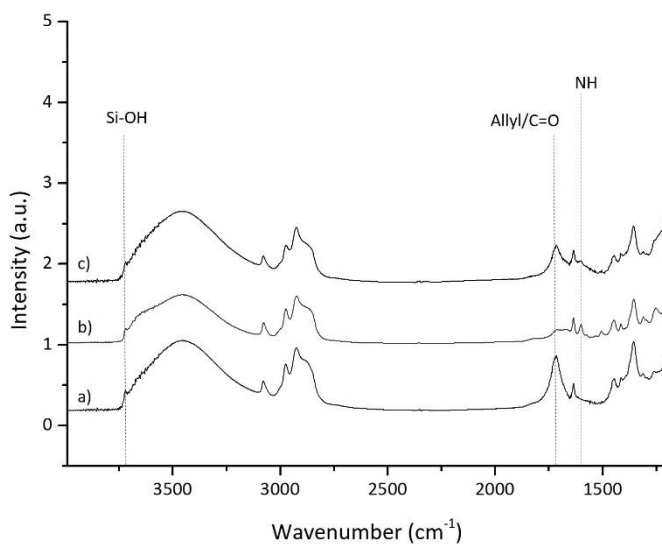


Figure 3.13. DRIFTS spectra of the mAR-PMO (a), Amine-mAR-PMO (b) and Cys-mAR-PMO (c).

materials Cys-AllylPMO and Amine-AllylPMO. The DRIFTS spectra of the mAR-PMO before and after functionalization are shown in Figure 3.12. A silanol signal can be observed for all samples at 3730 cm^{-1} , as well as a broad water band between 3730 and 3140 cm^{-1} . All spectra contain CH signals between 3100 and 2700 cm^{-1} . The broad band visible at 1730 cm^{-1} can tentatively be assigned to the allyl functionality for mAR-PMO and to the carbonyl

group for Cys-mAR-PMO. The amine functionality is present at 1620 cm^{-1} on Amine-mAR-PMO and Cys-mAR-PMO. Further bands at 1450 cm^{-1} and below belong to CH bonds.

3.4.2 Catalytic results and comparisons between the PMOs

The functionalized monoallyl ring PMO materials were tested in the aldol reaction of acetone and 4-nitrobenzaldehyde, under identical conditions as used for the functionalized ePMOs described above. The loadings of the functionalized mAR-PMO materials as well as the catalytic results are shown in Table 3.4.

Table 3.4. Catalytic results of the functionalized mAR-PMO and the long linker ePMO (See also Scheme 3.3).

Entry	Sample	Loading ^a (mmol/g)	TOF (s^{-1})	Selectivity ^b (%)
1	Cys-mAR-PMO	0.35	- ^c	- ^c
2	Amine-mAR-PMO	0.37	$1.5 \cdot 10^{-6}$	92
3	C6-Amine-ePMO	0.36	$4.5 \cdot 10^{-6}$	92

^aLoading of nitrogen, from elemental analysis. ^bTowards aldol product **1**. ^cNo significant conversion was observed.

Surprisingly, no significant catalytic activity was observed for the cysteine-functionalized mAR-PMO. The amine-functionalized mAR PMO exhibited some activity, but the corresponding TOF value is two orders of magnitude lower than that of the functionalized ePMO. These results show that the grafting strategy to produce enamine catalysts cannot be generalized to all PMOs. There are several factors that could affect the activity of the functionalized mAR-PMO, compared to the ePMO, such as the pore structure, the amount of silanol groups on the surface and the linker chain length. These factors were investigated for both the monoallyl ring PMO and the ePMO, to study the differences between these materials. Table 3.5 gives a comparative overview of several properties for the two PMO materials, which are discussed in the following paragraphs.

Since the two PMOs were synthesized using the same template, namely P123, their mesopore structure should be very similar. Table 3.5 entries 1-6 give a comparative overview of the properties related to the porosity. The BET surface area is lower for the mAR-PMO, but the mesopore size and pore volumes are very similar for both PMOs. The difference in BET surface area can be attributed to a higher micropore volume for the ePMO (entries 4 and 5). In fact, in the case of the mAR-PMO, the micropores could be blocked by the dangling allyl functionality and therefore barely contribute to the BET surface area. However, due to their small diameter, the micropores are not expected to significantly contribute to the catalytic activity of the materials. So, if we subtract the micropore surface

area from the BET surface area for both materials, we find a similar mesopore surface area (entry 6).

Table 3.5. Comparative properties of the ePMO and monoallyl ring PMO materials.

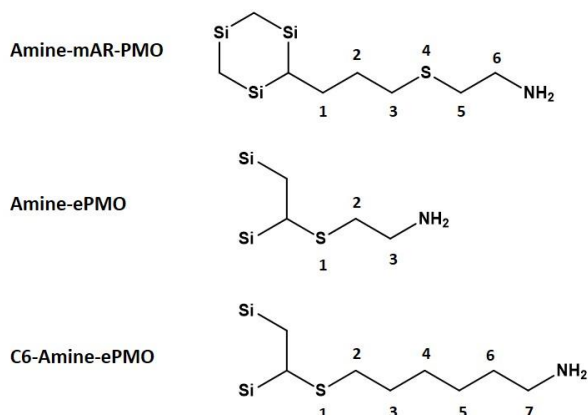
Entry	Property	ePMO	mAR-PMO
1	BET surface area	890 m ² /g	766 m ² /g
2	Average pore size ^a	5.2 nm	5.5 nm
3	Pore Volume ^b	0.98 ml/g	0.97 ml/g
4	Micropore Volume ^c	0.06 ml/g	~0 ml/g
5	Micropore surface area ^c	145 m ² /g	8 m ² /g
6	Mesopore surface area ^d	745 m ² /g	758 m ² /g
7	Surface silanol density	0.9 mmol/g or 0.6 per nm ²	0.4 mmol/g or 0.4 per nm ^{2e}

^a Based on the BJH distribution of the desorption branch. ^b Based on the desorption isotherm at P/P₀=0.95. ^c Based on t-plot analysis. ^d Difference of the BET surface area and the micropore surface area. ^e Silanol groups of mAR-PMO were measured on a different batch with a surface area of 607 m²/g.

Therefore, the differences shown in entries 1-6 of Table 3.5 are not expected to be decisive in the difference of catalytic behaviors of the two PMOs.

Since it was found in the previous sections that the surface silanol groups play a major part in the catalytic activity of the functionalized PMOs, the surface silanol density could affect the catalytic activity of the PMO. In order to quantify the accessible surface silanol groups, the PMO materials were reacted with HMDS and the carbon contents before and after the treatment were compared using CHN measurements. Taking into account that every silanol is functionalized with three carbon atoms, we can calculate the amount of HMDS-functionalized silanol sites in mmol/g.^{5,11} Using the BET surface areas, these values can then be converted to the amount of functionalized silanol sites per nm². These values are shown in Table 3.5, entry 7. While the value is higher for the ePMO, it is possible that a part of the HMDS functionalization in this case took place inside the micropores, and therefore the values are hard to compare when we only want to consider the mesopores. Additionally, the HMDS method is not ideal when used on PMOs. It is apparent from Figure 3.2 that on the ePMO, a silanol signal is still visible after capping. So even though the capping had a significant impact on the catalytic activity, it was not necessarily quantitative in capping all the surface silanols.

A final factor to take into consideration is the chain length of the grafted amine or cysteine moiety. Since the mAR-PMO has a dangling allyl chain, there are 6 atoms in between the PMO backbone and the primary amine. In the case of the ePMO, there are only 3 atoms in the chain. Therefore, an ePMO was grafted with 6-aminohexane-1-thiol, to yield a



Scheme 3.3. A comparison of the chain lengths of amine-mAR-PMO, Amine-ePMO and C6-Amine-ePMO.

functionalized ePMO with 7 atoms in between the PMO backbone and the primary amine (Scheme 3.3). The activity of this last material was tested under identical conditions as the other materials and the result is listed in Table 3.4. The long chain ePMO is much less active than the ePMO functionalized with cysteamine. It seems that the chain length is a determining factor, if not necessarily the only one.

This finding is quite surprising, when compared to previous reports in the literature. Brunelli et al.¹² synthesized aminated SBA-15 materials with increasing chain lengths between the silica surface and the amine. They tested these materials in the aldol reaction of 4-nitrobenzaldehyde and acetone. An overview of their results is shown in Figure 3.14. They found that the material with a chain length of three carbons performed optimally and the

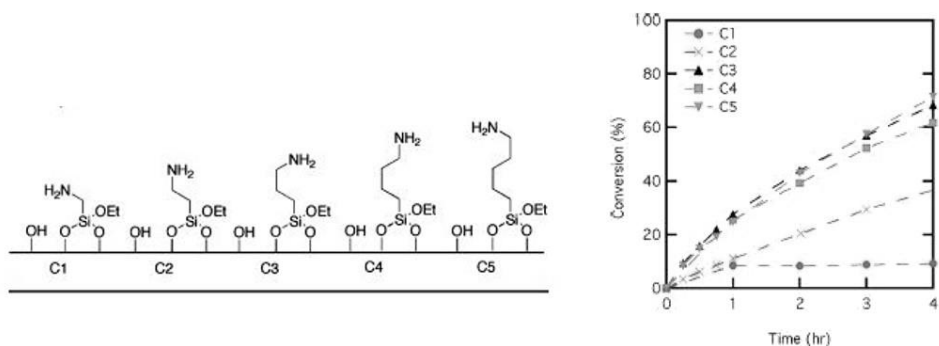


Figure 3.14. A representation of a series of aminated silica materials with increasing chain lengths reported by Brunelli et al. (left). A comparison of the catalytic activity of these materials in an aldol reaction (right).¹²

activity decreased marginally with increasing chain length. Shorter chain lengths on the other hand performed significantly worse.

On the PMO materials described here, clearly a different behavior is observed, even though Brunelli et al. used similar amine loadings and the silicas had a similar SBA-15 structure as the PMOs described here. At this time it is not clear what the reason is for this difference in behavior between the two materials is. It could possibly be related to the PMO surface which is more hydrophobic than the silica surface. In the case of Amine-mAR-PMO, the presence of a sulfur atom could also have an influence on the chain flexibility which might in turn affect the catalytic activity.

In conclusion, it seems that the difference in reactivity between the two types of PMOs, functionalized with amine or cysteine groups, is partially due to the chain length of the linker. However, there is still a difference in activity between the C6-Amine-ePMO and the Amine-mAR-PMO, which suggests that the chain length is not the only determining factor. The structure of a PMO is relatively complex and in addition it is amorphous and so not as neatly ordered as is the case for a crystalline material. It is therefore very difficult to determine exactly what is happening on the PMO surface and how each variable influences the catalytic activity. For instance, we cannot see the exact distribution of the active sites or the local silanol density in the vicinity of each active site. Therefore, the exact reason for the difference in activity of functionalized ePMO and mAR-PMO materials is not known.

3.5 Conclusions

A straightforward, single step procedure was developed to graft functional groups onto the ePMO. Cysteine and amine functionalized materials were obtained by a photoinitiated thiol-ene click reaction. Catalytic testing in an aldol reaction showed that the silanol groups present on the PMO surface are more effective as promoting site to the amine than carboxylic acid groups. In terms of the loading of the active sites, a lower loading gives a higher activity per unit of catalytic site. This can be rationalized by the formation of hydrogen bonds between the active sites at higher loadings, as was shown in the computational study. The synthesis method could be extended to a mAR-PMO, but with rather disappointing catalytic results. This difference in activity could be related to the increased chain length on the mAR-PMO, as well as other factors such as the surface silanol density.

3.6 Experimental details

Materials. The following chemicals were used as received: L-cysteine (>99%, Acros), Cysteamine (>95%, TCI), 2-Hydroxy-4-(2-hydroxyethoxy)-2-methylpropiophenone (Irgacure 2959, 98%, Aldrich), PEG-PPG-PEG Pluronic® P-123 (Aldrich), 1-Butanol (99.7%, Aldrich), HCl

(37%, Roth), vinyltriethoxysilane (97%, ABCR), Grubbs' catalyst (1st generation, 97%, Aldrich), HMDS (98.5%, ABCR), acetone (99.5%, Aldrich), dichloromethane (DCM, >99.5, Roth), 4-nitrobenzaldehyde (99%, Acros), n-hexane (Extra Pure, Acros), methyl 4-nitrobenzoate (>99%, Aldrich), 6-Amino-1-hexanethiol hydrochloride (Aldrich), CDCl₃ (99.8 atom% D, Aldrich) .

Synthesis of ePMO and ePMO-HMDS. 1,2-bis(triethoxysilyl)ethane (BTEE) and the ePMO were synthesized according to previously reported procedures.¹³ The 100% E-ethylene precursor was synthesized from vinyltriethoxysilane (42.95 ml), to which Grubbs' catalyst (53.5 mg) was added under inert atmosphere. The mixture was stirred for one hour and then refluxed at 160°C for three hours. Subsequent vacuum distillations at 90°C and 160°C were performed to obtain pure BTEE as the second distillate.

For the synthesis of the ePMO, P123 (1g), butanol (2.45 ml) and HCl (3.42 ml) were dissolved in water (48.7 ml) by stirring for 3 hours. BTEE (1.89 ml) was added dropwise and the mixture was stirred for 5 hours at 35°C. Butanol (18 ml) was added and the material was aged at 90°C under static conditions for 16 hours. The obtained white solid was filtered and the template was removed by Soxhlet extraction with acetone for 6 hours. The PMO was dried at 120°C in vacuo.

For the synthesis of ePMO-HMDS, ePMO (0.3 g) was stirred in HMDS (20ml) at room temperature, during 5 hours. The solid was filtered and washed with DCM. It was then stirred in DCM overnight, filtered and dried in vacuo at 120°C.

Synthesis of mAR-PMO. mAR-PMO was synthesized based on a previously reported procedure.¹⁴ P123 (0.375 g), KCl (2.19 g), HCl (37%, 0.9 ml) were dissolved in 11.25 ml water in a 50 ml flask. The mixture was stirred until the template and salt were completely dissolved (1 hour). Monoallyl ring precursor (0.563 g) was added while stirring the solution and the flask was put in an oil bath at 45°C. The solution was stirred at this temperature at 1000 rpm during 3 hours and then aged at 95°C during 24 hours, without stirring. The solid was filtered off and washed on the filter with water and acetone. The template was removed via Soxhlet extraction with acetone overnight. The solid was dried in vacuum at 120°C.

Grafting of functional groups on ePMO. The ePMO was first dried overnight at 120°C in vacuum. L-cysteine (0.875 g) or cysteamine (0.55 g) or 6-aminohexanethiol hydrochloride (14 mg) was dissolved in water (50 ml), along with Irgacure 2959 (0.425 g) and the solution was purged with argon. ePMO (0.425 g) or ePMO-HMDS (0.5 g) was added and the suspension was exposed to UV irradiation, while stirring. Different loadings of cysteine or amine were obtained by varying the reaction times between 15 minutes and 24 hours. UV

reactions were performed in a Metalight Classic UV reactor equipped with 12 UV sources (360 nm) and a stirring system.

For Cys-ePMO and Cys-ePMO-HMDS, the obtained yellow solid was filtered, washed with warm water and acetone, refluxed in water overnight, filtered and again washed with warm water and acetone. Finally, the product was dried in vacuum at 120°C.

For Amine-ePMO and Amine-ePMO-HMDS, the obtained yellow solid was washed by Soxhlet extraction with acetone for 6 hours and dried in vacuum at 120°C.

For C6-Amine-ePMO, the obtained solid was filtered and washed by Soxhlet extraction with acetone. Then, the solid was stirred in a 0.1M KOH solution, in order to remove the HCl. The material was then filtered, stirred in water for 3 hours, filtered and washed on the filter with water and ethanol and dried in vacuum at 120°C.

Grafting of functional groups on mAR-PMO. A similar method was used as for the grafting on ePMO. mAR PMO was dried overnight at 120°C in vacuum. Cysteine (1.5 mg) or cysteamine (1 mg) was dissolved in water (15 ml), along with Irgacure 2959 (20 mg) and the solution was purged with argon. mAR-PMO (0.1 g) was added and the suspension was exposed to UV irradiation for 2.5 hours. The materials were washed by Soxhlet with acetone, followed by stirring in water during 3 hours, filtration and washing on the filter with water and ethanol and dried in vacuum at 120°C.

Catalyst Characterization. FT-IR measurements were performed on a Nicolet 6700 (Thermo Scientific) with a KBr matrix, at 120°C, under vacuum. Elemental analysis was performed on a Thermo Flash 2000 Thermal Analyzer (Thermo Scientific). XRD was performed on a ARL X'TRA (Thermo Scientific). Nitrogen sorption measurements were performed on a TriStar 3000 analyzer (Micromeritics) after drying at 120° in vacuo. ¹H NMR was performed on a Bruker 300 MHz spectrometer, in CDCl₃.

Catalytic testing procedure. The experiments were performed in a 25 ml two-neck round-bottom flask equipped with a condenser and a septum. First, the supported catalyst was added to the flask so that the desired amount of amines was present, i.e., 4 mol-% with respect to the 4-nitrobenzaldehyde concentration. The reaction mixture was prepared separately by mixing the desired amounts of acetone (50 vol.-%), 4-nitrobenzaldehyde (0.03 mmol/ml), methyl 4-nitrobenzoate (internal standard, 0.022 mmol/ml) and n-hexane (solvent, 50 vol.-%). Afterwards, 5 ml of the reaction mixture was injected into the flask which contains the catalyst and the flask was immediately placed in an oil bath at 45 °C. The reaction was monitored by taking samples (about 50 μl) of the reaction mixture. Approximately 0.5 ml of acetone was used to wash the syringe needle and to transfer the sample to a vial. Subsequently, the catalyst was separated from the sample by means of

centrifugation. Finally, the samples were analyzed using a reversed-phase HPLC (Agilent 1100 series) equipped with a UV detector with variable wavelength. The HPLC was operated at a column temperature of 30°C using a gradient method with water (0.1% Trifluoroacetic acid) and acetonitrile (HPLC grade) as solvents. In this gradient method the volumetric percentage of acetonitrile is varied from 30% to 62% over a period of 7 minutes. The chirality of the aldol products was analyzed by chiral HPLC (Chiralpak AS-H, Hexane:Ethanol 90:10).

Computational Methodology. Static density functional theory (DFT) calculations were done within the Gaussian09¹⁵ package, using the hybrid B3LYP^{16, 17} functional combined with a triple zeta Pople basis set 6-311++G(d,p)¹⁸ for both optimization and frequency calculations. Empirical dispersion corrections were added using Grimme's D3 version with Becke-Johnson damping as implemented in Gaussian.^{19, 20} A simple model was constructed of a short chain, consisting of two linked precursor units, representative of the PMO backbone modified with one or two cysteine groups. The total stoichiometry of the model is hence $[\text{Si}(\text{OH})_3\text{C}_2\text{H}_3(\text{Cyst})\text{Si}(\text{OH})_2]_2\text{O}$. The chain was first optimized without the cysteine groups and its geometry was kept fixed during optimization of the complete model system, accounting for the rigidity of the PMO material. Molecular Dynamics simulations were performed using the CP2K²¹ package. A 22.0x22.0x22.0 Å box subjected to periodic boundary conditions was used. The BLYP functional was used together with empirical dispersion corrections (DFT-D3) to describe the long-distance van der Waals interactions.^{19, 20} A Gaussian and Plane waves method²² was chosen for all calculations, using a DZVP/TZVP Gaussian basis set for Si/C/S/H and O/N respectively and a plane wave basis set with a 280 Ry cut-off using Goedecker-Teter-Hutter pseudopotentials.^{23, 24} After initial heating using a CSV thermostat²⁵, a Nosé-Hoover thermostat^{26, 27} of 5 coupled heat baths was used to keep the system at 300K. In total, the NVT-simulations sampled 12 ps, using a 0.5 fs time step.

3.7 References

- [1] V.E. Collier, N.C. Ellebracht, G.I. Lindy, E.G. Moschetta, C.W. Jones, Kinetic and Mechanistic Examination of Acid-Base Bifunctional Aminosilica Catalysts in Aldol and Nitroaldol Condensations, *Acs Catalysis*, 6 (2016) 460-468.
- [2] J. Lauwaert, E.G. Moschetta, P. Van Der Voort, J.W. Thybaut, C.W. Jones, G.B. Marin, Spatial arrangement and acid strength effects on acid–base cooperatively catalyzed aldol condensation on aminosilica materials, *Journal of Catalysis*, 325 (2015) 19-25.
- [3] N.A. Brunelli, K. Venkatasubbaiah, C.W. Jones, Cooperative Catalysis with Acid–Base Bifunctional Mesoporous Silica: Impact of Grafting and Co-condensation Synthesis Methods on Material Structure and Catalytic Properties, *Chemistry of Materials*, 24 (2012) 2433-2442.
- [4] N.A. Brunelli, C.W. Jones, Tuning acid-base cooperativity to create next generation silica-supported organocatalysts, *Journal of Catalysis*, 308 (2013) 60-72.
- [5] J. Lauwaert, E. De Canck, D. Esquivel, J.W. Thybaut, P. Van Der Voort, G.B. Marin, Silanol-Assisted Aldol Condensation on Aminated Silica: Understanding the Arrangement of Functional Groups, *Chemcatchem*, 6 (2014) 255-264.
- [6] J.C. Hicks, R. Dabestani, A.C. Buchanan, C.W. Jones, Spacing and Site Isolation of Amine Groups in 3-Aminopropyl-Grafted Silica Materials: The Role of Protecting Groups, *Chem mater*, 18 (2006) 5022-5032.
- [7] M.W. McKittrick, C.W. Jones, Toward Single-Site Functional Materials Preparation of Amine-Functionalized Surfaces Exhibiting Site-Isolated Behavior, *Chem mater*, 15 (2003) 1132-1139.
- [8] M. Sharifi, C. Kohler, P. Tolle, T. Frauenheim, M. Wark, Proton Conductivity of SO₃H-Functionalized Benzene-Periodic Mesoporous Organosilica, *Small*, 7 (2011) 1086-1097.
- [9] A. Rimola, D. Costa, M. Sodupe, J.F. Lambert, P. Ugliengo, Silica Surface Features and Their Role in the Adsorption of Biomolecules: Computational Modeling and Experiments, *Chemical Reviews*, 113 (2013) 4216-4313.
- [10] G.A. Jeffrey, An introduction to hydrogen bonding, *Oxford University Press*, 1997.
- [11] M. Ide, M. El-Roz, E. De Canck, A. Vicente, T. Planckaert, T. Bogaerts, I. Van Driessche, F. Lynen, V. Van Speybroeck, F. Thybaut-Starzyk, P. Van Der Voort, Quantification of silanol sites for the most common mesoporous ordered silicas and organosilicas: total versus accessible silanols, *Physical Chemistry Chemical Physics*, 15 (2013) 642-650.

- [12] N.A. Brunelli, S.A. Didas, K. Venkatasubbaiah, C.W. Jones, Tuning Cooperativity by Controlling the Linker Length of Silica-Supported Amines in Catalysis and CO₂ Capture, *Journal of the American Chemical Society*, 134 (2012) 13950-13953.
- [13] C. Vercaemst, M. Ide, B. Allaert, N. Ledoux, F. Verpoort, P. Van Der Voort, Ultra-fast hydrothermal synthesis of diastereoselective pure ethylene-bridged periodic mesoporous organosilicas, *Chem Commun (Camb)*, (2007) 2261-2263.
- [14] S. Clerick, E. De Canck, K. Hendrickx, V. Van Speybroeck, P. Van der Voort, Heterogeneous Ru(III) oxidation catalysts via 'click' bidentate ligands on a periodic mesoporous organosilica support, *Green Chemistry*, 18 (2016) 6035-6045.
- [15] M.J. Frisch, G.W. Trucks, H.B. Schlegel, G.E. Scuseria, M.A. Robb, J.R. Cheeseman, G. Scalmani, V. Barone, B. Mennucci, G.A. Petersson, H. Nakatsuji, M. Caricato, X. Li, H.P. Hratchian, A.F. Izmaylov, J. Bloino, G. Zheng, J.L. Sonnenberg, M. Hada, M. Ehara, K. Toyota, R. Fukuda, J. Hasegawa, M. Ishida, T. Nakajima, Y. Honda, O. Kitao, H. Nakai, T. Vreven, J.A. Montgomery, J.E. Peralta, F. Ogliaro, M. Bearpark, J.J. Heyd, E. Brothers, K.N. Kudin, V.N. Staroverov, R. Kobayashi, J. Normand, K. Raghavachari, A. Rendell, J.C. Burant, S.S. Iyengar, J. Tomasi, M. Cossi, N. Rega, J.M. Millam, M. Klene, J.E. Knox, J.B. Cross, V. Bakken, C. Adamo, J. Jaramillo, R. Gomperts, R.E. Stratmann, O. Yazyev, A.J. Austin, R. Cammi, C. Pomelli, J.W. Ochterski, R.L. Martin, K. Morokuma, V.G. Zakrzewski, G.A. Voth, P. Salvador, J.J. Dannenberg, S. Dapprich, A.D. Daniels, Farkas, J.B. Foresman, J.V. Ortiz, J. Cioslowski, D.J. Fox, Gaussian 09, Revision D.01, Wallingford CT, 2009.
- [16] A.D. Becke, DENSITY-FUNCTIONAL THERMOCHEMISTRY .3. THE ROLE OF EXACT EXCHANGE, *Journal of Chemical Physics*, 98 (1993) 5648-5652.
- [17] C.T. Lee, W.T. Yang, R.G. Parr, DEVELOPMENT OF THE COLLE-SALVETTI CORRELATION-ENERGY FORMULA INTO A FUNCTIONAL OF THE ELECTRON-DENSITY, *Physical Review B*, 37 (1988) 785-789.
- [18] R. Krishnan, J.S. Binkley, R. Seeger, J.A. Pople, SELF-CONSISTENT MOLECULAR-ORBITAL METHODS .20. BASIS SET FOR CORRELATED WAVE-FUNCTIONS, *Journal of Chemical Physics*, 72 (1980) 650-654.
- [19] S. Grimme, J. Antony, S. Ehrlich, H. Krieg, A consistent and accurate ab initio parametrization of density functional dispersion correction (DFT-D) for the 94 elements H-Pu, *Journal of Chemical Physics*, 132 (2010) 154104.
- [20] S. Grimme, S. Ehrlich, L. Goerigk, Effect of the Damping Function in Dispersion Corrected Density Functional Theory, *Journal of Computational Chemistry*, 32 (2011) 1456-1465.

- [21] J. Hutter, M. Iannuzzi, F. Schiffmann, J. VandeVondele, CP2K: atomistic simulations of condensed matter systems, *Wiley Interdisciplinary Reviews-Computational Molecular Science*, 4 (2014) 15-25.
- [22] G. Lippert, J. Hutter, M. Parrinello, A hybrid Gaussian and plane wave density functional scheme, *Molecular Physics*, 92 (1997) 477-487.
- [23] C. Hartwigsen, S. Goedecker, J. Hutter, Relativistic separable dual-space Gaussian pseudopotentials from H to Rn, *Physical Review B*, 58 (1998) 3641-3662.
- [24] S. Goedecker, M. Teter, J. Hutter, Separable dual-space Gaussian pseudopotentials, *Physical Review B*, 54 (1996) 1703-1710.
- [25] G. Bussi, D. Donadio, M. Parrinello, Canonical sampling through velocity rescaling, *Journal of Chemical Physics*, 126 (2007) 014101.
- [26] S. Nose, A MOLECULAR-DYNAMICS METHOD FOR SIMULATIONS IN THE CANONICAL ENSEMBLE, *Molecular Physics*, 52 (1984) 255-268.
- [27] S. Nose, A UNIFIED FORMULATION OF THE CONSTANT TEMPERATURE MOLECULAR-DYNAMICS METHODS, *Journal of Chemical Physics*, 81 (1984) 511-519.

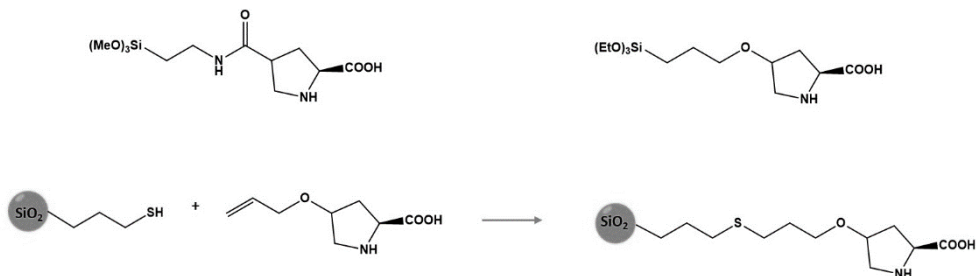
Chapter 4.

Proline-functionalized PMOs for asymmetric enamine catalysis

4.1 Introduction to immobilized proline

Several efforts have been reported to immobilize L-proline on solid supports. Different types of materials, such as polymers, silicas and other inorganic materials have been investigated, using several different anchoring methods. In polymer chemistry, the most common strategy is the synthesis of a proline-bearing monomer, which can be copolymerized with common monomers to form proline-modified polystyrene^{1, 2} or polyamide³ materials. Layered double hydroxides can be functionalized with proline by intercalating it in between the layers of the material.⁴ Zirconium phosphates can be functionalized by reacting a phosphoric acid-modified proline onto the surface.⁵ Proline has also been confined in the pores of a faujasite-type zeolite.⁶ All these materials could be used as enantioselective heterogeneous catalysts.

Mesoporous silicas were also functionalized with proline using different methods. Several research groups synthesized proline-bearing silanes, which could be introduced onto mesoporous silicas via grafting or co-condensation.⁷⁻¹⁰ Some examples are shown in Scheme 4.1 (top). The materials functionalized with these silanes catalyzed asymmetric aldol reactions, with ee values similar to or somewhat lower than homogeneous L-proline. Another method is the use of a thiol-ene click reaction. In that case, a commercial hydroxyproline first needs to be allylated. Then, a mesoporous silica is functionalized with a mercaptosilane. The proline moiety can then be clicked onto the support (Scheme 4.1, bottom).^{11, 12}



Scheme 4.1. Two examples of proline-bearing silanes (top) and a thiol-ene click method for functionalization of a silica with proline (bottom).

One limitation of the latter method is the limited hydrolytic stability of the resulting material. Since the active site is attached to the carrier material via a siloxane bond, it is vulnerable to hydrolysis. The hydrolytic stability of the proline group is particularly important when the catalyst is used in aldol reactions, because they are often performed in the presence of water. In fact, many proline-based catalysts were found to get increased reaction rates but also increased enantioselectivities in the presence of water.¹³ This is especially true for catalysts containing hydrophobic substituents or catalysts immobilized on hydrophobic supports. Since PMOs are relatively hydrophobic, compared to silicas, they could have an interesting effect on the activity of an immobilized proline moiety.

4.2 Set-up and aim of the research

In this chapter, a thiol-ene click functionalization, similar to the one shown in Scheme 4.1 is discussed. A thiol PMO was used as support, which contains the thiol functionality on the PMO backbone. Therefore, grafting the proline on this thiol could result in a material that is more hydrolytically stable, compared to materials where the thiol group was incorporated via the grafting or co-condensation of a mercaptosilane. Two thiol-ene click reactions were applied to the thiol PMO, namely a thermally activated and a UV-activated method. The resulting materials were tested for their activity in the aldol test reaction, as well as for their enantioselectivity towards the aldol product. When both of these methods failed to produce successful catalysts starting from the thiol PMO, several more materials were functionalized in an attempt to rationalize the obtained results.^a

^a All material syntheses and characterizations as well as catalytic tests were performed by the author. Catalytic results were analyzed by the author, with help from Jan Goeman for the chiral analyses.

4.3 Results and discussion

4.3.1 Synthesis and characterization of the 25% thiol PMO

As mentioned in Chapter 1, our group developed a thiol PMO precursor which can be used to synthesize a 100% thiol PMO.¹⁴ The thiol precursor is obtained by treating an ethene PMO precursor with thioacetic acid in a thiol-ene-type click reaction, followed by aminolysis with propylamine (see also Scheme 1.6). The ¹H NMR of the thiol precursor is shown in Figure 4.1.^b The sample contains some impurities, namely the propylamide formed during the synthesis and a propylammonium-thioacetate salt, formed by the excess of thioacetic

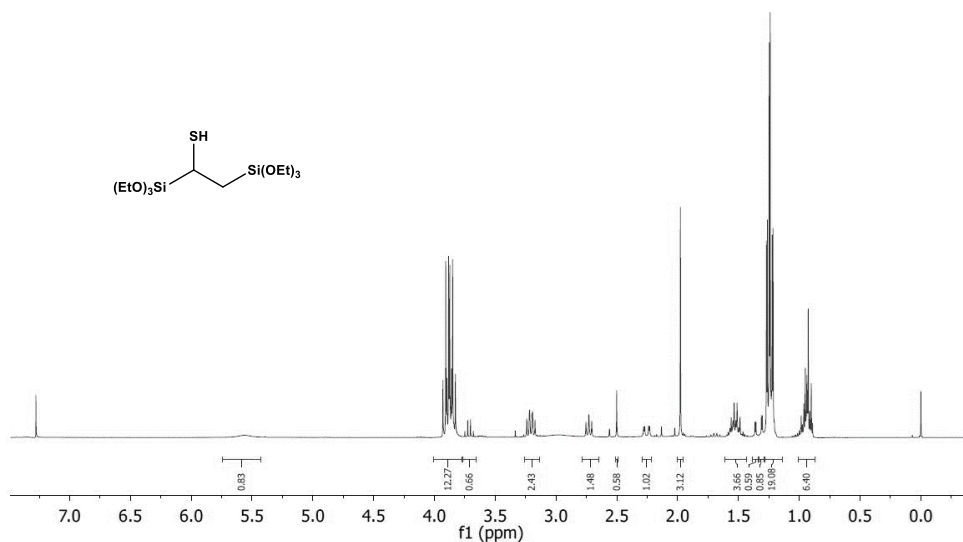
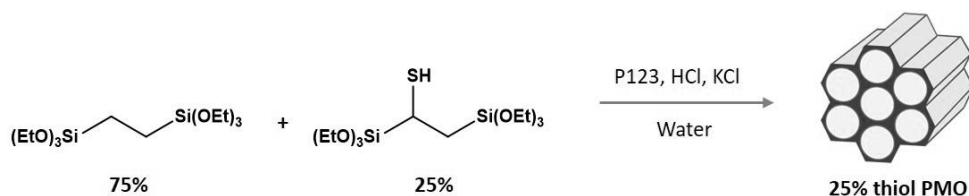


Figure 4.1. The ¹H NMR spectrum of the thiol PMO precursor, measured in CDCl₃.

acid and propylamine used during the synthesis. However, the precursor can be used as is in the PMO synthesis and the impurities are washed out during the filtration of the material.

The purpose of the thiol group in this case is to anchor a proline moiety on the PMO via a thiol-ene click reaction. As discussed in Chapter 3 regarding the PMOs functionalized with cysteine and cysteamine, a high loading of active sites in enamine catalysis is not necessarily beneficial. Therefore, a 100% loading of thiol groups is not necessary in this case. Instead, a 25% thiol PMO was synthesized, by co-condensing 25% of 1,2-bis(triethoxysilyl)thio-ethane

^b ¹H NMR (300 MHz, CDCl₃) Thiol precursor: δ = 3.78 (m, 1H), 3.87 (m, 12H, OCH₂CH₃), 2.26 (dd, J = 12.3, 2.5 Hz, 1H, CHSH), 1.24 (m, 18H, OCH₂CH₃), 0.96 (m, 2H, CH₂CH). Propylammonium-thioacetate salt: δ = 2.73 (m, 2H, CH₂CH₂NH₂), 2.50 (s, 3H, CH₃(C=O)) 1.51 (m, 2H, CH₃CH₂CH₂), 0.96 (m, 3H, CH₃CH₂). Propylamide: δ = 3.19 (m, 2H, CH₂CH₂NH), 1.98 (s, 3H, CH₃(C=O)), 1.52 (m, 2H, CH₃CH₂CH₂), 0.96 (m, 3H, CH₃CH₂CH₂).



Scheme 4.2. The synthesis conditions for the 25% thiol PMO

(BTETE) and 75% of 1,2-bis(triethoxysilyl)ethane (BTEE), using P123 as template (Scheme 4.2). This material was previously reported by our group in the context of mercury adsorption on a series of thiol PMOs.¹⁵ The 25% thiol PMO was visualized by HAADF-STEM^c and EDX^d mapping, as shown in Figure 4.2. In image **a**) in Figure 4.2, the cylindrical pore structure induced by the P123 template is visible and in image **b**), the hexagonal ‘honeycomb’ pore structure can be seen. (The white spots on these images indicate adsorbed mercury clusters, which were not present for the application of this material as proline-support.) Images c-e in Figure 4.2 show the EDX mapping of silicon, oxygen and sulfur on a STEM-HAADF image of the 25% thiol PMO. While the Si and O atoms are densely

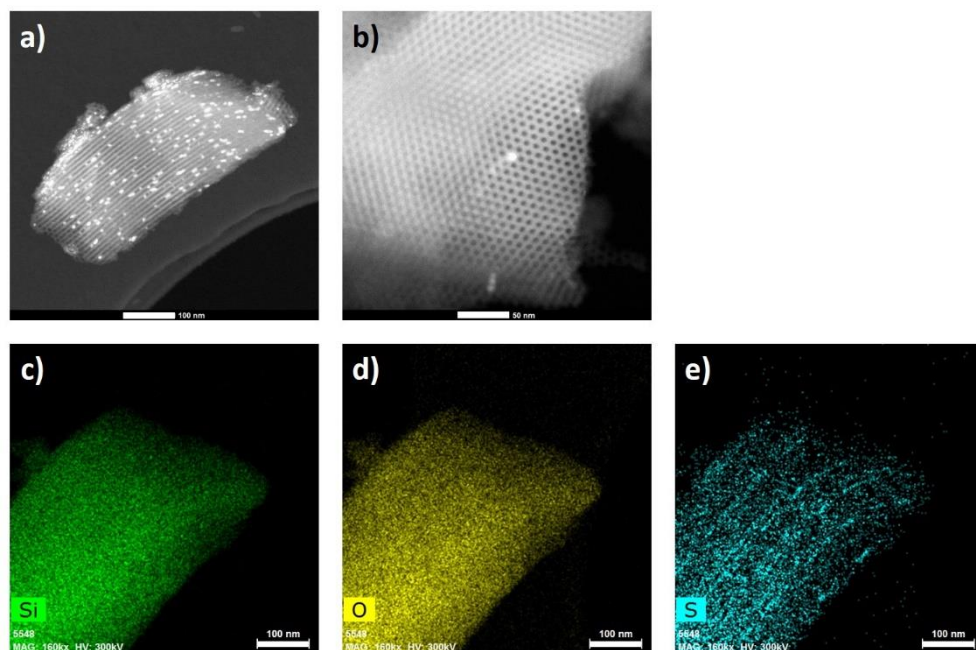


Figure 4.2. HAADF-STEM images of the 25% thiol PMO (a,b) with EDX mapping for Si, O and S (c-e). The scale bars indicate 100 nm for all images except b), which has a 50 nm scale bar.

^c High-angle annular dark-field scanning transmission electron microscopy

^d Energy-dispersive X-ray spectroscopy

distributed in the PMO structure, as would be expected in an organosilica, the S atoms are more sparse, due to the 25% loading. While the resolution of image e is not high enough to observe single sulfur atoms, it seems that the thiol groups (and possibly disulfide groups, see further text) are homogeneously distributed throughout the sample. This is important for the anchoring of proline, because a homogeneous distribution of the proline moieties is desirable.

The 25% thiol PMO was further investigated with nitrogen sorption, XRD, FT-Raman and CHNS elemental analysis. Figure 4.3 shows the nitrogen sorption isotherm and the pore size distribution of the PMO. The BET surface area of the PMO is 547 m²/g and the pore volume is 0.62 ml/g. The BJH pore size distribution shows that the main mesopore size is approximately 5.5 nm. The shape of the isotherm indicates that some macropores are present in the sample as well. The XRD measurement of the PMO is shown on the right side of Figure 4.3. We can see the characteristic (100) reflection of the hexagonal pore structure at 1° and a secondary (110) reflection can only just be distinguished at 1.8°. These data show that the ordering of the 25% thiol PMO is slightly less pronounced than for instance the ePMO discussed in Chapter 3, where both secondary reflections are clearly visible at 1.8° and 2°. The XRD looks very similar to that of an ethene PMO (See further, section 4.3.2.4). It seems that the excellent ordering of the ePMO is caused by pi-interactions of the ethene functional groups, which are not present in the 25% thiol PMO and the ethane PMO.

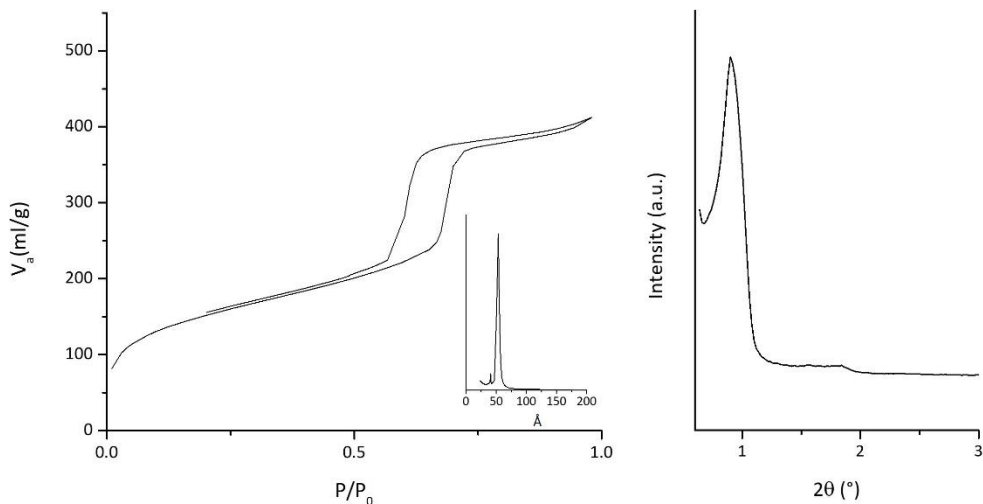


Figure 4.3. Nitrogen sorption isotherm (left) and XRD diffractogram (right) of the 25% thiol PMO. The inset of the isotherm shows the BJH pore size distribution based on the desorption branch.

The amount of sulfur in the 25% thiol PMO was determined via CHNS elemental analysis. The material contains 0.7 mmol/g of sulfur. However, the sulfur could be present in two different forms, namely the thiol form and the disulfide form. This is due to the fact that two thiol functionalities in each other's vicinity can form a disulfide bond via an oxidative reaction. It is expected that a portion of the thiol groups on the PMO will undergo this transformation. These two forms can be distinguished via FT-Raman spectroscopy (Figure 4.4). The thiol signal is present at 2570 cm^{-1} and the disulfide signal can be seen at 510 cm^{-1} . The other main signals can be assigned to CH stretch (2890 cm^{-1}) and CH bending (1410 cm^{-1}).

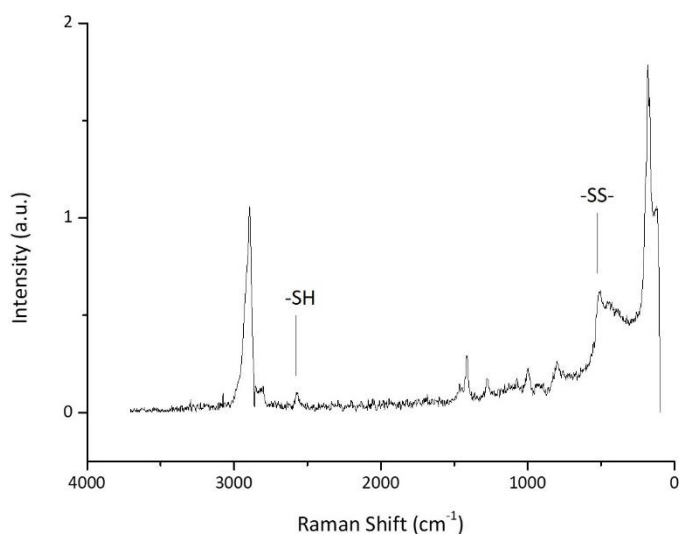
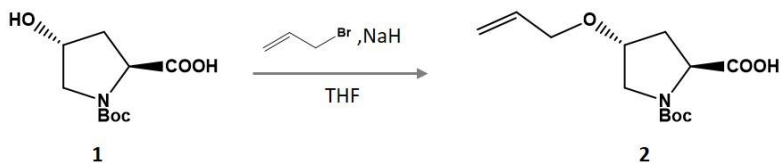


Figure 4.4. FT-Raman spectrum of the 25% thiol PMO.

4.3.2 Proline-functionalization of the PMO

4.3.2.1 Allylation of hydroxyproline

In order to graft a proline moiety on the 25% thiol PMO using the convenient thiol-ene click reaction, we have to introduce an allyl group onto proline. Since proline itself has no anchoring points, we instead started from the commercial Boc-protected hydroxyproline **1**. This compound was allylated with allyl bromide, as shown in Scheme 4.3. Two equivalents of sodium hydride are used to deprotonate both the carboxylic acid and the alcohol. Upon addition of allyl bromide, the hydroxyl moiety acts as nucleophile in an S_N2 reaction with the elimination of bromide. After workup, this results in the Boc-protected allylated proline **2** with a yield of 85% (see section 4.5 for all experimental details related to this chapter).



Scheme 4.3. The alkylation of the Boc-protected hydroxyproline.

The ^1H NMR of the allylated Boc-proline is shown in Figure 4.5.^e All the NMR peaks could be assigned to the expected structure, so it seems that the alkylation procedure was successful.

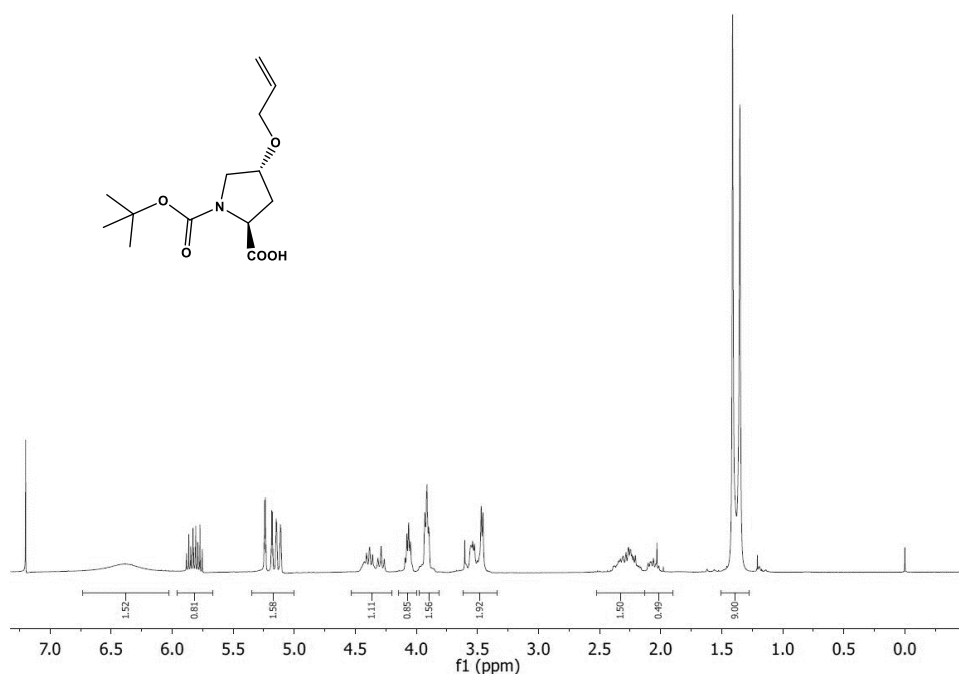
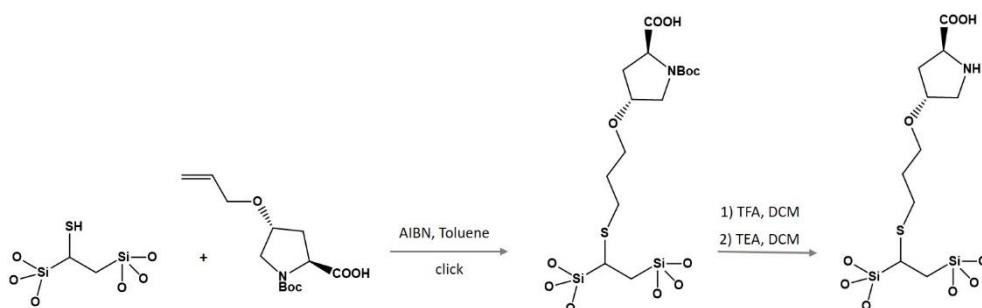


Figure 4.5. ^1H NMR spectrum of the allylated Boc-proline, measured in CDCl_3 .

^e ^1H NMR (300 MHz, CDCl_3) δ = 6.24 (s, 1H, COOH), 5.82 (ddt, J = 17.2, 10.5, 5.6 Hz, 1H, $\text{CH}_2\text{CH}=\text{CH}_2$), 5.18 (m, 2H, $\text{CH}=\text{CH}_2$), 4.34 (dt, J = 28.7, 7.5 Hz, 1H, $\text{CH}(\text{O})(\text{CH}_2)_2$), 4.05 (m, 1H, $\text{CH}_2\text{CH}=\text{CH}_2$), 3.92 (m, 1H $\text{CH}_2\text{CH}=\text{CH}_2$), 3.52 (m, 2H, $\text{CH}_2(\text{NH})(\text{CH})$), 1.90-2.40 (m, 2H, $\text{CH}_2(\text{COOH})(\text{CH})$), 1.38 (m, 9H, $\text{C}(\text{CH}_3)_3$).

4.3.2.2 The thermal anchoring method

The allylated product **2** can be grafted onto the 25% thiol PMO via the thiol-ene click reaction. In the literature, the thiol-ene coupling of **2** has been reported using AIBN as radical initiator and dry toluene as solvent. This method uses heating as activation method of the radical initiator. After anchoring of the proline moiety, the Boc group is removed by an acid treatment, using trifluoroacetic acid (TFA). A basic treatment with triethylamine (TEA) is then used to remove the remaining acid. A reaction scheme for this method applied to the 25% thiol PMO is shown in Scheme 4.4. The resulting material is denoted as Pro-PMO-Th, with Th designating the thermally activated click reaction. The nitrogen loading of this sample was 0.43 mmol/g according to elemental analysis.



Scheme 4.4. Reaction scheme for the thermal modification method on the 25% thiol PMO.

The DRIFTS spectra of the 25% thiol PMO before grafting, after grafting and after Boc-deprotection are shown in Figure 4.6. The silanol band is visible at 3730 cm^{-1} for all samples, as well as C-H signals between 3000 and 2750 cm^{-1} . The bands at 1420 and 1270 cm^{-1} could tentatively be assigned to alcohol and ether functionalities, respectively, which could arise from remaining P123 surfactant. From these DRIFTS measurements, almost no difference can be seen between the materials before and after functionalization. The only difference which could possibly be interpreted as significant is the increase of the signal at 1720 cm^{-1} for Boc-Pro-PMO-Th, which could indicate the carbamate functionality of the Boc-group. However, it is not clear why a signal is already present at the same wavenumber on the 25% thiol PMO, before functionalization. The lack of change in the DRIFTS spectra after functionalization could be because the obtained proline loading was too low to detect any difference, or because the proline anchoring was not successful. To gather more information, the material was catalytically tested. The catalytic results of this material are discussed in detail in the following section.

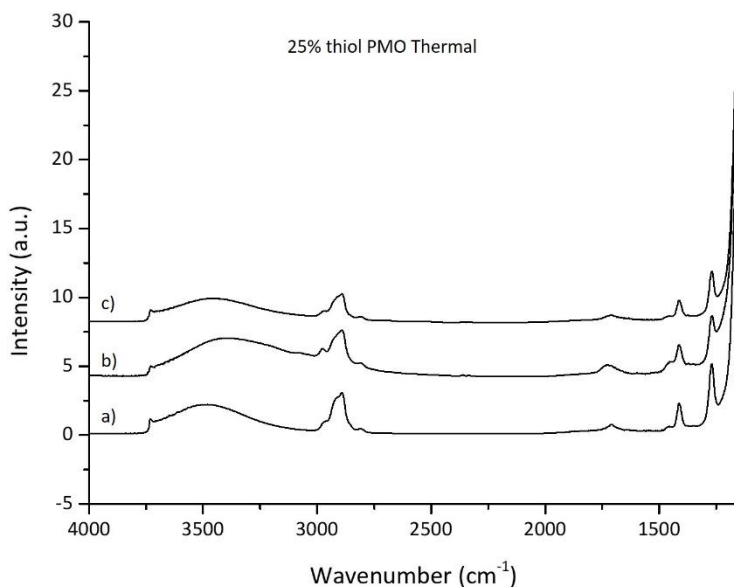


Figure 4.6. DRIFTS spectra of 25% thiol PMO (a), Boc-Pro-PMO-Th (b) and Pro-PMO-Th (c).

4.3.2.3. The UV anchoring method

Because the thermal functionalization method, taken from the literature, did not yield satisfying results on the 25% thiol PMO, a different functionalization method was devised. It was inspired by the click reaction of cysteine on the ePMO, described in Chapter 3. This thiol-ene click reaction was performed in water, using Irgacure 2959 as radical initiator with UV activation. Since the 25% thiol PMO is stable in water and the thiol functionality was directly incorporated into the PMO precursor (as opposed to using a mercaptosilane), this material could also be functionalized in similar conditions. The Boc-deprotection could also be performed in water, using HCl as the acid, which was subsequently removed using NaOH. Table 4.1 shows a comparison between the thermal and UV modification methods.

Table 4.1. Synthesis conditions of Pro-PMO-Th and Pro-PMO-UV.

	Pro-PMO-Th	Pro-PMO-UV
Solvent	Dry toluene	Distilled water
Radical Initiator	AIBN	Irgacure 2959
Evacuation method	Freeze-pump-thaw (x3)	Bubbling argon
Activation method	Heating (90°C)	UV irradiation
Deprotection method	TFA in dry DCM	HCl in water
Base used after deprotection	TEA in DCM	NaOH in water

One advantage of the UV method is that the Boc-allyl proline (**2**) is more readily soluble in water than in toluene. The method is also more benign, as water is used as the only solvent. More importantly, in the UV method, the proline moiety is the only nitrogen source in the entire synthetic procedure. This in contrast to the thermal method, where the radical initiator (AIBN), as well as the base used after deprotection (TEA), both contain nitrogen. This means that the nitrogen content determined by elemental analysis can, in theory, only indicate the proline loading in the UV method, while in the thermal method some nitrogen could be left over from the AIBN or TEA due to insufficient washing of the materials. The downside of the UV method is that it could only be performed on the thiol PMO, as materials grafted with a mercaptosilane would undergo severe leaching in the used reaction conditions.

The DRIFTS spectra for the Pro-PMO-UV sample before and after functionalization are shown in Figure 4.7. As was the case for the DRIFTS spectra of Pro-PMO-Th (Figure 4.6), very little difference can be seen after functionalization of the material. Again the signal at 1720 cm^{-1} increases on the Boc-Pro-PMO-UV sample, which could indicate the Boc-group. On the same spectrum, a band appears at 1630 cm^{-1} , which could also arise from the carbonyl of the Boc-group.

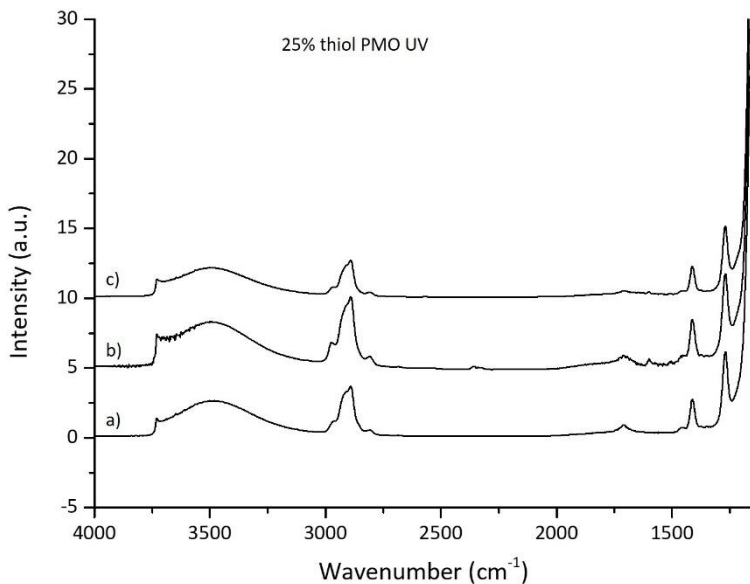


Figure 4.7. DRIFTS spectra of 25% thiol PMO (a), Boc-Pro-PMO-UV (b) and Pro-PMO-UV (c).

According to elemental analysis, the Pro-PMO-UV contained 0.27 mmol/g of nitrogen. Comparative CHNS data for the PMOs functionalized by thermal and UV methods are shown in Table 4.2. We can see that the starting material contained no nitrogen, but the

reactivity, based on the literature. Some reports mention that the presence of water can increase the yield of the aldol addition product without sacrificing the enantioselectivity. The catalytic reactions were first assessed after 24 hours (Table 4.3). The activities were disappointing and the conversions were too low to determine ee values. The addition of water to the reaction mixture did not drastically increase the activity and the 10 vol% of water even decreased the conversion after 24 hours.

In order to increase the conversion sufficiently to determine ee values, the reactions were run for one week. The temperature was increased to 35°C for the slowest reaction (Pro-PMO-Th) in an attempt to boost the conversion. However, the conversion only reached 0.8% after one week of reaction time for this catalyst. Two of the reactions using Pro-PMO-UV as catalyst reached sufficient conversion after one week to determine the ee values. However, no significant enantioselectivity was observed.

Table 4.3. Catalytic results of Pro-PMO-UV, using acetone and different amounts of water, during 24 hours.

Catalyst	Solvent	Cat. Loading (%)	Temp. (°C)	Conversion (%)	Selectivity ^a (%)	ee (%)
Pro-PMO-Th	Acetone	35.5	25	0.1	-	-
Pro-PMO-UV	Acetone	33.1	25	7.6	98	-
Pro-PMO-UV	Acetone +10 vol% water	34.5	25	3.6	98	-
Pro-PMO-UV	Acetone +100 vol% water	34.7	25	11.4	>99	-

^a Towards the aldol addition product.

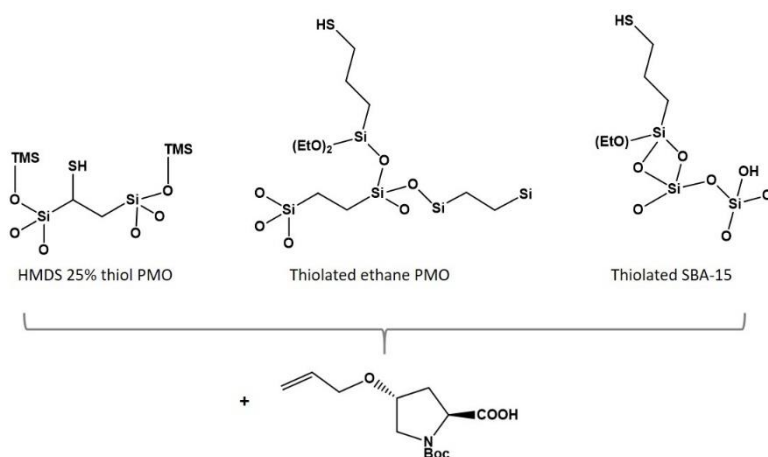
Table 4.4. Catalytic results of Pro-PMO-UV after one week, using acetone and different amounts of water.

Catalyst	Solvent	Cat. Loading (%)	Temp. (°C)	Conversion (%)	Selectivity (%) ^a	ee (%) ^b
Pro-PMO-Th	Acetone	35.5	25°C for 2 days, 35°C for 5 days	0.8	97	-
Pro-PMO-UV	Acetone	33.1	25	28	95	3
Pro-PMO-UV	Acetone +10 vol% water	34.5	25	14	96	-
Pro-PMO-UV	Acetone +100 vol% water	34.7	25	33	98	<1

^a Towards the aldol addition product ^b Towards the *R*-isomer.

4.3.2.4 Revisiting the thermal anchoring method

In order to gather some more information on the thermal functionalization method, three other materials were subjected to the same procedure. This could help us understand if the anchoring procedure itself is ineffective, or whether the 25% thiol PMO structure is the reason for the lack of conversion and selectivity observed in the previous section. Firstly, a 25% thiol PMO was treated with HMDS to cap the surface silanol groups. Secondly, mercaptopropyl triethoxysilane (MPTES) was grafted onto an SBA-15 material and an ethane PMO. These three materials were subjected to the same thermal functionalization procedure as the 25% thiol PMO in the previous section. A comparison between the three materials obtained via the thermal modification method is shown in Scheme 4.6.



Scheme 4.6. Schematic representation of the HMDS 25% thiol PMO, the thiolated ethane PMO and the thiolated SBA-15, which were all functionalized with the allylated proline. (TMS = Trimethylsilyl)

The three materials were all synthesized using the P123 precursor and should therefore have very similar mesopore structures. Structural analysis of the SBA-15 and the ethane PMO was performed using nitrogen sorption and XRD. The obtained results are shown in Figure 4.8 and Figure 4.9. The SBA-15 has a specific surface area of 658 m²/g and a very high degree of pore ordering. The XRD data clearly show the secondary (110) and (200) reflections. The ethane PMO has a high surface area of 1120 m²/g but a lower pore ordering. Both materials have very similar narrow pore size distributions with a maximum at 5.5 nm. After the proline modification of the three materials, DRIFTS analysis was performed, as shown in Figure 4.10. On the DRIFTS spectra of these materials, a clear signal appears around 1720 cm⁻¹ after the click reaction and disappears again (or is greatly reduced) after

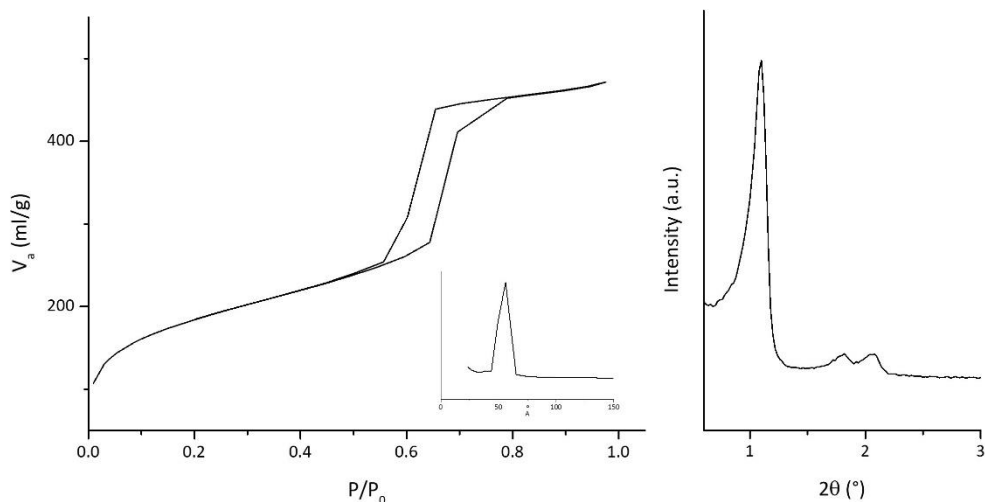


Figure 4.8. Nitrogen sorption isotherm (left) with BJH pore size distribution in the inset and XRD diffractogram (right) of the SBA-15.

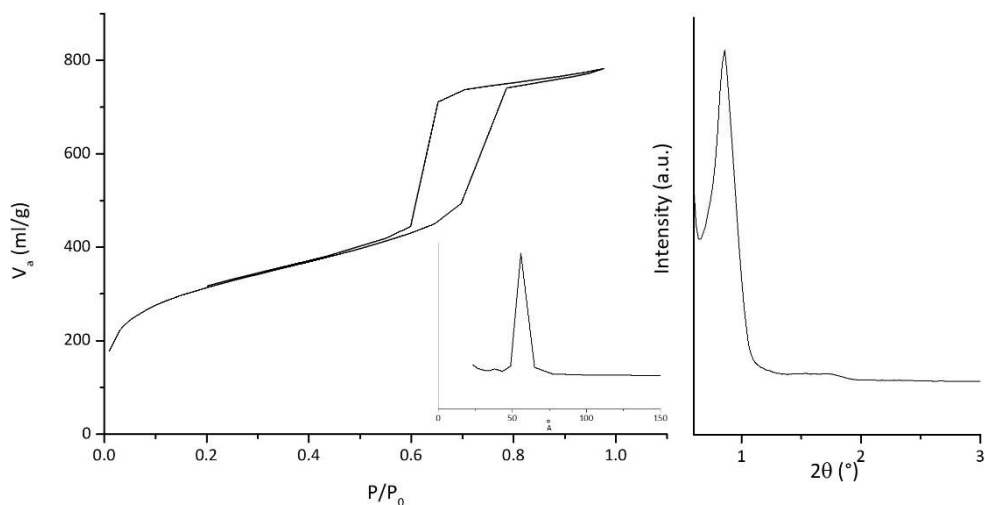


Figure 4.9. Nitrogen sorption isotherm (left) with BJH pore size distribution in the inset and XRD diffractogram (right) of the ethane PMO.

the Boc-deprotection. This signal could belong to the carbamate functionality of the Boc-group. It is much more pronounced on these materials than on the Pro-PMO-Th and Pro-PMO-UV samples. On the Boc-Pro-SBA-Th sample, a signal also appears at 1400 cm^{-1} , which could belong to the carboxylic acid. This signal could be masked on the PMO materials because there is already a signal present in that area. However, no other signals clearly

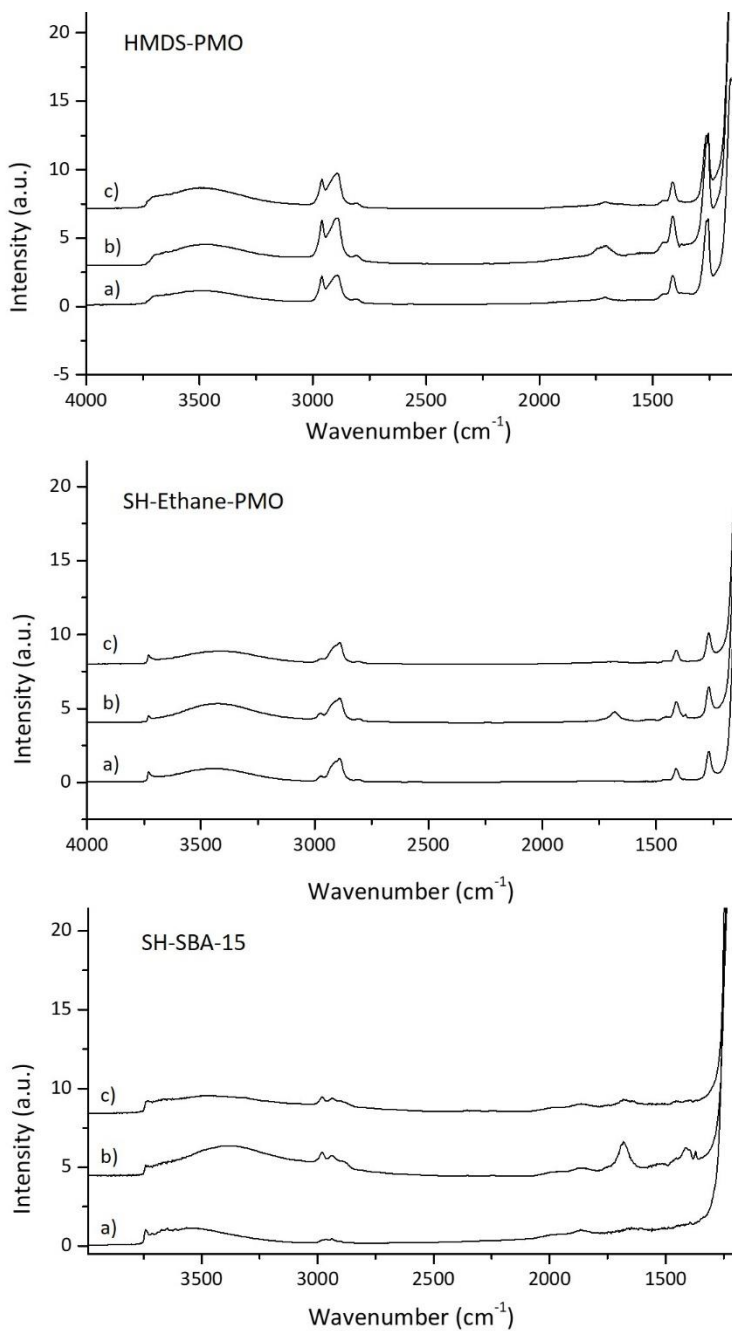


Figure 4.10. DRIFTS spectra of HMDS-PMO (top), SH-ethane-PMO (middle) and SH-SBA-15 (bottom). Spectrum a) shows the starting material, spectrum b) the Boc-proline-functionalized material and spectrum c) the proline-functionalized material.

show that the grafting of proline was successful. Elemental analysis showed a nitrogen content of 0.32 mmol/g for Pro-HMDS-PMO, 0.48 mmol/g for Pro-SBA-15 and 0.43 mmol/g for Pro-ethane-PMO.

The catalytic results for the heterogeneous catalysts synthesized via the thermal anchoring method are shown in Table 4.5 and Table 4.6. The loading of the catalysts was kept around 35 mol% with respect to 4-nitrobenzaldehyde (with the exception of Pro-ethane-PMO-Th, which had a higher loading due to a practical issue). Table 4.5 shows the conversion of the samples after 24 hours of reaction time. The conversion is disappointing for all catalysts in comparison to homogeneous L-proline. The exception is Pro-SBA-Th, which reaches nearly full conversion in 24 hours. However, the resulting aldol product is racemic which suggests that the anchored proline moiety is not the active species in this reaction. A hot filtration experiment confirmed this, as the filtrate also went to full conversion after removal of the Pro-SBA-Th material. This indicates that on this sample, probably some acid or base still remains from the Boc-deprotection procedure, which can catalyze the aldol reaction.

Table 4.5. Catalytic results of the heterogeneous catalysts. All reactions were performed in acetone, without addition of any solvents, during 24 hours.

Catalyst	Cat. Loading (%)	Temperature (°C)	Conversion (%)	Selectivity (%) ^a	ee (%) ^b
Pro-SBA-Th	37.8	25	98.7	89	<1
Pro-ethane-PMO-Th	58.2	25	11.9	>99	-
Pro-HMDS-PMO-Th	35.2	25	8.0	95	-

^a Towards the aldol addition product. ^b Towards the *R*-isomer.

The enantioselectivity of the other samples after 24 hours was not determined, due to the low conversion. In order to get the ee values for the remaining samples, the reactions were run for one week. The slowest reaction was increased to 35°C after 2 days in an attempt to boost the conversion. The resulting catalytic data are shown in Table 4.6. The functionalized ethane PMO and HMDS PMO samples reached significant conversion and the ee values could be determined. Both samples showed significant ee values of 42% and 32%, respectively.

This is a very good result as compared to the functionalized 25% thiol PMO, although the ee values are moderate in comparison to homogeneous L-proline. Also, the conversion rate of the samples is still low.

Table 4.6. Catalytic results of the heterogeneous catalysts after one week of reaction time. All reactions were performed in acetone

Catalyst	Cat. Loading (%)	Temperature (°C)	Conversion (%)	Selectivity ^a (%)	ee ^b (%)
Pro-ethanePMO-Th	58.2	25°C for 6 days	43	81	42
Pro-HMDS-PMO-Th	35.2	25°C for 2 days, 35°C for 5 days	19.3	93	32

^a Towards the aldol addition product. ^b Towards the *R*-isomer.

After finding that two of the materials functionalized by the thermal method showed enantioselective properties, we can now assume that the proline functionalization method is successful and that the low activity of the proline –functionalized 25% thiol PMO is related to the properties of this material, rather than intrinsic problems with the thermal functionalization method. One of the similarities between the Pro-ethane-PMO-Th and Pro-HMDS-PMO-Th samples is that they are both PMO samples with inaccessible silanol sites. On the HMDS-PMO, the silanol groups were capped before the click functionalization and on the ethane PMO, the silanol groups were functionalized with the mercaptosilane. This could be a significant reason why these materials were active and the functionalized 25% thiol PMO was not.

As to which properties of the different materials were determining for the differences in activity and why, we can only speculate at this point. For instance, it's possible that the capping of the silanol groups is important here because there is no cooperativity between the silanol and the amine on the proline functionality. Therefore, if the carbonyl species interact with the silanol groups, they are possibly not attainable by the enamine species. Also the chain length of the materials could play a role, as the Pro-ethane PMO showed higher activity than the Pro-HMDS-PMO. It is possible that with a short linker such as the one obtained when using the thiol-ene click reaction on a thiol PMO is not ideal. Maybe the proline moiety doesn't have enough space or flexibility to form the correct transition state. This could also affect the enantioselectivity of the material. Further research on this topic could possibly elucidate these factors and their impact on the catalytic performance.

4.4 Conclusion

In this chapter, the proline-functionalization of a 25% thiol PMO was described. Two modification methods were attempted but both resulting materials performed poorly in the asymmetric catalysis of the aldol reaction. One problem that was encountered was related to the characterization of the materials after functionalization. When using DRIFTS, a signal appeared which could be related to the Boc-group. However, the carboxylic acid and amine

functionalities could not be detected on any of the spectra after Boc-deprotection. Therefore, it is very difficult to determine whether the grafting and deprotection procedures were successful. Another possible characterization method is solid state ^{13}C NMR. This technique was attempted for 25% thiol PMOs after grafting and after deprotection (for both the thermal and UV methods), but no signals corresponding to the Boc or the proline functionalities could be discerned. The spectra are not shown here because they did not add useful information and they were measured on different batches of material than the ones discussed here. It seems that IR and NMR methods are not sufficiently sensitive to detect the incorporated functionalities amidst the organic groups already present in the PMO materials. It might be useful to repeat the functionalization methods using an excess of Boc-allyl proline in order to obtain materials with higher loadings of functional groups. This would probably be less suitable for catalysis, as the proline groups might then be too close together to perform catalysis, but a better characterization of the materials might be achieved in this way.

The original UV-functionalization method that was proposed here was not effective on the 25% thiol PMO. This method cannot be applied to the two materials that did end up showing ee (HMDS-PMO and ethane PMO), because they both contain functionalities attached by Si-O-Si bonds, which are not hydrolytically stable. The goal of synthesizing a hydrolytically stable enantioselective catalyst was therefore not achieved.

After analyzing the results obtained in this chapter, unfortunately many questions remain. It is unclear why the functionalized 25% thiol PMO materials were not active and enantioselective. We also cannot say with certainty that the proline moiety was successfully grafted onto the 25% thiol PMO. This highlights one of the downsides of functionalizing PMOs with organic groups. It can be very difficult to identify the functionalities on the material and nearly impossible to prove without a doubt the exact bonds linking the functionality to the material.

An interesting result of the study is that two of the synthesized materials did show significant ee values. The results obtained at this point are encouraging, but they are not at the level of homogeneous L-proline or results reported for other anchored proline materials. For instance, silica gel-supported proline yielded 40% of the aldol addition product in 6 hours with 63% ee.¹⁷ The catalytic results shown here can therefore be considered as preliminary results for these materials. The conversion and ee values could possibly be increased by varying the catalytic reaction conditions, such as the catalyst loading, temperature and solvents used. As for the 25% thiol PMO, further investigations could include attempts to obtain higher loadings of proline and achieve better characterization data, as mentioned above. Also, grafting of a proline moiety with a different linker could be attempted. In fact, the two materials which achieved enantioselectivity had capped silanol

groups. Therefore it is possible that an interaction between proline and the surface silanol groups is responsible for the lack of activity on the 25% thiol PMO. The use of a longer linker for instance might yield different results.

4.5 Experimental Details

Materials Following products were purchased from Aldrich and used without further purification: Thioacetic acid (96%), 2,2-Dimethoxy-2-phenylacetophenone (DMPA, 99%), poly(ethylene glycol)-block-poly(propylene glycol)-block-poly(ethylene glycol) (P123), Acetone (99.5%), CDCl_3 (99.8 atom% D), Boc-L-hydroxyproline (98%), NaH (dry, 90%), Azobisisobutyronitrile (AIBN, 98%), triethylamine (99%), 2-hydroxy-4-(2-hydroxyethoxy)-2-methylpropiophenone (Irgacure 2959, 98%), L-proline (99%), methyl 4-nitrobenzoate (99%). Propylamine (98%, Aldrich) was distilled over NaOH before use. The remaining products were purchased as follows: Allyl bromide (98%, TCI), TEOS (99%, abcr), MPTES (98%, abcr), BTEE (97%, abcr), toluene (99.85%, extra dry, Acros), DCM (99.9%, extra dry, Acros), THF (99.9%, extra dry, Acros), trifluoroacetic acid (TFA, 99%, Acros), 4-nitrobenzaldehyde (99%, Acros), ethanol (denatured, 95%, Fiers), hexane (95%, Fischer), HCl (37%, Roth), KCl (99.5%, Roth), NaOH (98%, Roth).

Synthesis of 25% thiol PMO¹⁴ The thiol PMO precursor (BTETE) was synthesized using the 100% trans ethene PMO material (see Chapter 3 for details). 80.3 mg of DMPA was dissolved in 8 ml of ethene precursor and purged with argon. 1.9 ml of thioacetic acid was added and the mixture was irradiated with UV light during 2 hours (Metalight Classic UV, 360 nm). The resulting product was treated with 8 ml of dry propylamine at 0°C. The excess propylamine was removed by rotavapor.

For the synthesis of the 25% thiol PMO, 0.84g P123, 5.36g KCl and 4.2 ml HCl (37%) were dissolved in 29.5 ml water. The mixture was stirred at 45°C overnight. 0.5 ml of BTETE and 1.5 ml of BTEE were mixed and added dropwise to the reaction mixture. After stirring at 1000 rpm at 45°C for 24 hours, the aging step was performed under static conditions at 100°C for 24 hours. The formed solid was filtered and washed with water and acetone. The PMO is refluxed three times during 6 hours in 150 ml ethanol and 4 ml HCl (37%), in order to remove the template.

Synthesis of SBA-15 2g P123 and 10 ml HCl (37%) were dissolved in 65 ml water by stirring at 45°C overnight. 4.55 ml TEOS was added and the mixture was stirred at 45°C at 1000 rpm during 5 hours. The aging step was performed under static conditions at 90°C during 18 hours. The resulting material was filtered and washed with water. The template was removed by two calcinations at 550°C (2°C/min, 6 hours).

Synthesis of ethane PMO The synthesis procedure of ethane PMO was identical to 25% thiol PMO, but using only BTEE as precursor (2 ml). The template was extracted via Soxhlet extraction with acetone.

Thiolation of SBA-15 and ethane PMO 200 mg of either solid was dried in vacuum at 120°C overnight and brought into a dry Schlenk flask under inert atmosphere. Dry toluene (10 ml) and MPTES (2 ml) were added. The reaction mixture was stirred and refluxed at 120°C overnight under inert atmosphere. The solid was filtered and washed with toluene and DCM.

Synthesis of allylated proline 2g Boc-L-hydroxyproline (**1**) was dissolved in 30 ml dry THF. 456 mg NaH was separately dissolved in 50 ml dry THF. The first solution was slowly added to the second at 0°C. The mixture was stirred at room temperature for 1 hour. 1.15 g allyl bromide was added and the mixture was stirred at 60°C during 4 hours. After cooling to room temperature, 100 ml water was added and the unreacted allyl bromide was extracted with hexane. The aqueous phase was acidified to pH 2-3 with a 2M NaHSO₄ solution and extracted with ethyl acetate. The organic phase was dried on Na₂SO₄ and the solvent was evaporated.

Grafting of proline – Thermal method¹⁸ 200 mg of 25% thiol PMO was dried overnight in vacuum at 120°C. 70 mg AIBN and 24 mg of allylated Boc-proline (**2**) were dissolved in dry toluene in a Schlenk tube under inert atmosphere. The PMO was added along with a stirring bar. Three Freeze-pump-thaw cycles were performed to degas the reaction mixture. The mixture was stirred at 90°C overnight. The solid was filtered and washed with toluene and ethanol. For the Boc-deprotection, the solid was dried at 120°C in vacuum and suspended in 10 ml dry DCM. 2 ml TFA was added and the mixture was stirred overnight. 50 ml DCM was added and the solid was filtered and washed with DCM and methanol. The solid was suspended in methanol and 0.5 ml triethylamine was added. After stirring for 5 minutes, the solid was filtered and washed with DCM and methanol, water and methanol again.

Grafting of proline – UV method 200 mg of 25% thiol PMO was dried overnight in vacuum at 120°C. Water was degassed by purging with argon for several minutes. 40 mg Irgacure 2959 and 12 mg of allylated Boc-proline (**2**) were dissolved in degassed water. The PMO was added and the mixture was sonicated in order to suspend the PMO. The mixture was irradiated with UV light overnight (Metalight Classic UV, 360 nm). The solid was filtered and washed with water, warm water and ethanol. For the Boc-deprotection, the solid was suspended in a 4M HCl solution and stirred during one hour. The solid was filtered and washed with water until washing water was at neutral pH. The solid was then suspended in a 0.01M NaOH solution for 30 minutes. The solid was filtered and washed with water until washing water was at neutral pH. The solid was suspended in water and stirred for 1 hour. The solid was filtered and washed with water and ethanol.

Catalyst Characterization FT-IR measurements were performed on a Nicolet 6700 (Thermo Scientific) with a KBr matrix, at 120°C, under vacuum. Elemental analysis was performed on a Thermo Flash 2000 Thermal Analyzer (Thermo Scientific). XRD was performed on a ARL X'TRA (Thermo Scientific). Nitrogen sorption measurements were performed on a TriStar 3000 analyzer (Micromeritics) after drying at 120° in vacuo. ¹H NMR was performed on a Bruker 300 MHz spectrometer, in CDCl₃. HAADF-STEM imaging and EDX spectroscopy experiments were performed on a FEI Titan “cubed” microscope, operated at 300 kV acceleration voltage and equipped with a large solid-angle “Super-X” EDX detector.

Catalytic procedure 2.5 mg of 4-nitrobenzaldehyde and 2.5 mg of methyl 4-nitrobenzoate (as internal standard) were added in a vial. The appropriate amount of catalyst was added, so that the nitrogen content of the catalyst corresponded to 35 mol% with respect to 4-nitrobenzaldehyde. A minimal amount of acetone was added to wet the catalyst (0.3-0.5 ml). The reaction mixture was kept at 25°C in an oil bath and stirred at 500 rpm. Samples were analyzed on a LC-20AT Shimadzu HPLC equipped with a C18 reversed phase column and a diode array detector. A gradient of acetonitrile and water containing 0.1% TFA was used. The acetonitrile concentration was increased from 30% to 62% in 7 minutes, then kept at 62% for 1 minute, decreased back to 30% in one minute and kept there for one minute. The column temperature was kept constant at 30°C. The enantiomers of the aldol product were separated by chiral HPLC (Chiralpak AS-H, Hexane:Ethanol 90:10).

4.6 References

- [1] C. Ayats, A.H. Henseler, M.A. Pericas, A Solid-Supported Organocatalyst for Continuous-Flow Enantioselective Aldol Reactions, *Chemsuschem*, 5 (2012) 320-325.
- [2] E.G. Doyaguez, G. Corrales, L. Garrido, J. Rodriguez-Hernandez, A. Gallardo, A. Fernandez-Mayoralas, Linear Copolymers of Proline Methacrylate and Styrene as Catalysts for Aldol Reactions in Water: Effect of the Copolymer Aggregation on the Enantioselectivity, *Macromolecules*, 44 (2011) 6268-6276.
- [3] L. Xu, J.J. Huang, M. Zhang, L. Yu, Y.N. Fan, Design and Preparation of Polymer Resin-Supported Proline Catalyst with Industrial Application Potential, *Chemistryselect*, 1 (2016) 1933-1937.
- [4] Z. An, W.H. Zhang, H.M. Shi, J. He, An effective heterogeneous L-proline catalyst for the asymmetric aldol reaction using anionic clays as intercalated support, *Journal of Catalysis*, 241 (2006) 319-327.
- [5] S. Calogero, D. Lanari, M. Orru, O. Piermatti, F. Pizzo, L. Vaccaro, Supported L-proline on zirconium phosphates methyl and/or phenyl phosphonates as heterogeneous organocatalysts for direct asymmetric aldol addition, *Journal of Catalysis*, 282 (2011) 112-119.
- [6] K. Arya, U.C. Rajesh, D.S. Rawat, Proline confined FAU zeolite: heterogeneous hybrid catalyst for the synthesis of spiroheterocycles via a Mannich type reaction, *Green Chemistry*, 14 (2012) 3344-3351.
- [7] E.A. Prasetyanto, S.M. Jeong, S.E. Park, Asymmetric Catalysis in Confined Space Provided by L-Proline Functionalized Mesoporous Silica with Plugs in the Pore, *Topics in Catalysis*, 53 (2010) 192-199.
- [8] E.G. Doyaguez, F. Calderon, F. Sanchez, A. Fernandez-Mayoralas, Asymmetric aldol reaction catalyzed by a heterogenized proline on a mesoporous support. The role of the nature of solvents, *Journal of Organic Chemistry*, 72 (2007) 9353-9356.
- [9] F. Calderon, R. Fernandez, F. Sanchez, A. Fernandez-Mayoralas, Asymmetric aldol reaction using immobilized proline on mesoporous support, *Advanced Synthesis & Catalysis*, 347 (2005) 1395-1403.
- [10] A. Zamboulis, N.J. Rahier, M. Gehringer, X. Cattoen, G. Niel, C. Bied, J.J.E. Moreau, M.W.C. Man, Silica-supported L-proline organocatalysts for asymmetric aldolisation, *Tetrahedron-Asymmetry*, 20 (2009) 2880-2885.
- [11] A. Massi, A. Cavazzini, L. Del Zoppo, O. Pandoli, V. Costa, L. Pasti, P.P. Giovannini, Toward the optimization of continuous-flow aldol and alpha-amination reactions by means

of proline-functionalized silicon packed-bed microreactors, *Tetrahedron Letters*, 52 (2011) 619-622.

[12] Z. An, Y. Guo, L.W. Zhao, Z. Li, J. He, L-Proline-Grafted Mesoporous Silica with Alternating Hydrophobic and Hydrophilic Blocks to Promote Direct Asymmetric Aldol and Knoevenagel-Michael Cascade Reactions, *Acs Catalysis*, 4 (2014) 2566-2576.

[13] S. Bhowmick, A. Mondal, A. Ghosh, K.C. Bhowmick, Water: the most versatile and nature's friendly media in asymmetric organocatalyzed direct aldol reactions, *Tetrahedron-Asymmetry*, 26 (2015) 1215-1244.

[14] D. Esquivel, O. van den Berg, F.J. Romero-Salguero, F. Du Prez, P. Van Der Voort, 100% thiol-functionalized ethylene PMOs prepared by "thiolacid-ene" chemistry, *Chemical Communications*, 49 (2013) 2344-2346.

[15] D. Esquivel, J. Ouwehand, M. Meledina, S. Turner, G. Van Tendeloo, F.J. Romero-Salguero, J. De Clercq, P. Van Der Voort, Thiol-ethylene bridged PMO: A high capacity regenerable mercury adsorbent via intrapore mercury thiolate crystal formation, *Journal of Hazardous Materials*, 339 (2017) 368-377.

[16] B. List, R.A. Lerner, C.F. Barbas, Proline-catalyzed direct asymmetric aldol reactions, *Journal of the American Chemical Society*, 122 (2000) 2395-2396.

[17] A.A. Elmekawy, J.B. Sweeney, D.R. Brown, Efficient synthesis of supported proline catalysts for asymmetric aldol reactions, *Catalysis Science & Technology*, 5 (2015) 690-696.

[18] O. Bortolini, L. Caciolli, A. Cavazzini, V. Costa, R. Greco, A. Massi, L. Pasti, Silica-supported 5-(pyrrolidin-2-yl)tetrazole: development of organocatalytic processes from batch to continuous-flow conditions, *Green Chemistry*, 14 (2012) 992-1000.

Part II.

Titania-functionalized frustules as photocatalyst

Chapter 5.

An introduction to titania and titania/silica composites in photocatalysis

5.1 Titania as a photocatalyst

5.1.1 The different forms of titania

Titanium dioxide, or titania, is an abundant transition metal oxide with many common applications. It is used as a white pigment and can be found in paint, sunscreen, tooth paste and food products. Titania also has many technological applications, due to its semiconductor properties. Some examples include solar cells, self-cleaning surfaces and water and air purification. Titania can occur in different forms and three main crystalline polymorphs exist, namely anatase, rutile and brookite. Their crystal structures are depicted in Figure 5.1.

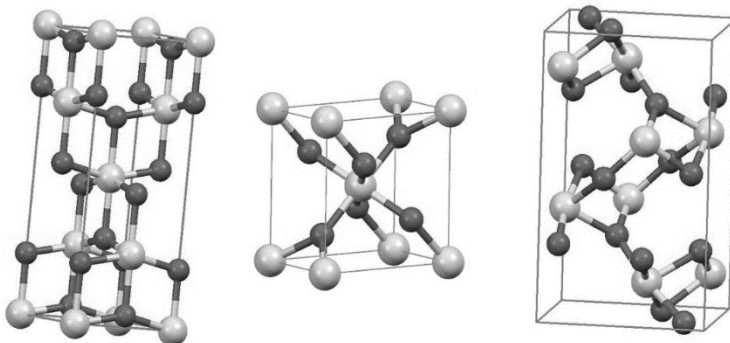


Figure 5.1. The crystal structures of three titania polymorphs: anatase, rutile and brookite (from left to right).

When synthesizing titania via sol-gel methods, usually an amorphous phase is formed initially. When increasing the temperature during calcination, anatase crystallites form initially, which then transition to rutile. The formation of anatase can start at 350°C, whereas the transformation to rutile requires a temperature of 500°C. However, these temperature values are dependent on the particle size and can shift to considerably higher temperatures for nanoparticles.¹ Brookite is very rarely obtained in this type of synthesis, as it requires very specific reaction conditions to be formed, usually involving the use of certain additives.²

5.1.2 The mechanism of photocatalysis

Solid materials can be classified as conductors, semiconductors and insulators (Figure 5.2). In conductors, such as copper, the valence band (VB) and conduction band (CB) overlap, so that electrons can be excited and travel freely through the material. In an insulator, such as glass, a large band gap exists between the VB and CB, so that the electrons cannot be excited to the conduction band. In practice, this means that a conductor can conduct electricity over a long distance, while an insulator stops the flow of electricity. In a semiconductor, such as titania, the VB and CB do not overlap, but the band gap is sufficiently small that electrons can be excited from the VB to the CB, either by thermal energy or by irradiation. This excitation forms an electron-hole pair, also called the exciton, which will recombine after a certain time.

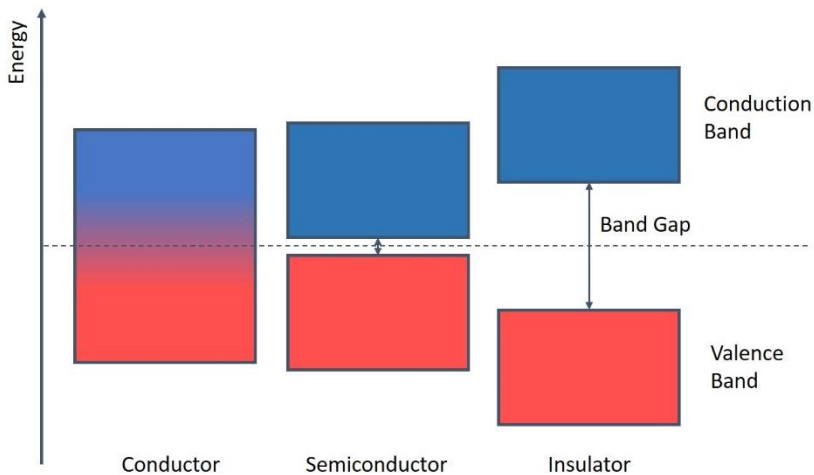
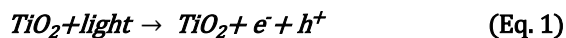


Figure 5.2. A schematic representation of a conductor, a semiconductor and an insulator.

Titania being a semiconductor, electrons (e^-) and holes (h^+) are formed upon excitation with light in the UV or visible range (Eq. 1). For this to happen, the energy of the photon must be

greater than the band gap. The wavelength of the radiation required to excite electrons across the band gap can be calculated by the formula $E = \frac{hc}{\lambda}$, where E is the band gap in eV, h is Planck's constant, c is the speed of light in vacuum and λ is the wavelength of the radiation in nm.

The electrons in the conduction band act as reductants and the holes in the valence band act as oxidants. These can undergo several reactions with molecules which are adsorbed on the outer titania surface. After the dissociation of water (Eq. 2), hydroxyl radicals can be formed from hydroxyl ions (Eq. 3). If a high amount of water is present, the formation of hydrogen peroxide can occur in the presence of oxygen (Eq. 4), which can dissociate to a hydroxyl ion and a hydroxyl radical (Eq. 5). Oxygen present in the atmosphere can also be reduced to a radical superoxide ion (Eq. 6).



The reactions above show the formation of the radical $\text{OH}\cdot$ and $\cdot\text{O}_2^-$ species, which are both strong oxidants. Due to these oxidative properties, titania lends itself to the photocatalytic decomposition of organic molecules. In water, typically dyes are used in test reactions, including methylene blue and rhodamine B. In the gas phase, the degradation of volatile organic compounds (VOCs) such as acetone, acetaldehyde or acetic acid is most often reported. As an example of the mechanism of such degradations, the photocatalytic decomposition of acetaldehyde to CO_2 proceeds via a succession of oxidation steps, with acetic acid, formaldehyde and formic acid as intermediates.³

Titania also lends itself to other applications due to these semiconductor properties.⁴ One of these is the use of titania in solar cells. Several setups have been developed that allow titania, directly or indirectly, to be photoexcited by sunlight. The resulting electron can be led to an external circuit in order to generate electricity. Another application of titania is in water splitting. Here, water is photocatalytically transformed into H_2 and O_2 via redox processes. Titania can also be used as a sensor for gases such as H_2 , CO, methanol and ethanol. The electrical resistance of titania shifts depending on the gas it comes into contact with, allowing to quantify the gas concentration.

5.1.3 Anatase versus rutile as photocatalyst

Both anatase and rutile are photocatalytically active, though it is generally considered that the anatase phase is a better photocatalyst, despite the fact that rutile can absorb light in a wider wavelength range. In fact, the band gap of anatase is 3.2 eV and that of rutile is 3.0 eV. This means that anatase can absorb light of wavelengths below 387 nm, while rutile can absorb light below 413 nm. The UVA region of light, which is contained in sunlight, ranges from 320 to 400 nm. Therefore, rutile can absorb more sunlight than anatase. Despite this, anatase is generally more active in photocatalysis, even when light in the UVA range is used. This can be explained by a difference in the diffusion distance of the electron-hole pairs in both crystal phases. Luttrell et al.⁵ performed a study to show the difference in recombination rate between anatase and rutile. They synthesized thin films of pure anatase and pure rutile crystals, with increasing film thickness and tested these in the photocatalytic degradation of methylene orange in water (Figure 5.3a). They found that for rutile films of increasing thickness, the photocatalytic activity stopped increasing significantly at a thickness of 2.5 nm. This indicates that the charge carriers cannot travel more than 2.5 nm to reach the surface of the film and contribute to the photocatalytic activity. For the anatase films, this threshold thickness was found to be 5 nm. Therefore, the increased activity of anatase can be attributed to the longer diffusion distance of the active electrons and holes, which can travel up to 5 nm through the crystal phase. It is important to note that in this

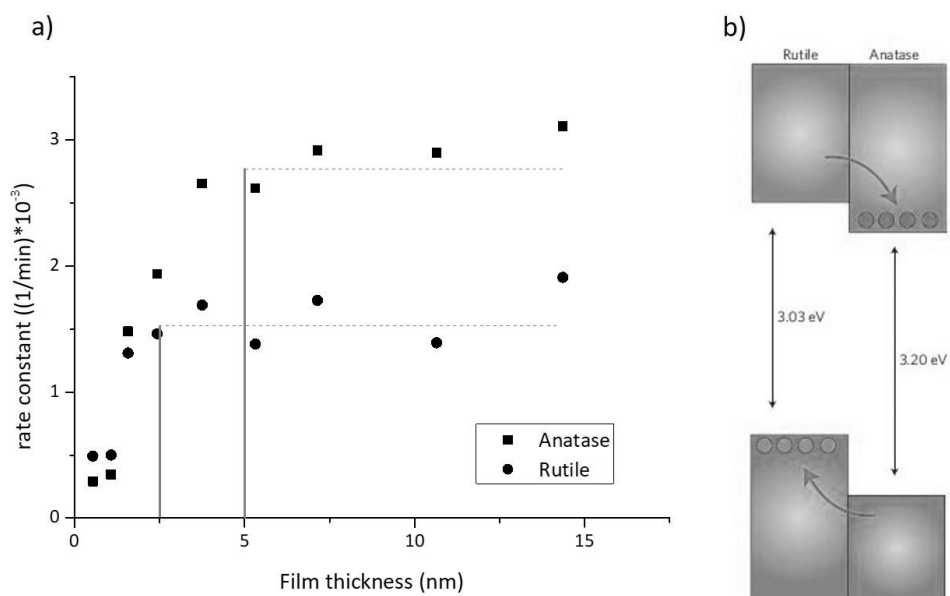


Figure 5.3. a) A simplified representation of the data obtained in the thin film study performed by Luttrell et al. The vertical lines indicate the film thickness at which the photocatalytic activity stops increasing significantly. b) The relative positions of the anatase and rutile band gaps.^{5,11}

study, UV light of 350-400 nm was used, which penetrates titania to a depth of several μm .⁶ Therefore the penetration depth of the UV light should not be a limiting factor for the photocatalytic activity and should not have an influence on the results displayed in the thin film study. The larger diffusion distance in anatase is most likely due to a combination of longer exciton life-times and higher mobilities of the charge carriers, compared to the rutile phase.

The primary benchmark material in photocatalysis is Evonik's P25, a crystalline titania powder containing approximately 80% anatase and 20% rutile.⁸ This material is manufactured by the gaseous hydrolysis of TiCl_4 at elevated temperatures. Many researchers have attributed the high activity of P25 to a synergetic effect of anatase and rutile. From a theoretical point of view, this can be explained by the fact that the VB and CB of rutile are slightly higher than those of anatase. Figure 5.3b shows the relative CB and VB positions of anatase and rutile, according to the current scientific consensus⁹⁻¹¹, based on both theoretical and experimental studies. Rutile can transfer CB electrons to the anatase CB and holes are transferred from the anatase VB to the rutile VB. This causes a physical separation of a portion of the charge carriers, which increases their life-time. However, when tested experimentally, P25 and other physical mixtures of anatase and rutile are sometimes, but not consistently, more active in photocatalytic reactions than pure anatase or pure rutile.^{8, 9, 12} For the synergetic effect between anatase and rutile to be effective, sufficient physical contact between the two phases is required,^{12, 13} which seems to be highly dependent on the reaction conditions used during the catalytic testing.

Therefore we can conclude that a titania photocatalyst should ideally contain anatase as the main crystalline phase. Possibly the presence of rutile can increase the activity, but only if in direct contact with the anatase phase. Amorphous titania is generally considered inactive for photocatalysis, so the crystallinity of the titania phase should be as high as possible. Since the charge carriers cannot travel more than 5 nm through crystalline anatase, the ideal titania photocatalyst should consist of nanoparticles or thin films, providing a high surface area and low bulk volume. Some of these requirements can be accommodated to by depositing titania nanoparticles onto a support material, such as silica.

5.2 Titania/silica composites as photocatalysts

5.2.1 The role of silica in composite materials

The synthesis of titania/silica composites is a very popular research topic because the titania particles in such composites are often more active than pure titania synthesized under similar conditions. Silica has several effects in these composites, namely the stabilization of the titania nanoparticles and a possible enhancement of the photocatalytic activity via adsorption and diffusion of the organic compound. These two effects are discussed in more detail hereafter.

Firstly, on a titania/silica composite, the silica phase can stabilize the titania nanoparticles by preventing their aggregation during the crystallization process.^{14, 15} Therefore, titania nanoparticles in composites are usually smaller and, due to the resulting increase in surface area and decrease in bulk volume, more active. Additionally, the titania in composites is more thermally stable than pure titania. This could be due to the reduced particle size, as the transition temperatures of amorphous titania to anatase and of anatase to rutile are both inversely proportional to the particle size.¹ Moreover, the spatial separation of titania, which prevents the sintering and aggregation of the particles could also inhibit the crystallization process. The higher transition temperature of anatase to rutile allows the synthesis of anatase at higher temperatures, which improves the degree of crystallinity and thus the photocatalytic activity.¹⁴

Besides the stabilization of the titania particles, the silica phase in $\text{TiO}_2/\text{SiO}_2$ composites can also play an active part in improving the photocatalytic activity. This effect is described as the 'adsorb and shuttle' mechanism in the literature.⁶ It implies that a pollutant can adsorb onto the silica surface in close proximity to a titania particle and then reach the active site via diffusion, as illustrated in Figure 5.4. Obviously, the active radicals formed by the charge carriers (eq 1-6) could also diffuse from the titania phase to the silica surface and thereby contribute to the photocatalytic reaction. However, it was shown that these active radicals can only diffuse over a distance of $20\ \mu\text{m}$,¹⁶ whereas organics adsorbed on the silica surface can diffuse over several cm.¹⁷ Therefore, the main effect of the increased surface area of the composite is an increased adsorption of the pollutant and, after diffusion to the titania sites, this leads to increased photocatalytic degradation. This phenomenon has been reported by several research groups, both for pollutants in the gas phase and in aqueous solutions.

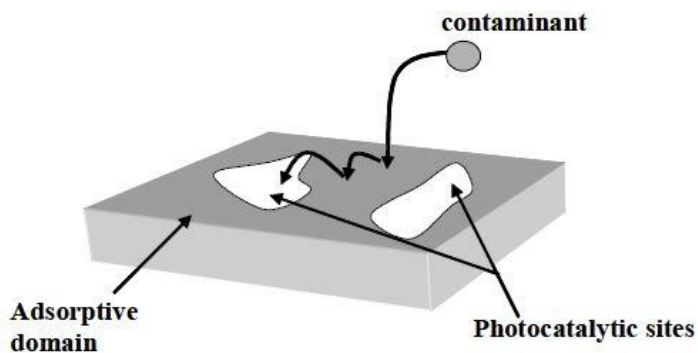


Figure 5.4. A schematic representation of the 'adsorb and shuttle' mechanism.⁶

Takeda et al.¹⁸ investigated the photocatalytic degradation of gaseous propionaldehyde with titania supported on thin films made of different materials, such as zeolites, silica, alumina and activated carbon. They found that the amount of propionaldehyde adsorbed by the thin films was not related to the surface area of the films, but more so to the affinity

of each material for the pollutant. They then correlated the adsorption coefficient of each material to the rate coefficient of the photodegradation of propionaldehyde and found that an intermediate affinity of the substrate for the pollutant gave optimal results. They rationalized that at low adsorption affinity, only a small amount of pollutant is adsorbed onto the substrate and this amount limits the reaction rate. At too high affinity, the mobility of the adsorbed pollutant is reduced and therefore the photocatalytic degradation of the adsorbed pollutant is inhibited.

The same researchers¹⁷ also studied the diffusion of propionaldehyde along a TiO₂/zeolite film, by illuminating only a small strip of the film, so that 90% of the film remained in the dark. They showed that under these conditions, the gaseous propionaldehyde could be fully decomposed, which indicated that the pollutant was able to diffuse along the length of the film (which was 4 cm), from the dark part of the film to the illuminated strip on the edge of the film. They were able to fit the diffusion of propionaldehyde to a one-dimensional diffusion model.

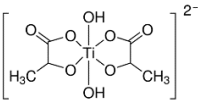
5.2.2 Synthesis methods of titania/silica composites

A wide variety of synthetic methods have been used to obtain titania/silica composites. The resulting materials vary in Ti/Si ratio, specific surface area, crystallite properties of the titania phase, etc. In addition, various photocatalytic reactions are commonly used to test the activity of the reported materials, including the aqueous decomposition of various dyes or other organic compounds and the gaseous decomposition of various VOCs and other pollutants. This makes it extremely difficult to compare the performances of materials reported by different research groups. However, it is interesting to give an overview of the synthetic pathways investigated in this field.

5.2.2.1 The sol-gel synthesis method

Table 5.1 gives an overview of the most common silica and titania precursors, along with their abbreviations. The most common way to synthesize titania/silica composites is via sol-gel synthesis. In this approach, a silica source (typically TEOS) and a titania source (typically TTIP or TBOT) are separately dissolved in an organic solvent. Then, acidified water is added to catalyze the hydrolysis and condensation of the precursors with the formation of a silica sol and a titania sol. Then, the sols are mixed and heated to form a gel. The gel is then dried and calcined to obtain a mixed oxide.^{14, 19, 20} These materials consist of a crystalline titania phase and an amorphous silica phase and can reach high surface areas of several hundred m²/g. Figure 5.5 shows a 3D reconstruction of the morphology of such a sol-gel composite, based on electron tomography measurements.²¹

Table 5.1. Chemical formulas, names and abbreviations of the most commonly used silica and titania precursors in sol-gel synthesis

Si(OEt) ₄	Tetraethyl orthosilicate	TEOS
Ti(OiPr) ₄	Titanium (IV) isopropoxide	TTIP
Ti(Obu) ₄	Tetrabutyl orthotitanate	TBOT
TiCl ₄	Titanium chloride	-
TiOSO ₄	Titanium oxysulphate/Titanyl sulphate	-
2NH_4^+ 	Titanium (IV) bis (ammonium lactato) dihydroxide	TIBALDH

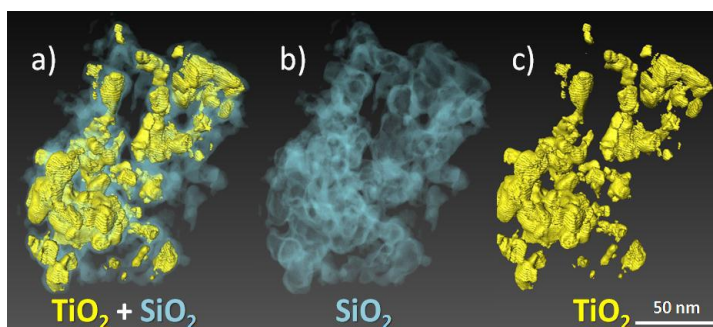


Figure 5.5. A 3D reconstruction of a titania/silica composite obtained via sol-gel synthesis (a) and the two phases of the composite material represented separately (b and c).²¹

The sol-gel method is straightforward in its execution and it usually involves relatively cheap and benign solvents, such as ethanol or isopropanol. However, many different parameters play a role in this type of synthesis, such as the chosen precursors, their concentrations, the solvents used and the pH of the solution. Therefore, while one specific set of conditions may give reproducible results, the influence of changing one of the parameters on the end product is very unpredictable.

5.2.2.2 Post-functionalization of pre-formed porous silicas

In a different approach, titania can be grafted onto a pre-existing amorphous silica material. This method provides a better control over the morphological properties of the silica, because it is synthesized separately. The functionalization can be achieved via different processes. Several ordered mesoporous silicas have been functionalized with titania, the most common ones being MCM-41 and SBA-15. One method is to directly deposit pre-formed titania nanoparticles onto the mesoporous silica.^{22, 23} Another possibility is impregnation, where the titania precursor is dissolved in a dry solvent and added to the porous silica source, followed by filtration.²⁴⁻²⁹ The Ti-precursor then binds to the surface silanol groups but, due to the absence of water, cannot further hydrolyse. Therefore, only

a single layer of titania can be deposited on the silica by this method. It generally uses more expensive and harmful solvents, such as toluene or hexane.

No doubt the most popular functionalization method of pre-formed silica consists of a modified sol-gel synthesis, where a titania precursor is dissolved in an organic solvent and hydrolyzed by adding water or an acid solution. The pre-formed silica source is then added to the titania sol and the solvent is either evaporated or separated via filtration or centrifugation.³⁰⁻³⁹ This method offers the same advantages as the sol-gel method using Si and Ti precursors, namely that it's cheaper, more benign and it offers many possibilities by varying the reaction parameters. However, with a pre-formed silica material, the morphology of the silica is very well controlled. Additionally, some of the many reaction parameters of the classical sol-gel synthesis are removed. For instance, a big difference in condensation speed of the Si and Ti precursors need no longer be a problem, because now only the Ti precursor is condensed.

Additionally, other methods for titania functionalization using specialized equipment exist. Chemical vapor deposition (CVD) can be used to cover a silica material with a titania film. In particular, atomic layer deposition (ALD) allows to do this in a very controlled manner. In this type of synthesis, the silica is exposed to a vapor of a titania precursor such as TTIP. This precursor reacts with the surface silanols to chemically bond onto the silica surface (via Si-O-Ti bonds), forming a monolayer which fully covers the silica surface. Then, the material is exposed to water vapor, which hydrolyses the bonded TTIP. Pulses of TTIP and water vapor are alternated to grow a titania film, layer by layer, onto the silica surface. This process is followed by calcination to obtain the anatase phase.⁴⁰ While this method provides a great control over the thickness of the deposited film, it has several practical drawbacks such as its high cost and long reaction time. Physical vapor deposition (PVD), such as sputtering, is another technique to synthesize titania coatings. In this case, a titanium electrode is bombarded with a sputtering gas, which releases Ti atoms. In the presence of oxygen, TiO₂ is formed and deposited onto the target substrate.⁴¹

5.3 Diatom frustules as silica source

5.3.1 An introduction to diatom frustules

Diatoms are single-celled algae which produce intricate amorphous silica structures as a protective shell.⁴² These so-called frustules consist of well-defined silica structures, unique to each species. Diatoms and their frustules contain symmetry and fractal patterns in a wide variety of extraordinary shapes and patterns (Figure 5.6). With an estimated 200.000 different diatom species⁴³ containing frustules with pore sizes ranging from 3 to several hundred nm,⁴⁴⁻⁴⁶ and specific surface areas ranging from below 10 m²/g to above 150 m²/g,⁴⁷ the diatom population represents a huge and diverse database of porous silicas. The

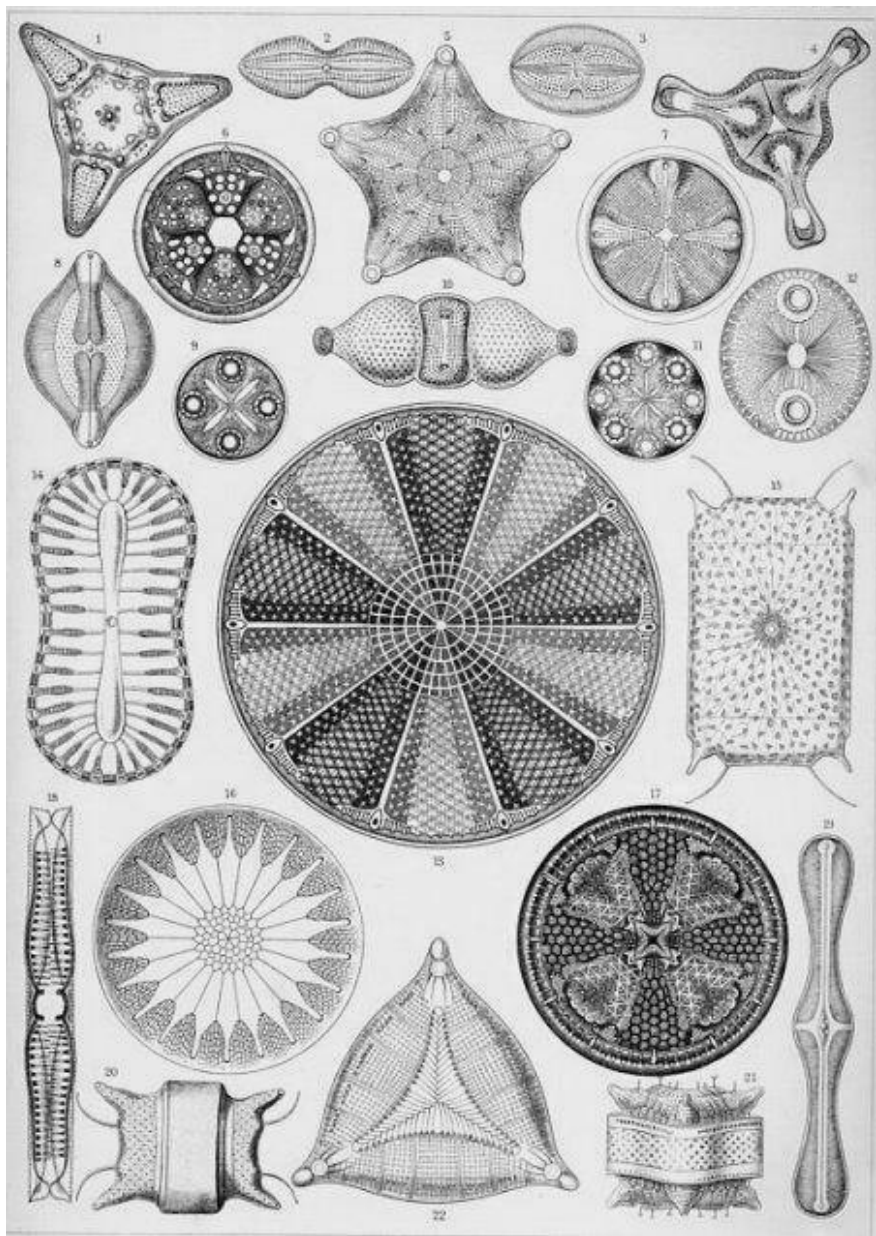


Figure 5.6. A collection of diatoms, reproduced from Ernst Haeckel's 'Kunstformen der Natur', 1904.

large scale production of diatoms is expected to increase in the coming years, in view of their potential in the production of biofuels.⁴⁸ In fact, as global fossil fuel reserves are rapidly being depleted, research towards the production of these alternative fuels from renewable sources has become very important in recent years. Diatoms contain 15 to 80 percent (by weight of dry biomass) of oil,⁴⁹ depending on the species, which makes them a viable competitor for crops as a biofuel source. Like plants, diatoms metabolize carbon via photosynthesis, which makes the process of harvesting and burning the biofuel CO₂-neutral. They also present certain practical advantages, such as a high growth rate and the very little space required to grow them. Therefore, frustules are expected to be an important side product of the biofuel production process.⁵⁰

Furthermore, diatom frustules present certain structural differences compared to commercial or synthetic porous silica sources. While commercial silica gel has a high specific surface area, its pores are not well defined as they are formed randomly in the production process.⁵¹ Uniform pore size distributions can be obtained in synthetic silicas, such as zeolites or MCM and SBA-type mesoporous materials. However, in these cases, the pore sizes and morphologies which can be obtained are limited. Diatom frustules on the other hand are biologically synthesized by the organism, resulting in well-defined structures. While many different diatom species exist with a wide variety of pore sizes and shapes, the morphology of the frustules is uniform for each species.^{44, 45} They combine the advantages of a wide scope of pore morphologies with a well-defined pore structure. Not surprisingly then, diatom frustules have been investigated in several technological applications.

5.3.2 Technological applications of diatom frustules

Diatom frustules were found to be non-toxic⁵² and are therefore worth investigating for drug release. Several different drugs were loaded on frustules and the release behavior was studied. Interestingly, a two-step release pattern is observed in most cases. The drugs loaded on the outside surface of the frustule are released within 6 hours, while the drugs adsorbed to the inside of the frustule are released more slowly, over the course of two weeks.^{53, 54} In some cases, the frustules were functionalized with acidic or basic functional groups, to improve the interaction with the drugs and tune the release profiles.^{55, 56}

Frustules were also used as a hard template to form porous carbon materials.⁵⁷⁻⁵⁹ A carbon source such as furfuryl alcohol or sucrose was polymerized inside the frustule pores and calcined. Then, the frustules were etched out, resulting in a carbon with the inverted morphology of the frustule. The resulting materials can reach BET surface areas of over 300 m²/g and have potential applications in adsorption. This is illustrated in Figure 5.7. Similar templating strategies have also been applied to form metal structures, resulting in uniquely shaped silver⁶⁰ and gold⁶¹ materials.

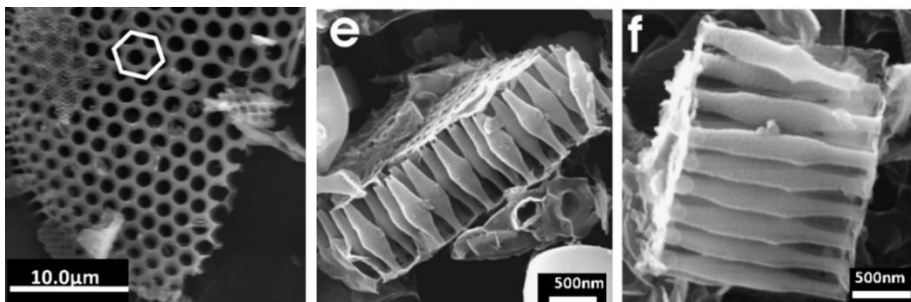


Figure 5.7 SEM images of a diatom frustule (left) and the inversed carbon structure (middle and right).⁶⁵

Frustules have also been used in gas sensing applications. Bao et al.⁶² converted the silica frustule to silicon, while keeping the morphology intact, using a magnesium-mediated reduction process. Weatherspoon et al.⁶³ covered the frustules in a continuous layer of SnO₂. These conductive frustule-based materials were used to make a NO gas sensor, based on the difference in conductivity of the material in the presence of the gas.

The relatively high surface area and unique pore structure of diatoms also makes them interesting as carrier material for titania nanoparticles. The use of titania/diatom composites in photocatalysis is discussed in the following section.

5.3.3 Diatom frustules in titania/silica composites

Apart from synthetic silicas, frustules of different diatom species were also functionalized with titania using sol-gel or impregnation methods. Different precursors were used, such as TBOT⁶⁴, TiCl₄⁶⁵, TTIP⁶⁶ and TiOSO₄⁶⁷, and after calcination, the obtained materials were successfully applied in aqueous dye degradation. In a slightly different approach, He et al.⁶⁸ functionalized *Cocconeis placentula* frustules with TTIP, without fully removing the organic matter of the frustules beforehand. After calcination, this resulted in a carbon-doped anatase phase, which was active in the aqueous degradation of rhodamine B. Zhang et al.⁶⁹ used *Coscinodiscus* frustules as a hard template. After coating with TBOT and calcination, the silica was removed by a basic treatment, leaving a titania shell in the shape of the frustule.

Few of these titania-functionalized frustules were applied in photocatalytic air purification, but mostly in the aqueous degradation of dyes. Van Eynde et al.⁷⁰ functionalized *Pinnularia* frustules by sol-gel deposition of TTIP, followed by calcination. The resulting titania-coated frustules were successfully applied in the photodegradation of NO gas.

Another interesting line of research is the biogenic incorporation of titania in diatom frustules. In this approach, a Ti source is added to the cultivation medium and the diatoms

biogenically incorporate titania into the frustule. Lang et al.⁷¹ incorporated titania into *Thalassiosira weissflogii* frustules by adding TiBALDH to the cultivation medium, reaching a Ti:Si ratio of 0.34:1. However, this material was not tested for its photocatalytic activity. Van Eynde et al.⁷² tested several Ti sources and obtained an incorporation of up to 10 wt% Ti in *Pinnularia* frustules. After calcination, some of the obtained materials showed photocatalytic activity in the degradation of gaseous acetaldehyde.

Besides diatoms, other organisms are worth considering for the renewable sourcing of silica. Typically, plants which are rigid and mechanically strong have a high silica content. Several of these plants have been investigated for the extraction of silica and its subsequent functionalization with titania. Examples include corn plants,⁷³ several aquatic plants⁷⁴ and rice husk.^{75, 76} The silica extracted from plants had surface areas between 100 and 235 m²/g, while rice husk has surface areas as high as 680 m²/g. The resulting functionalized materials were all successful in the photocatalytic degradation of dyes in water.

5.4 References

- [1] O. Khatim, M. Amamra, K. Chhor, A.M.T. Bell, D. Novikov, D. Vrel, A. Kanaev, Amorphous-anatase phase transition in single immobilized TiO₂ nanoparticles, *Chemical Physics Letters*, 558 (2013) 53-56.
- [2] A. Di Paola, M. Bellardita, L. Palmisano, Brookite, the Least Known TiO₂ Photocatalyst, *Catalysts*, 3 (2013) 36-73.
- [3] B. Hauchecorne, D. Terrens, S. Verbruggen, J.A. Martens, H. Van Langenhove, K. Demeestere, S. Lenaerts, Elucidating the photocatalytic degradation pathway of acetaldehyde: An FTIR in situ study under atmospheric conditions, *Applied Catalysis B-Environmental*, 106 (2011) 630-638.
- [4] X. Chen, S.S. Mao, Titanium dioxide nanomaterials: Synthesis, properties, modifications, and applications, *Chemical Reviews*, 107 (2007) 2891-2959.
- [5] T. Luttrell, S. Halpegamage, J.G. Tao, A. Kramer, E. Sutter, M. Batzill, Why is anatase a better photocatalyst than rutile? - Model studies on epitaxial TiO₂ films, *Scientific Reports*, 4 (2014) 4043.
- [6] Y. Paz, Composite Titanium Dioxide Photocatalysts and the "Adsorb & Shuttle" Approach: A Review, *Solid State Phenomena*, 162 (2010) 135-162.
- [7] E. Carbonell, F. Ramiro-Manzano, I. Rodriguez, A. Corma, F. Meseguer, H. Garcia, Enhancement of TiO₂ photocatalytic activity by structuring the photocatalyst film as photonic sponge, *Photochemical & Photobiological Sciences*, 7 (2008) 931-935.
- [8] B. Ohtani, O.O. Prieto-Mahaney, D. Li, R. Abe, What is Degussa (Evonik) P25? Crystalline composition analysis, reconstruction from isolated pure particles and photocatalytic activity test, *Journal of Photochemistry and Photobiology a-Chemistry*, 216 (2010) 179-182.
- [9] R. Quesada-Cabrera, C. Sotelo-Vazquez, J.C. Bear, J.A. Darr, I.P. Parkin, Photocatalytic Evidence of the Rutile-to-Anatase Electron Transfer in Titania, *Advanced Materials Interfaces*, 1 (2014) 1400069.
- [10] D.O. Scanlon, C.W. Dunnill, J. Buckeridge, S.A. Shevlin, A.J. Logsdail, S.M. Woodley, C.R.A. Catlow, M.J. Powell, R.G. Palgrave, I.P. Parkin, G.W. Watson, T.W. Keal, P. Sherwood, A. Walsh, A.A. Sokol, Band alignment of rutile and anatase TiO₂, *Nature Materials*, 12 (2013) 798-801.
- [11] Y. Nosaka, A.Y. Nosaka, Reconsideration of Intrinsic Band Alignments within Anatase and Rutile TiO₂, *Journal of Physical Chemistry Letters*, 7 (2016) 431-434.

- [12] T. Ohno, K. Sarukawa, K. Tokieda, M. Matsumura, Morphology of a TiO₂ photocatalyst (Degussa, P-25) consisting of anatase and rutile crystalline phases, *Journal of Catalysis*, 203 (2001) 82-86.
- [13] T. Ohno, T. Tsubota, R. Inaba, Photocatalytic partial oxidation of methylpyridine isomers on TiO₂ particles under an anaerobic condition, *Journal of Applied Electrochemistry*, 35 (2005) 783-791.
- [14] K.Y. Jung, S.B. Park, Enhanced photoactivity of silica-embedded titania particles prepared by sol-gel process for the decomposition of trichloroethylene, *Applied Catalysis B-Environmental*, 25 (2000) 249-256.
- [15] A. Hanprasopwattana, T. Rieker, A.G. Sault, A.K. Datye, Morphology of titania coatings on silica gel, *Catalysis Letters*, 45 (1997) 165-175.
- [16] H. Haick, Y. Paz, Remote photocatalytic activity as probed by measuring the degradation of self-assembled monolayers anchored near microdomains of titanium dioxide, *Journal of Physical Chemistry B*, 105 (2001) 3045-3051.
- [17] N. Takeda, M. Ohtani, T. Torimoto, S. Kuwabata, H. Yoneyama, Evaluation of diffusibility of adsorbed propionaldehyde on titanium dioxide-loaded adsorbent photocatalyst films from its photodecomposition rate, *Journal of Physical Chemistry B*, 101 (1997) 2644-2649.
- [18] N. Takeda, T. Torimoto, S. Sampath, S. Kuwabata, H. Yoneyama, EFFECT OF INERT SUPPORTS FOR TITANIUM-DIOXIDE LOADING ON ENHANCEMENT OF PHOTODECOMPOSITION RATE OF GASEOUS PROPIONALDEHYDE, *Journal of Physical Chemistry*, 99 (1995) 9986-9991.
- [19] B. Llano, M.C. Hidalgo, L.A. Rios, J.A. Navio, Effect of the type of acid used in the synthesis of titania-silica mixed oxides on their photocatalytic properties, *Applied Catalysis B-Environmental*, 150 (2014) 389-395.
- [20] X.T. Gao, I.E. Wachs, Titania-silica as catalysts: molecular structural characteristics and physico-chemical properties, *Catalysis Today*, 51 (1999) 233-254.
- [21] L. Pinho, J.C. Hernandez-Garrido, J.J. Calvino, M.J. Mosquera, 2D and 3D characterization of a surfactant-synthesized TiO₂-SiO₂ mesoporous photocatalyst obtained at ambient temperature, *Physical Chemistry Chemical Physics*, 15 (2013) 2800-2808.
- [22] S. Artkla, W. Kim, W. Choi, J. Wittayakun, Highly enhanced photocatalytic degradation of tetramethylammonium on the hybrid catalyst of titania and MCM-41 obtained from rice husk silica, *Applied Catalysis B-Environmental*, 91 (2009) 157-164.

- [23] M.V.P. Sharma, V.D. Kumari, M. Subrahmanyam, TiO₂ Supported over SBA-15: An efficient photocatalyst for the pesticide degradation using solar light, *Chemosphere*, 73 (2008) 1562-1569.
- [24] M. Signoretto, E. Ghedini, V. Trevisan, C.L. Bianchi, M. Ongaro, G. Cruciani, TiO₂-MCM-41 for the photocatalytic abatement of NO_x in gas phase, *Applied Catalysis B*, 95 (2010) 130-136.
- [25] W.Y. Jung, B.H. Noh, S.H. Baek, G.D. Lee, S.S. Park, S.S. Hong, Photocatalytic decomposition of orange II over TiO₂-loaded on SBA-15 prepared using a microwave process, *Reaction Kinetics and Catalysis Letters*, 91 (2007) 223-231.
- [26] W. Wang, M. Song, Photocatalytic activity of titania-containing mesoporous SBA-15 silica, *Microporous and Mesoporous Materials*, 96 (2006) 255-261.
- [27] M. Besancon, L. Michelin, L. Josien, L. Vidal, K. Assaker, M. Bonne, B. Lebeau, J.L. Blin, Influence of the porous texture of SBA-15 mesoporous silica on the anatase formation in TiO₂-SiO₂ nanocomposites, *New Journal of Chemistry*, 40 (2016) 4386-4397.
- [28] F.X. Zhang, X. Carrier, J.M. Krafft, Y. Yoshimura, J. Blanchard, Insight into the structure and localization of the titania overlayer in TiO₂-coated SBA-15 materials, *New Journal of Chemistry*, 34 (2010) 508-516.
- [29] Y.J. Li, N. Li, J.C. Tu, X.T. Li, B.B. Wang, Y. Chi, D.R. Liu, D.F. Yang, TiO₂ supported on rod-like mesoporous silica SBA-15: Preparation, characterization and photocatalytic behaviour, *Materials Research Bulletin*, 46 (2011) 2317-2322.
- [30] M.A. Hassan, S.K. Mohamed, A.A. Ibrahim, M.A. Betiha, E.A. El-Sharkawy, A.A. Mousa, A comparative study of the incorporation of TiO₂ into MCM-41 nanostructure via different approaches and its effect on the photocatalytic degradation of methylene blue and CO oxidation, *Reaction Kinetics Mechanisms and Catalysis*, 120 (2017) 791-807.
- [31] L.H. Tian, H.T. Liu, Y. Gao, Degradation and adsorption of rhodamine B and phenol on TiO₂/MCM-41, *Kinetics and Catalysis*, 53 (2012) 554-559.
- [32] A.M. Busuioc, V. Meynen, E. Beyers, P. Cool, N. Bilba, E.F. Vansant, Growth of anatase nanoparticles inside the mesopores of SBA-15 for photocatalytic applications, *Catalysis Communications*, 8 (2007) 527-530.
- [33] A.M. Busuioc, V. Meynen, E. Beyers, M. Mertens, P. Cool, N. Bilba, E.F. Vansant, Structural features and photocatalytic behaviour of titania deposited within the pores of SBA-15, *Applied Catalysis a-General*, 312 (2006) 153-164.

[34] A. Orlov, Q.Z. Zhai, J. Klinowski, Photocatalytic properties of the SBA-15 mesoporous silica molecular sieve modified with titanium, *Journal of Materials Science*, 41 (2006) 2187-2193.

[35] J. Yang, J. Zhang, L.W. Zhu, S.Y. Chen, Y.M. Zhang, Y. Tang, Y.L. Zhu, Y.W. Li, Synthesis of nano titania particles embedded in mesoporous SBA-15: Characterization and photocatalytic activity, *Journal of Hazardous materials*, 137 (2006) 952-958.

[36] K. De Witte, P. Cool, I. De Witte, L. Ruys, J. Rao, G. Van Tendeloo, E.F. Vansant, Multistep loading of titania nanoparticles in the mesopores of SBA-15 for enhanced photocatalytic activity, *Journal of Nanoscience and Nanotechnology*, 7 (2007) 2511-2515.

[37] C. Liu, X. Lin, Y.J. Li, P. Xu, M. Li, F.T. Chen, Enhanced photocatalytic performance of mesoporous TiO₂ coated SBA-15 nanocomposites fabricated through a novel approach: supercritical deposition aided by liquid-crystal template, *Materials Research Bulletin*, 75 (2016) 25-34.

[38] Y.J. Acosta-Silva, R. Nava, V. Hernandez-Morales, S.A. Macias-Sanchez, M.L. Gomez-Herrera, B. Pawelec, Methylene blue photodegradation over titania-decorated SBA-15, *Applied Catalysis B*, 110 (2011) 108-117.

[39] D.R. Sahu, L.Y. Hong, S.C. Wang, J.L. Huang, Synthesis, analysis and characterization of ordered mesoporous TiO₂/SBA-15 matrix: Effect of calcination temperature, *Microporous and Mesoporous Materials*, 117 (2009) 640-649.

[40] P.A. Williams, C.P. Ireland, P.J. King, P.A. Chater, P. Boldrin, R.G. Palgrave, J.B. Claridge, J.R. Darwent, P.R. Chalker, M.J. Rosseinsky, Atomic layer deposition of anatase TiO₂ coating on silica particles: growth, characterization and evaluation as photocatalysts for methyl orange degradation and hydrogen production, *Journal of Materials Chemistry*, 22 (2012) 20203-20209.

[41] A. Farooq, A. Shukur, C. Astley, L. Tosheva, P. Kelly, D. Whitehead, M. Azzawi, Titania coating of mesoporous silica nanoparticles for improved biocompatibility and drug release within blood vessels, *Acta Biomaterialia*, 76 (2018) 208-216.

[42] C.E. Hamm, R. Merkel, O. Springer, P. Jurkojc, C. Maier, K. Prechtel, V. Smetacek, Architecture and material properties of diatom shells provide effective mechanical protection, *Nature*, 421 (2003) 841-843.

[43] D.G. Mann, S.J.M. Droop, Biodiversity, biogeography and conservation of diatoms, *Hydrobiologia*, 336 (1996) 19-32.

[44] E.G. Vrieling, T.P.M. Beelen, R.A. van Santen, W.W.C. Gieskes, Nanoscale uniformity of pore architecture in diatomaceous silica: A combined small and wide angle X-ray scattering study, *Journal of Phycology*, 36 (2000) 146-159.

- [45] E.G. Vrieling, T.P.M. Beelen, Q.Y. Sun, S. Hazelaar, R.A. van Santen, W.W.C. Gieskes, Ultrasmall, small, and wide angle X-ray scattering analysis of diatom biosilica: interspecific differences in fractal properties, *Journal of Materials Chemistry*, 14 (2004) 1970-1975.
- [46] D.Y. Zhang, Y. Wang, W.Q. Zhang, J.F. Pan, J. Cai, Enlargement of diatom frustules pores by hydrofluoric acid etching at room temperature, *Journal of Materials Science*, 46 (2011) 5665-5671.
- [47] A. Gelabert, O.S. Pokrovsky, J. Schott, A. Boudou, A. Feurtet-Mazel, J. Mielczarski, E. Mielczarski, N. Mesmer-Dudons, O. Spalla, Study of diatoms/aqueous solution interface. I. Acid-base equilibria and spectroscopic observation of freshwater and marine species, *Geochimica et Cosmochimica Acta*, 68 (2004) 4039-4058.
- [48] T.V. Ramachandra, D.M. Mahapatra, B. Karthick, R. Gordon, Milking Diatoms for Sustainable Energy: Biochemical Engineering versus Gasoline-Secreting Diatom Solar Panels, *Industrial and Engineering Chemistry Research*, 48 (2009) 8769-8788.
- [49] Y. Chisti, Biodiesel from microalgae, *Biotechnology Advances*, 25 (2007) 294-306.
- [50] M. Hildebrand, A.K. Davis, S.R. Smith, J.C. Traller, R. Abbriano, The place of diatoms in the biofuels industry, *Biofuels*, 3 (2012) 221-240.
- [51] R.K. Iler, *The Chemistry of Silica: Solubility, Polymerization, Colloid and Surface Properties and Biochemistry*, Wiley, 1979.
- [52] H. Zhang, M.A. Shahbazi, E.M. Makila, T.H. da Silva, R.L. Reis, J.J. Salonen, J.T. Hirvonen, H.A. Santos, Diatom silica microparticles for sustained release and permeation enhancement following oral delivery of prednisone and mesalamine, *Biomaterials*, 34 (2013) 9210-9219.
- [53] M.S. Aw, S. Simovic, J. Addai-Mensah, D. Losic, Silica microcapsules from diatoms as new carrier for delivery of therapeutics, *Nanomedicine*, 6 (2011) 1159-1173.
- [54] M.S. Aw, S. Simovic, Y. Yu, J. Addai-Mensah, D. Losic, Porous silica microshells from diatoms as biocarrier for drug delivery applications, *Powder Technology*, 223 (2012) 52-58.
- [55] M.S. Aw, M. Bariana, Y. Yu, J. Addai-Mensah, D. Losic, Surface-functionalized diatom microcapsules for drug delivery of water-insoluble drugs, *Journal of Biomaterials Applications*, 28 (2013) 163-174.
- [56] M. Bariana, M.S. Aw, M. Kurkuri, D. Losic, Tuning drug loading and release properties of diatom silica microparticles by surface modifications, *International Journal of Pharmaceutics*, 443 (2013) 230-241.

- [57] S.M. Holmes, B.E. Graniel-Garcia, P. Foran, P. Hill, E.P.L. Roberts, B.H. Sakakini, J.M. Newton, A novel porous carbon based on diatomaceous earth, *Chemical Communications*, (2006) 2662-2663.
- [58] M. Perez-Cabero, V. Puchol, D. Beltran, P. Amoros, Thalassiosira pseudonana diatom as biotemplate to produce a macroporous ordered carbon-rich material, *Carbon*, 46 (2008) 297-304.
- [59] D. Liu, P. Yuan, D.Y. Tan, H.M. Liu, T. Wang, M.D. Fan, J.X. Zhu, H.P. He, Facile preparation of hierarchically porous carbon using diatomite as both template and catalyst and methylene blue adsorption of carbon products, *Journal of Colloid and Interface Science*, 388 (2012) 176-184.
- [60] E.K. Payne, N.L. Rosi, C. Xue, C.A. Mirkin, Sacrificial biological templates for the formation of nanostructured metallic microshells, *Angewandte Chemie-International Edition*, 44 (2005) 5064-5067.
- [61] D. Losic, J.G. Mitchell, N.H. Voelcker, Fabrication of gold nanostructures by templating from porous diatom frustules, *New Journal of Chemistry*, 30 (2006) 908-914.
- [62] Z.H. Bao, M.R. Weatherspoon, S. Shian, Y. Cai, P.D. Graham, S.M. Allan, G. Ahmad, M.B. Dickerson, B.C. Church, Z.T. Kang, H.W. Abernathy, C.J. Summers, M.L. Liu, K.H. Sandhage, Chemical reduction of three-dimensional silica micro-assemblies into microporous silicon replicas, *Nature*, 446 (2007) 172-175.
- [63] M.R. Weatherspoon, M.B. Dickerson, G. Wang, Y. Cai, S. Shian, S.C. Jones, S.R. Marder, K.H. Sandhage, Thin, conformal, and continuous SnO₂ coatings on three-dimensional biosilica templates through hydroxy-group amplification and layer-by-layer alkoxide deposition, *Angewandte Chemie-International Edition*, 46 (2007) 5724-5727.
- [64] B. Wang, F.C. de Godoi, Z.M. Sun, Q.C. Zeng, S.L. Zheng, R.L. Frost, Synthesis, characterization and activity of an immobilized photocatalyst: Natural porous diatomite supported titania nanoparticles, *Journal of Colloid and Interface Science*, 438 (2015) 204-211.
- [65] L. Mao, J. Liu, S.M. Zhu, D. Zhang, Z.X. Chen, C.X. Chen, Sonochemical fabrication of mesoporous TiO₂ inside diatom frustules for photocatalyst, *Ultrasonics Sonochemistry*, 21 (2014) 527-534.
- [66] L. Chetia, D. Kalita, G.A. Ahmed, Enhanced photocatalytic degradation by diatom templated mixed phase titania nanostructure, *Journal of Photochemistry and Photobiology a-Chemistry*, 338 (2017) 134-145.

- [67] S.K. Padmanabhan, S. Pal, E.U. Haq, A. Licciulli, Nanocrystalline TiO₂-diatomite composite catalysts: Effect of crystallization on the photocatalytic degradation of rhodamine B, *Applied Catalysis A*, 485 (2014) 157-162.
- [68] J. He, D.M. Chen, Y.L. Li, J.L. Shao, J. Xie, Y.J. Sun, Z.Y. Yan, J.Q. Wang, Diatom-templated TiO₂ with enhanced photocatalytic activity: biomimetics of photonic crystals, *Applied Physics A*, 113 (2013) 327-332.
- [69] Q.Q. Zhang, R. Chen, L. Li, Synthesis of three-dimensional agaric-like biomorphic TiO₂ by a facile method with *Coscinodiscus* sp frustule, *Journal of Ocean University of China*, 11 (2012) 507-510.
- [70] E. Van Eynde, T. Tytgat, M. Smits, S.W. Verbruggen, B. Hauchecorne, S. Lenaerts, Biotemplated diatom silica-titania materials for air purification, *Photochemical and Photobiological Sciences*, 12 (2013) 690-695.
- [71] Y. Lang, F. del Monte, B.J. Rodriguez, P. Dockery, D.P. Finn, A. Pandit, Integration of TiO₂ into the diatom *Thalassiosira weissflogii* during frustule synthesis, *Scientific Reports*, 3 (2013) 3205.
- [72] E. Van Eynde, Z.Y. Hu, T. Tytgat, S.W. Verbruggen, J. Watte, G. Van Tendeloo, I. Van Driessche, R. Blust, S. Lenaerts, Diatom silica-titania photocatalysts for air purification by bio-accumulation of different titanium sources, *Environmental Science-Nano*, 3 (2016) 1052-1061.
- [73] H. Ma, W.W. Liu, S.W. Zhu, Q. Ma, Y.S. Fan, B.J. Cheng, Biotemplated hierarchical TiO₂-SiO₂ composites derived from *Zea mays* Linn. for efficient dye photodegradation, *Journal of Porous Materials*, 20 (2013) 1205-1215.
- [74] Z.Y. Yan, J. He, L. Guo, Y.T. Li, D.L. Duan, Y.J. Chen, J.J. Li, F.G. Yuan, J.Q. Wang, Biotemplated Mesoporous TiO₂/SiO₂ Composite Derived from Aquatic Plant Leaves for Efficient Dye Degradation, *Catalysts*, 7 (2017) 82.
- [75] F. Adam, L. Muniandy, R. Thankappan, Ceria and titania incorporated silica based catalyst prepared from rice husk: Adsorption and photocatalytic studies of methylene blue, *Journal of Colloid and Interface Science*, 406 (2013) 209-216.
- [76] P. Sujaridworakun, S. Jinawath, W. Panpa, A. Nakajima, M. Yoshimura, Hydrothermal synthesis of TiO₂/SiO₂ hybrid photocatalyst from rice husk ash, *Key Engineering Materials*, 352 (2007) 281-285.

Chapter 6.

Titania-functionalized diatom frustules as photocatalyst for indoor air purification

6.1 Set-up and aim of the research

As described in Chapter 5, TiO₂/SiO₂ hybrid materials are widely studied and diatom frustules represent an interesting silica source for the synthesis of this type of material. In this chapter, the synthesis of titania-functionalized frustules of the diatom species *Thalassiosira Pseudonana* and their application as photocatalysts are described. A graphical summary of the research is shown in Figure 6.1. The work described in this chapter was published with the following reference: J. Ouwehand, E. Van Eynde, E. De Canck, S. Lenaerts, A. Verberckmoes, P. Van Der Voort, Titania-functionalized diatom frustules as photocatalyst for indoor air purification, *Applied Catalysis B: Environmental* **226** (2018) 303.^a

The non-toxic and water soluble titania precursor titanyl sulfate (TiOSO₄) was used in a straightforward impregnation procedure. This makes the synthetic process environmentally friendly, as the alternative titanium alkoxides and titanium chloride salts are much more toxic and often require processing in organic solvents. Additionally, in this procedure, all the titania is deposited onto the frustules, so no titanium-containing waste is produced.

The BET surface area of diatom frustules varies greatly, depending on the diatom species, ranging from below 10 m²/g to above 150 m²/g.¹ In this work, we selected the *Thalassiosira pseudonana* species, because of its high surface area and its straightforward cultivation and

^a Frustule extractions, functionalizations and characterizations were performed by the author, with help from Katrien Hastraete for TEM imaging. Diatom production was performed by TomAlgae. Diatom selection and photocatalytic testing was performed by Erik Van Eynde.

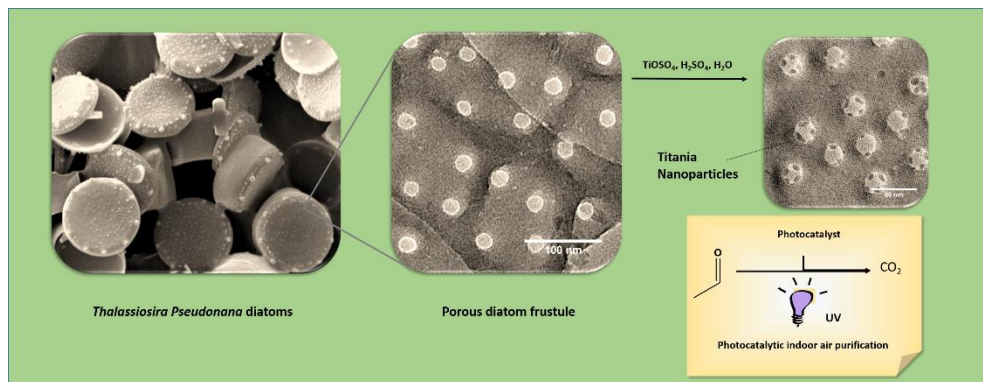


Figure 6.1. A graphical summary of the research presented in this chapter.

fast growth. The synthesis of the photocatalyst was optimized by varying the Ti/Si ratio and the calcination temperature and duration.

The titania-coated frustules were applied in the photocatalytic degradation of gaseous acetaldehyde. This compound was chosen as a benchmark volatile organic compound (VOC), because of its presence in typical polluted indoor air, such as in office buildings.² It has previously been shown that titania photocatalysts can break down mixtures of several carbonyl compounds,³ as well as aromatics and aliphatics.⁴ Therefore, titania-silica photocatalysts have great potential for real applications in indoor air purification systems. In order to further investigate the behavior of our material in more relevant conditions, the photocatalytic behavior was also studied as a function of the relative humidity and for a prolonged period of time.

6.2 Results and discussion

6.2.1 Extraction and characterization of frustules

Diatom frustules were extracted from a sample containing a cultivation of *Thalassiosira pseudonana* in its salt water medium. After an initial washing procedure to remove the majority of the salts, an acid treatment was used to remove any remaining carbonates and to partially digest the organic matter. After washing away the acid, calcination in air at 550°C was used to completely free the frustules of organic components. The purity of the resulting frustules was assessed by a quantitative analysis of any expected trace elements,⁵⁻⁷ using CHN elemental analysis and XRF (X-Ray Fluorescence). Table 6.1 shows the weight percentage of the analyzed elements. The impurities amount to a total of 1.2 wt%, supposing that there are no other significant trace elements. We can therefore conclude that frustules of highly pure silica were obtained.

Table 6.1. Trace elements quantified in the cleaned diatom frustules.

Element ^a	Weight %
P	0.42
Mg	0.38
Fe	0.12
Ca	0.12
C	0.11
Cu	0.011
K	0.0099
Zn	0.0033
S	0.0030
Cl	- ^b
Mn	- ^b
N	- ^b
Total	1.2

^a C and N were determined by CHN elemental analysis, the other elements were determined by XRF.

^b Not detected (below detection limit).

The frustules were visualized by SEM (Scanning Electron Microscopy), as shown in Figure 6.2. It can be observed that the individual frustules are not intact, but instead are broken down to flat or curved plate-like pieces. Although the frustules are not preserved in one piece, the typical rib-like structures and round pore ‘mouths’ (the so-called strutted processes)⁸ can be recognized.

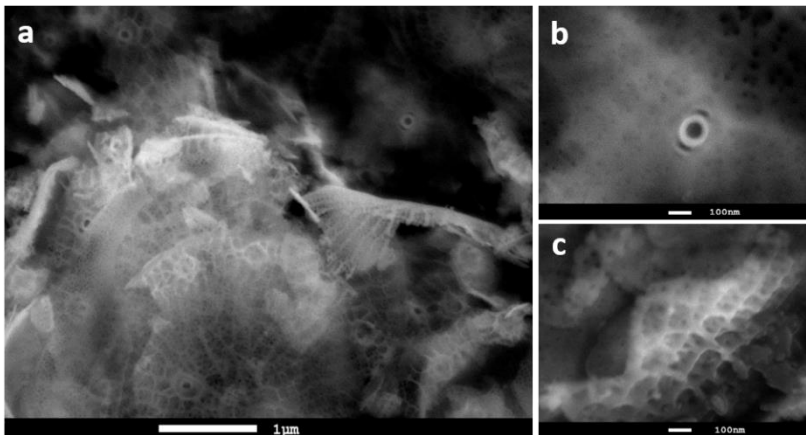


Figure 6.2. SEM images of a) the cleaned frustules, b) the pore mouths and c) the rib-like structures. The scale bar for shows 1 μm for a) and 100 nm for b) and c).

The *Thalassiosira pseudonana* species was chosen for its high surface area, giving it better potential for titania immobilization. Figure 6.3 shows the nitrogen sorption isotherm of the cleaned frustules. The BET surface area of the sample is 115 m²/g, which is relatively high

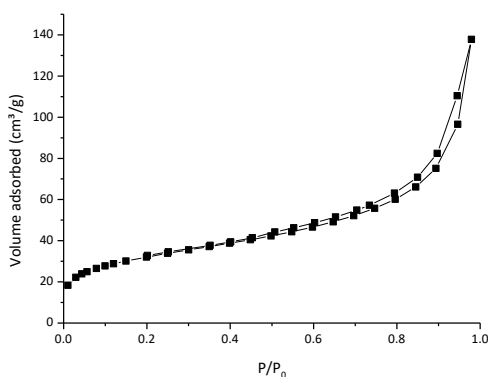


Figure 6.3. Nitrogen sorption isotherm of the cleaned frustules.

compared to other frustules.¹ The type II isotherm is indicative of a plate-like structure, which is also confirmed by TEM (Transmission Electron Microscopy).

Figure 6.4 shows TEM images of the typical pore structure, which consists of near-circular pores. The shape and size of the pores seems to be consistent throughout the sample, as can be seen on TEM images with lower magnification (Figure 6.5). A pore size distribution determined from the left TEM image in Figure 6.4 gives an average pore size of 23.2 nm (see Figure 6.4c).

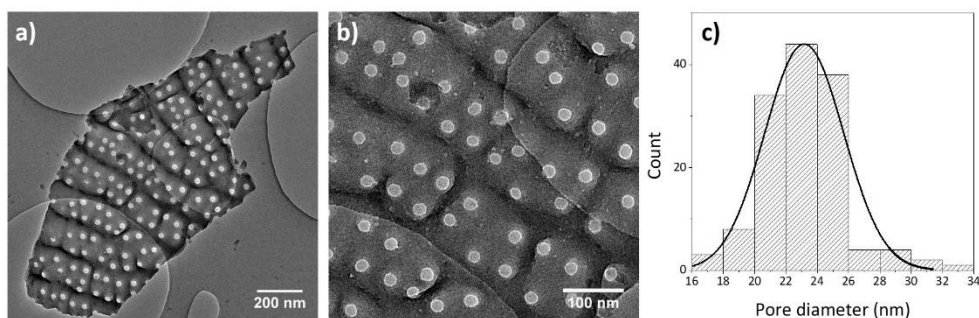


Figure 6.4. TEM images (a and b) of the cleaned frustules, showing the porous structure. c) shows a pore size distribution of the frustules based on image a). The distribution was based on 138 data points. The curve shows the Gaussian fit of the distribution.

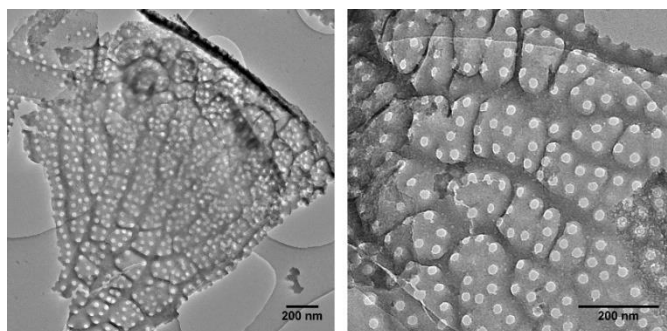


Figure 6.5. Additional TEM images of the frustules at lower magnification showing the homogeneous pore size distribution throughout the sample.

6.2.2 Optimization of calcination temperature and duration

After extraction, the frustules were functionalized with titania by simply adding the silica to a solution of titanyl sulfate in acidified water and subsequently evaporating the liquid. The resulting $\text{SiO}_2/\text{TiO}_2$ composite was then calcined in air at elevated temperature, at which titanyl sulfate decomposes to form crystalline titania.⁹ The conditions were varied by using different calcination temperatures and durations, while the amount of titania precursor used in each synthesis was kept constant (0.8 g titanyl sulfate precursor per gram of silica).

XRD analysis (Figure 6.6) shows that the only crystalline phase present in the calcined samples is anatase. The samples calcined at 550°C and above all show the (101) reflection of the anatase phase at 25.3°. The peaks are broadened due to the small particle size of the anatase (*vide infra*). None of the samples show any reflections corresponding to rutile or brookite phases. While in bulk titania, the phase transformation from amorphous

titania to anatase can already start at 350°C and a phase transition to rutile takes place at 500°C, these transition temperature are often increased for silica-immobilized titania. This is due to the lowered mobility of the titania on the silica surface. The titania nanoparticles aggregate less and remain smaller on the silica surface, compared to pure titania.¹⁰ The transition temperatures of titania depend on the particle size, and can become significantly higher for nanoparticles, compared to bulk titania.¹¹ Therefore, the silica carrier effectively thermally stabilizes the titania, by limiting the nanoparticle growth. This explains that in our samples, anatase is formed at calcination temperatures of 550-650°C and no rutile phase is observed at these temperatures. Table 6.2 gives an overview of some properties of the materials calcined at different conditions. The loading of titania in the materials was determined by XRF and is close to 20 wt% for all samples.

The samples' photocatalytic activity was assessed in the decomposition of gaseous acetaldehyde to carbon dioxide. To correct for the slight differences in titania loading, the activities were expressed per mg of titania and not per mg of composite. It is clear from the data that the calcination temperature of 500°C is not sufficiently high to result in good photocatalytic activity. This is in line with the fact that the XRD intensity of the anatase peak is very low for these samples. XRF analysis shows that the samples calcined for 3 and 6 hours

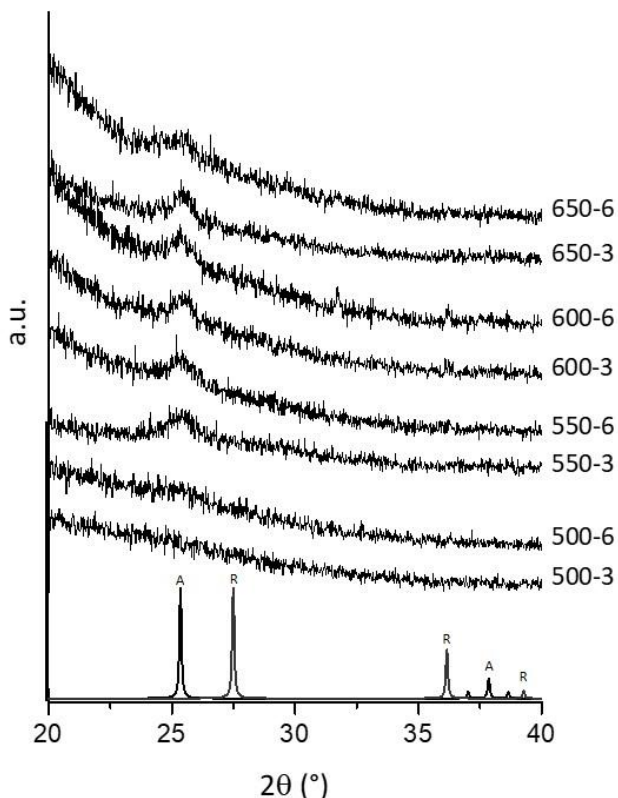


Figure 6.6. X-ray diffractograms of titania-functionalized frustules summarized in Table 2, calcined at different temperatures and durations. The legend indicates the calcination temperature in °C and the duration in h. Reference diffractograms for anatase (A) and rutile (R) are shown below the graphs.

still contain 0.83 and 0.37 mmol of sulfur per gram, respectively. This confirms that the titanyl sulfate precursor was not fully decomposed and converted into titania.

The highest photocatalytic activity is obtained for the sample calcined at 550°C for 3 hours, with a value of 10.4 ppm/min per mg of titania. The samples calcined at higher

temperatures still show high activities (9.5 ppm/min for the samples calcined at 600°C), but the activity clearly decreases with calcination at 650°C. These differences in photocatalytic activity can be explained by two factors, namely the crystallite size and the decrease in BET surface area caused by the calcination treatment.

Table 6.2. Overview of characteristics of the TiO₂/SiO₂ composites calcined at different conditions.

Calcination Temperature	Calcination duration	Loading of TiO ₂ ^a	Average crystallite size ^b	Photocatalytic activity per mg TiO ₂	Decrease in BET surface area after calcination ^c
(°C)	(h)	(wt%)	(nm)	(ppm/min)	(%)
500	3	- ^d	- ^d	0.5	3.5
500	6	- ^d	- ^d	2.6	10
550	3	18.2	12	10.4	11
550	6	21.0	17	9.3	7.8
600	3	21.9	15	9.5	19
600	6	20.8	14	9.5	32
650	3	18.7	19	8.3	22
650	6	21.8	17	6.6	29

^a Determined by XRF.

^b Determined by XRD using the Scherrer equation.

^c Determined by subjecting non-functionalized frustules to the listed calcination conditions.

^d Not determined.

The average crystallite sizes were determined using the Scherrer equation. As will be shown in section 6.2.4, the titania nanoparticles on these materials are inconsistent in shape, whereas the Scherrer equation assumes spherical particles. Therefore, the average crystallite sizes obtained here should not be taken as absolute values, but are rather used to observe a trend in crystallite size. We can see that the crystallite size significantly increases at 650°C. This is in line with expectations based on existing literature. It has been established that increased calcination temperatures cause an increase in anatase crystallite size, which can lead to a decrease in photocatalytic activity.^{12, 13} As for the calcination time, we only see a significant difference in crystallite size for the samples calcined at 550°C. For the samples at 600°C and 650°C, the increase in temperature seems to have a more important effect than the increase of calcination duration.

Another factor which should be taken into account is the thermal stability of the frustules. It has previously been shown that calcination conditions above 550°C damage some frustules' pore structure and the BET surface area decreases due to a partial collapse of the silica structure.⁵ In order to assess this effect for the *Thalassiosira pseudonana* frustules,

the calcination conditions were repeated on non-functionalized frustules, and the BET surface areas before and after calcination were compared (Table 6.2). It is clear from the data that calcination at 500°C and 550°C has little effect on the BET surface area (max. 11% decrease). However, the calcination conditions at 600°C and 650°C do significantly decrease the BET surface area, up to 32%. This collapse of the structure, combined with an increased crystallite size could account for the decreased photocatalytic activity at calcination temperatures of 600 and 650°C.

6.2.3 Optimization of titania loading

From the results in section 6.2.2, we found that calcination at 550°C during 3 hours gives the highest photocatalytic activity. We then investigated how the titania loading affected the activity. To achieve this, the amount of titanyl sulfate precursor used during the impregnation procedure was varied. Figure 6.7 shows the XRD patterns of the obtained

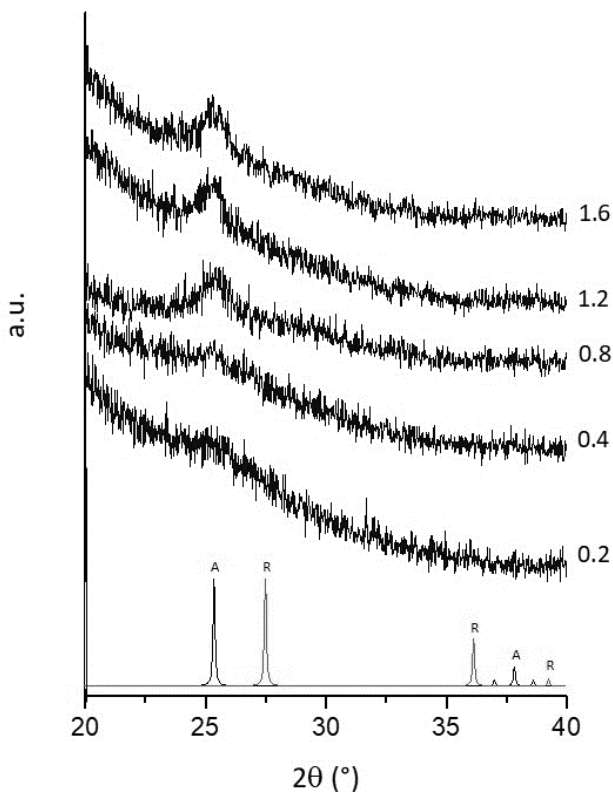


Figure 6.7. X-ray diffractograms of frustules functionalized with different titania loadings, summarized in Table 6.3. The legend indicates the Ti precursor to frustules ratio. Reference diffractograms for anatase (A) and rutile (R) are shown below the graphs.

materials. We can clearly see that the intensity of the (101) anatase reflection increases with increasing loading, suggesting that more anatase is formed at higher loadings.

Table 6.3 lists the synthesis conditions, titania loading, average crystallite size and photocatalytic activity of the samples synthesized with different precursor ratios. Despite the higher amount of anatase formed at higher titania loadings (based on the XRD patterns in Figure 6.7), the photocatalytic activity decreases with loadings of 25 and 29 wt%. It seems that the increase in crystal phase is compensated by an increase in crystallite size, which causes a decrease in activity. At titania loadings of 10.5 and 7 wt%, the average crystallite size could not be determined, due to the low intensity of the XRD signals. We can thus assume from the observed trend that the crystallite sizes are around 10 nm or below. However, the photocatalytic activity at these low loadings is less than that of the sample with a loading of 18.2 wt%, presumably due to a lower crystallization grade. From these data we can conclude that at a loading close to 20 wt%, the interplay between crystallization grade and crystallite size is optimal.

Table 6.3. Overview of characteristics of the TiO₂/SiO₂ composites with different titania loadings.

Amount of Ti precursor used per gram of silica (g)	Loading of TiO ₂ ^a (wt%)	Average crystallite size ^b (nm)	Photocatalytic activity per mg TiO ₂ (ppm/min)
0.2	6.99	- ^c	4.8
0.4	10.5	- ^c	5.1
0.8	18.2	12	10.4
1.2	25.0	15	7.5
1.6	28.9	27	6.3

^a Determined by XRF.

^b Determined by XRD using the Scherrer equation.

^c Not determined.

6.2.4 Further characterization of the optimized photocatalyst

From the previous results, we found that the sample calcined at 550°C during 3 hours, with a titania loading of 18.2 wt% was the optimal photocatalyst. This sample was further investigated with TEM and STEM-EDX^b. The first thing that is apparent from TEM imaging,

^b Scanning Transmission Electron Microscopy - Energy-dispersive X-Ray Spectroscopy

shown in Figure 6.8, is that next to no titania particles are found outside of the frustules, so virtually all the titania was successfully grafted to the silica.

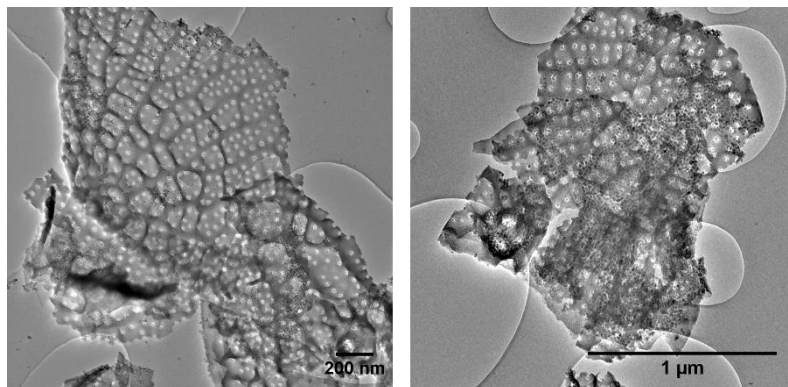


Figure 6.8. TEM images of the titania-functionalized frustules at low magnification showing that very few titania particles (dark spots) are present outside of the silica frustules.

Figure 6.9 shows the TEM images of the optimized catalyst. Image a gives an overview of the functionalized material. Two types of nanoparticles seem to be present on the sample, namely the ones contained inside the pores (detailed in image b) and the ones on the silica surface outside of the pores (detailed in image c). Figure 6.10 shows a STEM-EDX mapping of Si and Ti of the sample, confirming that the dark particles shown on the TEM images are indeed titania nanoparticles. The size of both types of nanoparticles was measured and both average to a size of 8 nm (longest axis of each particle, based on the TEM images). This indicates that both the pores and the silica platelets are effective at grafting the titania nanoparticles and limiting their growth and aggregation. This value is also of the same order of magnitude as the one obtained via the XRD patterns and the Scherrer equation (12 nm).

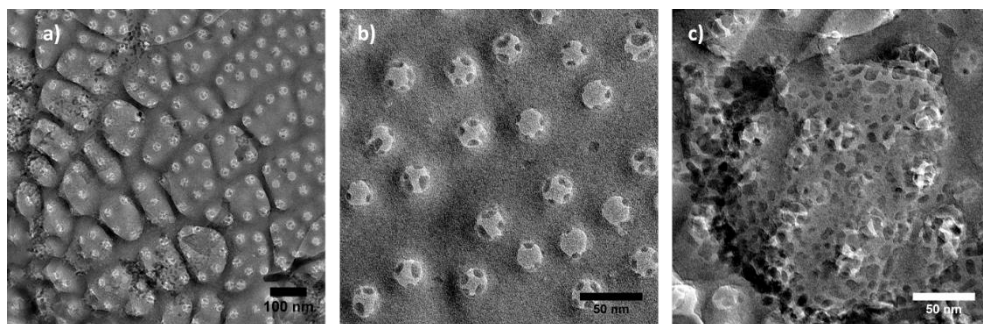


Figure 6.9. TEM images of the optimized titania functionalized frustules.

We compared the optimized photocatalyst to P25, which is a commercial crystalline titania powder and is widely considered as a benchmark material for photocatalysis. In the

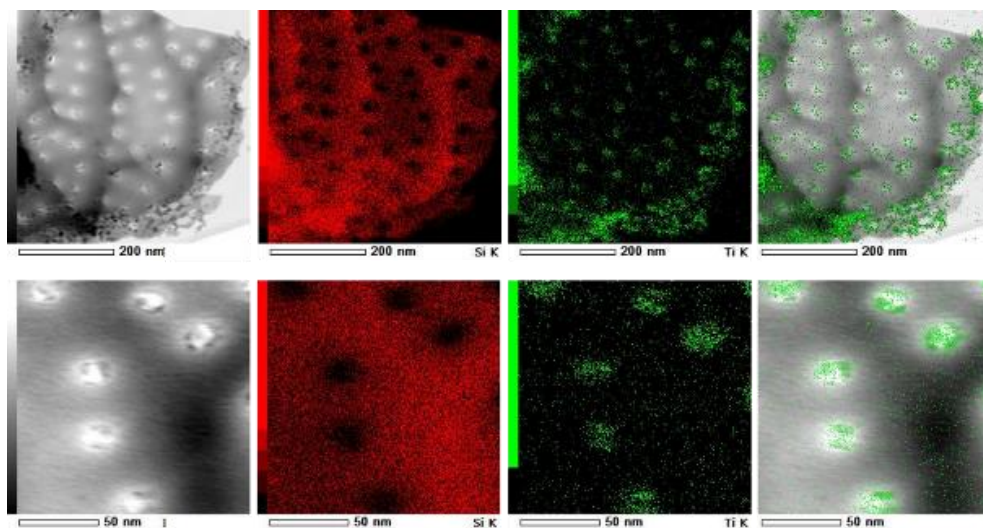


Figure 6.10. STEM-EDX mapping of the optimized titania functionalized frustules. Si mapping is shown in red, Ti mapping in green.

photocatalytic degradation of acetaldehyde, P25 showed an activity of 4.3 ppm/min per mg. With an activity of 10.4 ppm/min per mg, the titania grafted on the frustules is almost 2.5 times more active, which can be related to the average anatase particle size of 12 nm, compared to 29 nm for P25 (according to the Scherrer equation). This decrease in particle size increases the available surface area of the active titania phase, thus increasing the photocatalytic activity. Smaller nanoparticles are also more active because a larger fraction of the charge carriers can reach the titania surface.¹⁴ Additionally, as can be seen on the TEM images in Figure 6.9, the silica surface is not fully covered with titania, and a significant amount of silica surface is available for the adsorption of acetaldehyde. It has been established in the literature that in this case, a so-called ‘adsorb and shuttle’ mechanism can take place (see also Chapter 5).¹⁵ This means that the targeted pollutant can be adsorbed on a silica site close to a titania particle and then migrate on to the active titania site via diffusion. According to this mechanism, the silica is not merely an inert carrier material, but actively participates in an increase in photocatalytic activity. This effect has been observed in several studies, using different types of carriers such as activated carbon, silicates and zeolites.¹⁶⁻²⁰

6.2.5 Influence of humidity on the photocatalytic activity

After the optimization of the photocatalyst, the influence of the relative humidity (RH) on the photocatalytic activity was investigated. In fact, all previously mentioned photocatalytic tests were performed in dry conditions. In the literature, generally a negative effect of

humidity on the photocatalytic abatement of VOCs in the gas phase is reported.^{3, 21, 22} Figure 6.11 shows the activity of the optimized photocatalyst, as well as the P25 benchmark, as a function of the relative humidity. The activity of P25 gradually decreases to 42% of the initial activity at 75% RH. The titania functionalized frustules show a different behavior with a maximum at 12.5% RH followed by a decrease to 53% of the initial activity at 75% RH.

Water has a dual function in the photocatalytic abatement of VOCs. On one hand, water can form hydroxyl radicals, which are one of the active species in the oxidation process. At high amounts of adsorbed water, the formation of hydroxyl radicals is also possible through the dissociation of hydrogen peroxide. On the other hand, if too much water is present, it

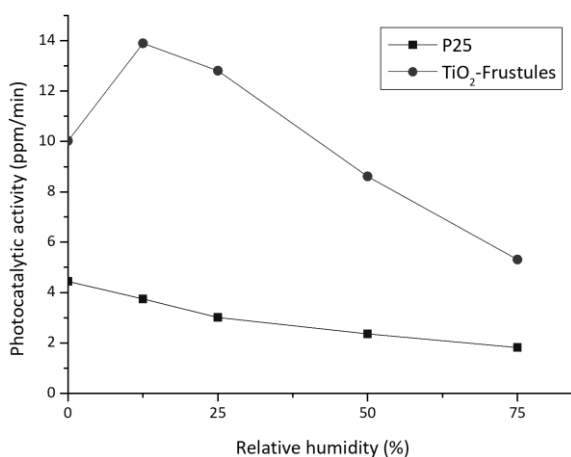


Figure 6.11. Photocatalytic activity of the optimized photocatalyst (●) and P25 (■) as a function of the relative humidity.

can form a multilayer on the titania surface, preventing acetaldehyde to access the titania hydroxyl sites (Ti-OH), thus inhibiting the decomposition reaction.¹⁰

Before the start of the photocatalytic experiment, the materials were UV-illuminated for 30 min. Silica is UV-transparent and the surface composition is unaltered. Titania on the other hand undergoes a surface transformation by the formation of hydrophilic Ti-OH sites.²³ From the TEM images of the composite material (Figure 6.9), it is clear that the silica surface is not fully covered by titania, so that a significant amount of silanol groups (Si-OH) is available to adsorb water. Hence, on the composite material, both Ti-OH and Si-OH sites are present. Additionally, the specific surface area of P25 is 45 m²/g, compared to 85 m²/g for the composite. Therefore, supposing that the water in the air is attracted to both the Ti-OH and Si-OH surface groups, the effective water concentration at the Ti-OH sites should be lower for the composite than for pure titania, at least at low RH values. At higher RH values,

even the Ti-OH groups on the composite could become saturated with water and the activity could decrease. This hypothesis could explain the maximum in photocatalytic activity at 12.5% RH for the functionalized frustules.

The relative humidity of indoor air is typically around 50%. It is obvious from Figure 6.11 that the activity of the functionalized frustules is not optimal at these conditions. Still, at 50% RH, the activity only decreased by 14% compared to dry air, as opposed to a decrease of 45% for P25. This proves the positive effect of the frustules for applications in indoor air purification.

6.2.6 Extended activity study

For application in indoor air purification, the lifetime of the catalyst is an important factor. Therefore, we studied the deactivation over time of the photocatalyst by performing a longer measurement at 50% RH, represented in Figure 6.12. All measurements in this work were performed by three cycles of UV-illumination during 20 minutes, where the activity stabilizes in the second and third cycles (see description of the experimental details, section 6.4). Here, we prolonged the third UV-cycle to 47.3 hours.

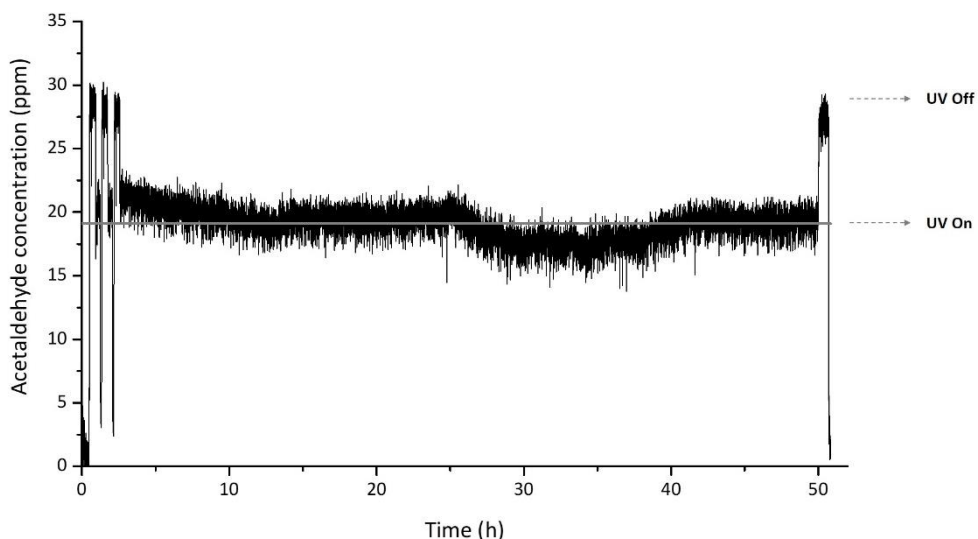


Figure 6.12. The concentration of acetaldehyde recorded during the photocatalytic reaction with the functionalized frustules, at 50% relative humidity. The gray line shows the average acetaldehyde concentration during the abatement phases.

After 48 hours of total reaction time, the activity stays relatively stable. Some fluctuations occur in the measurement, which might be due to fluctuations of the UV-lamp intensity. The average of the acetaldehyde concentration during the abatement phases (UV light on) is shown by the gray horizontal line in Figure 6.12. This average value comes to 8.0

ppm/min, per mg of titania, which is only slightly lower than the 8.6 ppm/min recorded in the short measurement (Figure 6.11, 50% RH), which consisted of a total reaction time of one hour. We can therefore state that although the activity of the functionalized frustules is not constant over a long period of time, there is only a slight decrease in the average activity. In conclusion, the functionalized frustules are a promising photocatalyst in the purification of indoor air, according to our test reactions at 50% RH over an extended period of time.

6.3 Conclusions

In conclusion, a straightforward method for the synthesis of titania functionalized diatom frustules was presented. Frustules were extracted from the diatom species *Thalassiosira Pseudonana* with a high purity and high surface area. The grafting of titania was optimized and the resulting composites were tested in the decomposition of gaseous acetaldehyde. We found the highest activity for the sample with 18.2 wt% titania loading, calcined at 550°C during three hours. The titania immobilized under these conditions is 2.5 times more active than the benchmark photocatalyst P25, which can be related to a smaller particle size of the active anatase phase. This is due to a stabilization of the titania particles on the silica surface of the frustules. When tested in realistic conditions for the purification of indoor air, namely at elevated relative humidity and extended reaction time, the photocatalyst shows promising results. This type of photocatalyst would be suitable for indoor air purification systems consisting of an air circulation device and an interior surface coated with photocatalyst and irradiated with UV light. Thus, we believe that in light of a probable increase in diatom cultivation for biofuel production, the silica frustules should not be discarded as a side product, but can be valorized in technological applications such as the one investigated in this work.

6.4 Experimental details

Procedure for frustule extraction. *Thalassiosira pseudonana* was isolated from the North Sea at Oostende (Belgium) and cultivated on large scale in 10 m³ raceway ponds at the facilities of TomAlgae (Nevele, Belgium). At the end of the cultivation the algae were harvested and upconcentration of the biomass into an algae paste was performed using the Evodos T25 spiral plate separator equipment. The obtained diatom paste has a dry weight of approximately 5wt% and was stored in a freezer at -20°C up to use. The extraction of the frustules from the biomass started with 500 ml of the frozen diatom paste, which was allowed to thaw at room temperature during 6 hours. The resulting liquid was divided over several centrifuge tubes and washed by adding distilled water, followed by centrifugation at 2000 rpm during 10 minutes. The decanted washing water was tested for the presence of chlorides by adding a few drops of a 0.1M solution of AgNO₃ (Sigma Aldrich, <99%). The

washing cycle was repeated until no white AgCl precipitation was formed. The washed algae were collected, diluted to a total volume of 1L with distilled water, and then 350 ml HCl (37%, Carl Roth) was added. This mixture was stirred overnight and then repeatedly washed by adding distilled water, followed by centrifugation and decantation. The washing cycles were repeated until the washing water was at pH 5-6. The resulting green paste was dried at 60°C for 3 hours, followed by calcination in air at 550°C (heating rate 60°C/h) during 6 hours. The resulting white silica material was crushed with a pestle and mortar to form a fine powder. This procedure yielded up to 7 g of silica.

Titania functionalization procedure. 0.32 g of Titanium(IV) oxysulfate - sulfuric acid hydrate (Sigma Aldrich, also referred to as titanyl sulfate in this work) was added to 4 ml of distilled water and heated at 65°C until the product fully dissolved. After cooling down to room temperature, 0.4 g of frustules were added and the mixture was stirred at 500 rpm during 2 hours. The mixture was then heated to 55°C and stirred at 150 rpm until all the liquid was evaporated. The resulting solid was calcined in air at 550°C (heating rate 60°C/h) during 3 hours. This procedure yields approximately 20 m% titania on the silica support. The same method was performed using different calcination temperatures and durations (see Table 6.2) and with different precursor ratios (see Table 6.3).

Photocatalytic abatement of acetaldehyde. The photocatalytic performance of the prepared diatom-TiO₂ samples towards the degradation of gas phase acetaldehyde is tested using the photocatalytic test setup described in detail by Tytgat et al.²⁴ All samples were first suspended in water (20 mg powder + 2 mL water) and stirred ultrasonically for 30 min. On two silicon wafers (2.5 x 1.5 cm²), 500 µL of the suspension was drop casted. The slides were left to dry in an oven at 70°C for 2h. As a reference, the photocatalytic activity of Aeroxide P25 titania nanoparticles (Evonik) is also determined. The P25 sample is pretreated in the same manner. The photodegradation experiments are conducted in a flat plate photoreactor equipped with a 25W UV-TL-lamp (3.2 mW/cm²) with a maximum wavelength of 354 nm and is operated in continuous flow mode. The photoreactor consists of a slit shaped reactor volume with dimensions 80 x 15 x 2 mm³. The schematic design is shown in Figure 6.13. In the reactor slit a silicon wafer loaded with 5 mg of sample is placed. The reactor is sealed by a quartz plate and is made air tight with a tension ring. Acetaldehyde (C₂H₄O) is selected as test pollutant. A synthetic gas mixture of dry air (Air Liquide) and acetaldehyde (Air Liquide, 1% in N₂) was mixed by mass flow controllers resulting in an acetaldehyde gas concentration of 40 ppmv and a total flow of 400 cm³ min⁻¹. For the measurements at different humidity, part of the gas flow was sent through a wash bottle. Humidity levels between 0 and 75 % are tested.

Each photodegradation experiment consisted of 4 subsequent phases: (1) 10 min gas flow (400 cm³ min⁻¹) in bypass, (2) 15 min gas flow through the dark reactor in order to achieve

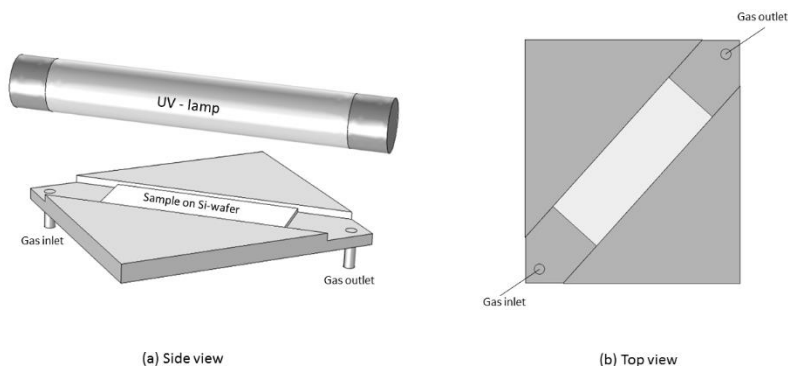


Figure 6.13. Schematic representations of the used photocatalytic reactor

adsorption/desorption equilibrium, (3) 20 min gas flow through the reactor under UV-illumination and (4) 5 min air flow (flush phase) through the dark reactor. Before the experiment starts the samples are pretreated with UV for 30 minutes. For the extended activity measurement, phase (3) is extended to 47.3 hours. During these different phases detection of acetaldehyde and carbon dioxide in the gas effluent was carried out using a Nicolet™ 380 FTIR spectrometer (Thermo Fisher Scientific) with ZnSe windows and a 2 m heated gas cell. Spectra were recorded in a range of $4000 - 400 \text{ cm}^{-1}$. The used $\nu_{\text{C}_2\text{H}_4\text{O}}$ and ν_{CO_2} stretch band positions of acetaldehyde and CO_2 are located at 2728 and 2360 cm^{-1} respectively. The peak heights at these wavenumbers are correlated with concentrations using a calibration curve.

Characterization methods. XRF measurements were performed on a NEX CG from Rigaku. CoO and TiO_2 were measured at different ratios to obtain a linear calibration curve. Photocatalyst samples were weighed and mixed with a known amount of CoO to determine the loading of TiO_2 . For trace element analysis, the quantification was directly performed by the apparatus.

XRD was performed with an ARL X'TRA apparatus (Thermo Scientific). Average crystallite sizes were determined using the Scherrer equation on the (101) reflection of the anatase phase by using: $d = \frac{0.9\lambda}{(\beta - b)\cos\theta}$, where d is the crystallite size, λ is the X-ray wavelength, β is the peak width (FWHM), b is the instrumental peak width (determined by measuring LaB6 crystals) and θ is the diffraction angle.

Elemental analysis was performed with a Thermo Flash 2000 Thermal Analyzer (Thermo Scientific). Nitrogen-sorption measurements were performed with a TriStar 3000 analyzer (Micromeritics). TEM and STEM-EDX measurements were performed on a JEOL JEM 2200-FS. SEM measurements were performed on a JEOL JSM 7600F FEG.

All measurements were performed after drying of the sample under vacuum at 120°C.

6.5 References

- [1] A. Gelabert, O.S. Pokrovsky, J. Schott, A. Boudou, A. Feurtet-Mazel, J. Mielczarski, E. Mielczarski, N. Mesmer-Dudons, O. Spalla, Study of diatoms/aqueous solution interface. I. Acid-base equilibria and spectroscopic observation of freshwater and marine species, *Geochimica et Cosmochimica Acta*, 68 (2004) 4039-4058.
- [2] S.O. Hay, T. Obee, Z. Luo, T. Jiang, Y.T. Meng, J.K. He, S.C. Murphy, S. Suib, The Viability of Photocatalysis for Air Purification, *Molecules*, 20 (2015) 1319-1356.
- [3] M.L. Zhang, T.C. An, J.M. Fu, G.Y. Sheng, X.M. Wang, X.H. Hu, X.J. Ding, Photocatalytic degradation of mixed gaseous carbonyl compounds at low level on adsorptive TiO₂/SiO₂ photocatalyst using a fluidized bed reactor, *Chemosphere*, 64 (2006) 423-431.
- [4] N. Abbas, M. Hussain, N. Russo, G. Saracco, Studies on the activity and deactivation of novel optimized TiO₂ nanoparticles for the abatement of VOCs, *Chemical Engineering Journal*, 175 (2011) 330-340.
- [5] E. Van Eynde, B. Lenaerts, T. Tytgat, S.W. Verbruggen, B. Hauchecorne, R. Blust, S. Lenaerts, Effect of pretreatment and temperature on the properties of Pinnularia biosilica frustules, *Rsc Advances*, 4 (2014) 56200-56206.
- [6] W.K. Jiang, H.Q. Pan, F.X. Wang, M.L. Jiang, X.Y. Deng, J.B. Li, A rapid sample processing method to observe diatoms via scanning electron microscopy, *Journal of Applied Phycology*, 27 (2015) 243-248.
- [7] W.K. Jiang, S.P. Luo, P.W. Liu, X.Y. Deng, Y. Jing, C.Y. Bai, J.B. Li, Purification of biosilica from living diatoms by a two-step acid cleaning and baking method, *Journal of Applied Phycology*, 26 (2014) 1511-1518.
- [8] E.E.S. Grethe R. Hasle, Karen A. Steidinger, Karl Tangen, Carmelo R. Tomas, Identifying Marine Diatoms and Dinoflagellates, *Academic Press*, 1996.
- [9] Y.Y. Huang, B.Y. Zhao, Y.C. Xie, A novel way to prepare silica supported sulfated titania, *Applied Catalysis A*, 171 (1998) 65-73.
- [10] Y. Hendrix, A. Lazaro, Q. Yu, J. Brouwers, Titania-Silica Composites: A Review on the Photocatalytic Activity and Synthesis Methods, *World Journal of Nano Science and Engineering*, 5 (2015) 161-177.
- [11] O. Khatim, M. Amamra, K. Chhor, A.M.T. Bell, D. Novikov, D. Vrel, A. Kanaev, Amorphous-anatase phase transition in single immobilized TiO₂ nanoparticles, *Chemical Physics Letters*, 558 (2013) 53-56.

- [12] P. Cheng, M.P. Zheng, Q. Huang, Y.P. Jin, M.Y. Gu, Enhanced photoactivity of silica-titania binary oxides prepared by sol-gel method, *Journal of Materials Science Letters*, 22 (2003) 1165-1168.
- [13] D.R. Sahu, L.Y. Hong, S.C. Wang, J.L. Huang, Synthesis, analysis and characterization of ordered mesoporous TiO₂/SBA-15 matrix: Effect of calcination temperature, *Microporous and Mesoporous Materials*, 117 (2009) 640-649.
- [14] T. Luttrell, S. Halpegamage, J.G. Tao, A. Kramer, E. Sutter, M. Batzill, Why is anatase a better photocatalyst than rutile? - Model studies on epitaxial TiO₂ films, *Scientific Reports*, 4 (2014) 4043.
- [15] Y. Paz, Composite Titanium Dioxide Photocatalysts and the "Adsorb & Shuttle" Approach: A Review, *Solid State Phenomena*, 162 (2010) 135-162.
- [16] T. Torimoto, S. Ito, S. Kuwabata, H. Yoneyama, Effects of adsorbents used as supports for titanium dioxide loading on photocatalytic degradation of propylamide, *Environmental Science & Technology*, 30 (1996) 1275-1281.
- [17] N. Takeda, M. Ohtani, T. Torimoto, S. Kuwabata, H. Yoneyama, Evaluation of diffusibility of adsorbed propionaldehyde on titanium dioxide-loaded adsorbent photocatalyst films from its photodecomposition rate, *Journal of Physical Chemistry B*, 101 (1997) 2644-2649.
- [18] C.H. Ao, S.C. Lee, Combination effect of activated carbon with TiO₂ for the photodegradation of binary pollutants at typical indoor air level, *Journal of Photochemistry and Photobiology A: Chemistry*, 161 (2004) 131-140.
- [19] I.S. Park, S.Y. Choi, J.S. Ha, High-performance titanium dioxide photocatalyst on ordered mesoporous carbon support, *Chemical Physics Letters*, 456 (2008) 198-201.
- [20] R. Portela, I. Jansson, S. Suarez, M. Villarroel, B. Sanchez, P. Avila, Natural silicate-TiO₂ hybrids for photocatalytic oxidation of formaldehyde in gas phase, *Chemical Engineering Journal*, 310 (2017) 560-570.
- [21] A.K. Boulamanti, C.J. Philippopoulos, Photocatalytic degradation of C-5-C-7 alkanes in the gas-phase, *Atmospheric Environment*, 43 (2009) 3168-3174.
- [22] W.K. Jo, J.T. Kim, Application of visible-light photocatalysis with nitrogen-doped or unmodified titanium dioxide for control of indoor-level volatile organic compounds, *Journal of Hazardous materials*, 164 (2009) 360-366.
- [23] R. Wang, N. Sakai, A. Fujishima, T. Watanabe, K. Hashimoto, Studies of surface wettability conversion on TiO₂ single-crystal surfaces, *Journal of Physical Chemistry B*, 103 (1999) 2188-2194.

[24] T. Tytgat, B. Hauchecorne, M. Smits, S.W. Verbruggen, S. Lenaerts, Concept and Validation of a Fully Automated Photocatalytic Test Setup, *Journal of Laboratory Automation*, 17 (2012) 134-143.

Outlook and Perspectives

This dissertation tackles two subjects that contain many similarities despite appearing to be very different. Both projects make use of porous materials and take advantage of their increased surface area. This surface area enlargement is directly inspired by nature, as many biological systems such as our lungs and intestines make use of the same principle to ensure an optimal interaction of the surface with its target molecules. Both research projects were also inspired by nature in other ways. In the photocatalysis part, the porous silica material, namely the diatom frustules, were literally taken from nature. The hierarchical silica structures, containing countless symmetry elements and fractal patterns, synthesized biogenically by the diatoms truly humble us as material chemists with our limited scope of synthetic procedures. In the PMO research, the endeavor to design solid enamine catalysts is often compared in the literature to enzyme catalysts. In fact, enzymes such as aldolases are highly selective enamine catalysts, but they are limited to physiological reaction conditions. In a way, the attempt to make solid enamine catalysts that are more stable in different conditions (increased temperatures and different solvents) is a way to mimic the activity of these enzymes outside of their natural environments. The fact that we can do so by immobilizing amino acids, which are the building blocks of these enzymes, makes this circle complete.

Another parallel between both projects is the functionalization of the porous starting material, using methods that are as straightforward and benign as possible. The TiOSO_4 precursor was specifically chosen for the functionalization of the diatom frustules because of the possibility to process it in water. For the PMO functionalization, the UV-mediated click reaction was also performed in water, which is rarely explored outside of the field of polymer synthesis.

The main difference between the two projects is probably their application possibilities. Titania is known as a very cheap photocatalyst, which can easily be produced on a large scale. The diatom frustules are envisaged as a cheap side product of the large-scale diatom

production which could take off in the near future for the production of biofuel. Therefore, the titania-functionalized frustules were developed with a large-scale production in mind and the procedures were already upscaled from milligram scale to gram scale. On the other hand, PMO materials are more expensive to produce. Therefore, PMO-based catalysts are usually developed with the small-scale production of fine chemicals in mind. In fact, the aldol reaction is a very useful catalytic reaction in that field. For the reason of cost, it is also important to consider the reasoning behind the use of PMOs in a specific application, compared to mesoporous silicas, which are cheaper to produce. The main advantage of PMO materials is their hydrolytic stability. This is also why we focused on the modification of PMOs directly on the PMO backbone, instead of using silanes to modify PMOs. This is in my view the only way to fully take advantage of the beneficial properties of PMOs compared to silicas. However, the main downside of PMOs is perhaps the fact that their behavior is not always predictable. In Chapter 3, it was shown that the modification of the ePMO with cysteine and cysteamine could not successfully be translated to the mAR-PMO, which was by no means obvious or predictable beforehand. Also, Chapter 4 showed that a synthetic strategy which was reported on silica materials could not be directly transferred to the thiol PMO without difficulties. Therefore it seems that when developing PMO-based catalytic systems, there is no universal strategy that applies to all PMO systems, and each PMO material will have to be investigated separately.

As for the research presented in this dissertation, some suggestions can be made for further work on these topics. For the cysteamine/cysteine PMO systems, one of the factors that could be further investigated is the reusability of these materials. A study of the deactivation of this type of material in function of time, using flow chemistry is currently under way in the group of Prof. Thybaut. For the proline PMO, obviously a lot of work is left to do in order to obtain sufficient conversion rates and enantioselectivities. Here, several factors could be investigated, for instance a variety of different linkers could be tested for the thiol-ene click functionalization of PMO materials. Possibly, computational studies could give some insight into the desired linker properties as well as the influence that the capping of the silanol groups has on the catalysis. Alternatively, different grafting strategies could be applied, possibly starting from a different PMO material. For the titania-functionalized frustules, an obvious addition to the current work would be doping of the titania phase. This could expand the possible applications of the material beyond air purification, which requires UV activation. It would also be interesting to do a systematic study of frustules taken from several diatom species, to see if any of the morphological features of different diatoms have specific advantages in the immobilization of titania nanoparticles.

